

RICE UNIVERSITY

**Ordering and motion of anisotropic nanomaterials**

by

**Saumyakanti Khatua**

A THESIS SUBMITTED  
IN PARTIAL FULFILMENT OF THE  
REQUIREMENTS FOR THE DEGREE

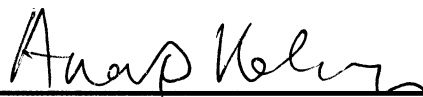
**Doctor of Philosophy**

APPROVED, THESIS COMMITTEE:



---

Stephan Link,  
Assistant Professor of Chemistry and  
Electrical and Computer Engineering



---

Anatoly B. Kolomeisky,  
Professor of Chemistry



---

Naomi J. Halas,  
Professor of Electrical and Computer  
Engineering, Bioengineering, Physics and  
Astronomy, and Chemistry

HOUSTON, TEXAS

October 2011

## ABSTRACT

Ordering and motion of anisotropic nanomaterials

by

Saumyakanti Khatua

Multi-scale ordering of the components is of utmost importance for the preparation of any functional system. This is particularly interesting for the assembly of plasmonic nanoparticles which show drastic differences in their optical properties compared to the individual counterparts, giving rise to the unique opportunity to perform enhanced spectroscopies, sensing, and transporting optical information below the diffraction limitation of light. The control over ordering of nanoscale materials is therefore of paramount importance. Template based bottom up approaches such as using nematic liquid crystals promise a long range, reversible ordering of nanomaterials. It also promises active control over plasmonic properties of metal nanoparticles due to the electric field induced reorientation of liquid crystals, resulting in a change of the local refractive index. This thesis discusses the possibility of ordering anisotropic metal nanoparticles and performing active modulation of the plasmonics response using a nematic liquid crystals. While long polymer chains can be solvated and aligned in liquid crystal solvents, anisotropic metal nanoparticles could not be dissolved in the nematic liquid crystal phase because of their poor solubility. Here, I show that appropriate surface functionalization can increase the otherwise low solubility of plasmonic nanoparticles in a nematic liquid crystal matrix. I also show that it is possible to reversibly modulate the polarized scattering of individual gold nanorods through an electric field induced phase

transition of the liquid crystal. In this thesis, I also studied the motion of a molecular machine, commonly known as nanocars, over different solid surface. I show that individual nanocars, which consist of four carborane wheels attached to an aromatic backbone chassis, can move up to several micrometers over a glass surface at ambient temperature. Their movement is consistent with the rolling of the carborane wheels and can be controlled by tuning the interaction between the surface and the wheels.

## ACKNOWLEDGEMENTS

I thank my advisor, Professor Stephan Link, for his guidance and support throughout my Ph.D. His guidance and leadership have been the corner stone for my professional development.

I thank Professor Christy Landes for all her support, guidance, and encouragement throughout the course of my Ph.D.

I am privileged to have studied at Rice University and I would like to extend my gratitude to the school and the members of the staff who provide the backbone that keeps Rice standing and running and who always lent a hand in the times of need. Particularly, I would like to thank Rose Gray-Dye, Dr. Linda Hamaker of the Chemistry Department and Susan Cudnik of the Chemistry Stockroom.

I take this opportunity to thank all the former and current group members and collaborators for making all these projects possible. Particularly, I thank Dr. Alexei Tcherniak who introduced me to the world of Matlab programming, Mrs. Jazmin Godoy, Mr. Pattanawit Sanglap, Mrs. Jana Olson, and Dr. Wei-Shun Chang for their great help throughout all these projects. I also thank Professor Naomi Halas, Professor Anatoly Kolomeisky, and Professor James Tour for many fruitful discussions and suggestions. .

Most importantly, I am very thankful to my family and friends whose continuous support gave me strength and encouragement:

## TABLE OF CONTENTS

<b>ABSTRACT</b> .....	<b>ii</b>
<b>ACKNOWLEDGEMENTS</b> .....	<b>iv</b>
<b>TABLE OF CONTENTS</b> .....	<b>v</b>
<b>LIST OF FIGURES</b> .....	<b>ix</b>
<b>CHAPTER 1: INTRODUCTION</b> .....	<b>1</b>
1.1 Motivation and background .....	1
1.2 Specific aims .....	7
1.3 Overview .....	7
<b>CHAPTER 2: PLASMONIC NANOPARTICLES-LIQUID CRYSTAL COMPOSITES</b> .....	<b>10</b>
2.1 Abstract .....	10
2.2 Introduction .....	11
2.3 Materials and methods .....	13
2.3.1 General .....	13
2.3.2 Synthesis of 1-decanethiol-capped gold nanoparticles .....	14
2.3.3 Synthesis of monodisperse 6 nm gold nanoparticles .....	14
2.3.4 Ligand exchange of 6 nm gold nanoparticles .....	14
2.3.5 Covalent attachment of 4'- <i>n</i> -octyloxybiphenyl-4-carboxylic acid to mercaptophenol-functionalized 6 nm gold nanoparticles .....	15

2.3.6 Synthesis of 4-sulfanylphenyl-4-[4-(octyloxy)phenyl]benzoate (SOPB) thiol.....	15
2.3.7 Preparation of gold nanoparticle-liquid crystal composites .....	16
2.3.8 Optical absorption measurements .....	17
2.4 Results and discussion .....	18
2.5 Conclusions .....	28
2.5 Acknowledgements .....	29
<b>CHAPTER 3: ACTIVE MODULATION OF NANOROD PLASMON .....</b>	<b>30</b>
3.1 Abstract .....	30
3.2 Introduction .....	31
3.3 Materials and methods .....	33
3.3.1 Materials .....	33
3.3.2 Fabrication of interdigitated electrode arrays .....	33
3.3.3 Characterization of single gold nanorods .....	34
3.3.4 Liquid crystal cell assembly .....	36
3.3.5 Liquid crystal cell thickness measurement .....	38
3.3.6 Analytical solution for the polarization change of light passing through homogeneous and twisted nematic liquid crystal phases .....	40
3.4 Results and discussion .....	44
3.5 Conclusions.....	61
3.6 Acknowledgements .....	61

## **CHAPTER 4: MICROMETER-SCALE TRANSLATION AND MONITORING OF**

<b>INDIVIDUAL NANOCARS ON GLASS .....</b>	<b>62</b>
4.1 Abstract .....	62
4.2 Introduction .....	63
4.3 Materials and methods .....	64
4.3.1 General synthetic methods .....	64
4.3.2 Sample preparation .....	67
4.3.3 Single molecule imaging .....	67
4.4 Results and discussion .....	69
4.5 Conclusion .....	79
4.6 Acknowledgements .....	80

## **CHAPTER 5: INFLUENCE OF THE SUBSTRATE ON THE MOBILITY OF**

<b>INDIVIDUAL NANOCARS .....</b>	<b>81</b>
5.1 Abstract .....	81
5.2 Introduction .....	82
5.3 Materials and methods .....	82
5.3.1 General synthetic methods .....	82
5.3.2. Synthesis of BODIPY S2 and BODIPY-based trimer S4 .....	83
5.3.3 Surface modification .....	84
5.3.4 AFM imaging on different surfaces .....	85
5.3.5 Sample preparation .....	86
5.3.6 Single molecule spectroscopy .....	86

5.4 Results and discussion .....	87
5.5 Conclusions .....	92
5.5 Acknowledgements .....	93
<b>CHAPTER 6: CONCLUSIONS .....</b>	<b>94</b>
<b>APPENDIX A: MOST COMMONLY USED PROGRAMS THAT WERE WRITTEN AND USED IN THE COURSE OF THIS WORK .....</b>	<b>96</b>
<b>APPENDIX B: CALIBRATION OF BULK FLUORESCENCE SPECTRA ACQUIRED BY A COMMERCIAL FLUOREMETER .....</b>	<b>102</b>
<b>BIBLIOGRAPHY .....</b>	<b>105</b>



## LIST OF FIGURES

- Figure 2.1.** Transmission electron microscopy image of decanethiol-coated gold nanoparticles. The inset shows the nanoparticle size distribution. 18
- Figure 2.2.** Molecular graphics representation of a gold nanoparticle functionalized with SOPB thiols. A 5CB molecule is shown for comparison in the upper left corner. 20
- Figure 2.3.** Experimental (solid lines) and calculated (dashed lines) absorption spectra of SOPB-functionalized gold nanoparticles in methylene chloride (green lines,  $\lambda_{\text{max}} = 531$  nm) and in 5CB (red lines,  $\lambda_{\text{max}} = 539$  nm). The spectra were normalized at the corresponding absorption maxima. The inset compares the absorption spectra of decanethiol- and SOPB-functionalized gold nanoparticles in 5CB (blue and red, respectively). All spectra were taken with the nematic director parallel to the light polarization 21
- Figure 2.4.** Absorption spectra of SOPB-functionalized gold nanoparticles in the nematic (red) and isotropic (blue) phases of 5CB (A). The spectra were taken at temperatures of  $T = 25^{\circ}\text{C}$  and  $T = 35^{\circ}\text{C}$ , respectively. Repeated cycling between these temperatures had no effect on the O.D. as measured at the plasmon resonance (B) confirming the stable solvation of the gold nanoparticles inside the liquid crystal. This is furthermore in agreement with the small, but reproducible shift in the plasmon resonance maximum (C). 23
- Figure 2.5.** Nematic-to-isotropic phase transition of neat 5CB (red) and 5CB doped with SOPB-functionalized gold nanoparticles (green). The temperature dependence of the relative transmittance (data points) was fitted with a sigmoidal function (solid lines). Error bars were calculated from three independent measurements. 26
- Figure 2.6.** Freedericksz transition of nanoparticle-doped (green) and undoped

(red) liquid crystal devices. The lines connect the experimental points and are included as guides for the eyes only. Error bars were calculated from two independent measurements. 27

**Figure 3.1.** Photograph of an interdigitated electrode array with 10  $\mu\text{m}$  gaps between electrodes fabricated using photolithography. The electrodes are 60 nm thick. 34

**Figure 3.2.** (A) SEM image of gold nanorods deposited in between interdigitated electrodes. The bright area at the top of the image is a gold electrode, as indicated by the arrow. The scale bar is 1  $\mu\text{m}$ . A higher magnification image of a single nanorod is shown in the inset where the scale bar corresponds to 100 nm. (B) Size distribution of two different gold nanorod samples used in this experiment as determined by TEM. The average sizes are  $(28 (\pm 5) \times 76 (\pm 10))$  nm and  $(35 (\pm 8) \times 60 (\pm 15))$  nm. The inset shows the distribution of aspect ratios for these nanorods. The average aspect ratios are 1.7 and 2.7. (C) Ensemble extinction spectra of the two nanorod samples measured with a Shimadzu UV-3101PC spectrophotometer with water as the solvent. 35

**Figure 3.3.** (A) Transmitted light microscope image of a liquid crystal cell in between two crossed polarizers. The sample is mounted in such a way that the nematic director of the liquid crystal is parallel to one of the polarizer axes. (B) Same as (A) while applying an AC electric field of 6 V and 1 kHz. The gaps between the electrodes now appear brighter because of the electric field induced reorientation of the liquid crystal director causing a change of the transmitted light polarization allowing more light to pass through the second polarizer. The liquid crystal molecules between the electrodes are switched in-plane from parallel (voltage off) to perpendicular (voltage on) with respect to the electrode array while the liquid

crystal molecules close to the glass coverslip retain their initial orientation due to strong anchoring by the polyimide alignment layer. This results in the formation of a twisted nematic phase in which the director changes direction by  $90^\circ$  from one side of the cell to the other. The change in contrast in these transmitted light microscope images is consistent with this phase transition of the liquid crystal in response to the applied electric field and hence demonstrates the successful operation of this liquid crystal cell.

37

**Figure 3.4.** Extinction spectrum of an empty cell. From the interference fringes due to multiple reflections at the glass interfaces a cell gap of  $14.2 \pm 0.5 \mu\text{m}$  is obtained.

38

**Figure 3.5.** Transmitted light dark-field microscope setup. The sample is excited with unpolarized light from a lamp. The polarized plasmon scattering passes through the liquid crystal and is collected by an objective. After going through a pinhole to spatially select individual nanorods and a polarizer, the scattered light is detected either by an avalanche photodiode detector or a CCD camera. The signal from the avalanche photodiode detector is fed into a counterboard (Becker&Hickl), which is synchronized to the signal applied to the liquid crystal cell using a set of three function generators. One of the function generators supplies the voltage modulation for the sample (square wave with 4 – 8 V and 1 Hz). To accurately determine the beginning and end of the square pulses, marker pulses are sent from a second function generator to another channel of the counterboard. These two function generators are synchronized by a master function generator.

39

**Figure 3.6.** (A, B) Geometry of the interdigitated electrode array as illustrated by a schematic drawing (A) and a reflected light microscope image (B) of an array fabricated on glass using photolithography. The

bright areas in (B) are the electrodes (scale bar corresponds to 50  $\mu\text{m}$ ). The nematic director of the liquid crystal 5CB is orientated parallel to the electrodes without an applied electric field. (C) Scheme of the experimental setup showing the direction of light propagation and sample geometry. (D, E) Polarized dark-field scattering images of single gold nanorods located in the electrode gaps and covered with 5CB. The detected light polarizations are chosen to be parallel (white) and perpendicular (green) to the electrode array as indicated by the arrows. (F, G) Same as (D, E) recorded with an applied electric field (6V, 1 kHz).

45

**Figure 3.7.** (A, B, C) Polarized dark-field scattering spectra of individual gold nanorods with (blue) and without (red) an electric field (6 V, 1 kHz). The polarizer is set parallel to the electrodes, causing the nanorods in (A) and (B) to appear bright and dim at 0 V, respectively. At 6 V the behavior is reversed as the direction of the scattered light polarization  $\phi$  is rotated by  $90^\circ$ . This is further evident from the insets showing the scattering intensity as a function of polarizer angle. For the nanorod in (C), the change in  $\phi$  is also  $90^\circ$ . However, because the initial polarization for 0 V is not aligned with the polarizer, a reduced intensity modulation of the scattering spectra is observed. (D) Orthogonal polarization rotation of the plasmon scattering measured for a total of 59 nanorods from two samples with the surface plasmon maximum varying between 680 and 850 nm. The error in determining the polarization is  $\sim 10^\circ$  mainly due to the limited number of polarization angles sampled. The black line is a linear fit with a slope of 0.9, where deviations from ideal behavior are likely due to local imperfections in the liquid crystal alignment and thickness.

47

**Figure 3.8.** Maximum intensity modulation achieved from individual nanorods as a function of their apparent orientation in the homogeneous liquid

crystal phase. The intensity modulation is calculated by placing the polarizer along the apparent orientation of the nanorods in the voltage off state, which is achieved by maximizing the scattering intensity by varying the polarizer angle. The modulation depth is then obtained as  $(I(V_{\text{off}}) - I(V_{\text{on}})) / I(V_{\text{off}})$ . These results demonstrate highly efficient plasmon modulation for all nanorods independent of their orientation.

48

**Figure 3.9.** (A, B, C) Reversible polarization rotation at a 1 Hz modulation frequency recorded using a 6 V square waveform and a 5 ms bin time. Time transients of the integrated scattering intensity are recorded using single photon counting detectors with two orthogonal polarizations (black: parallel; green: perpendicular with respect to the electrode array) for nanorods having apparent initial orientations and surface plasmon resonance maxima of 10° and 725 nm (D), 80° and 761 nm (E), and 60° and 809 nm (F). (D, E, F) Same as (A, B, C) but averaged for one cycle of the applied square waveform, yielding response times of  $20 \pm 10$  ms and  $170 \pm 40$  ms for on and off switching, respectively. The intensities in each channel are corrected for background scattering and then normalized by dividing by the total intensity, i.e. sum of both channels.

49

**Figure 3.10.** Background scattering from the liquid crystal solvent 5CB recorded at a 1 Hz modulation frequency using a 6 V square waveform and a 5 ms counterboard bin time. The black and green lines show the intensities for polarization parallel and perpendicular with respect to the electrode array. The fast rise ( $25 \pm 10$  ms) and slow relaxation ( $200 \pm 50$  ms) times of the liquid crystal are calculated by fitting the intensities with an exponential function. These response times are in good agreement with the corresponding values measured for the intensity modulation of the polarized scattering from the individual

nanorods.

51

**Figure 3.11.** Effect of the electric field on the polarization direction of the light scattered by single gold nanorods in air. This cell is prepared in the same way as the liquid crystal samples except that no liquid crystal is injected into the cell. (A, B) represent polarized images of single gold nanorods without an electric field. (C, D) represent polarized scattering images with an applied electric field of 10 V. No change in the scattered light polarization and no physical rotation of the nanorods are observed.

52

**Figure 3.12.** Effect of the electric field on the polarization direction of the light scattered by single gold nanorods in water. This cell is prepared in the same way as the liquid crystal samples except that water is injected into the cell instead of the liquid crystal solvent. (A, B) represent polarized images of single gold nanorods without an electric field. (C, D) represent polarized scattering images with an applied electric field of 10 V. No change in the scattered light polarization and no physical rotation of the nanorods are observed

53

**Figure 3.13.** Effect of the electric field on the polarization direction of the light scattered by single gold nanorods in 5CB when the cell is placed upside down. (A, B) represent polarized images of single gold nanorods without an electric field. (C, D) represent polarized scattering images with an applied electric field of 6 V. The experimental geometry is given in (E). No change in the scattered light polarization is observed. The reduced contrast in the dark-field scattering images compared to Figure 3.6 is because of the use of a lower NA objective (Zeiss LD Achromplan, 40X, 0.60 NA) that can image through the thicker glass slide.

53

**Figure 3.14.** Nematic to isotropic phase transition of the liquid crystal 5CB. The images are taken with an optical microscope employing a bright-

field transmitted light geometry. The liquid crystal director of the sample is aligned at  $45^\circ$  with respect to two crossed polarizers. In the nematic phase, the liquid crystal acts as a birefringent material rotating the polarization of the incident light and hence giving a bright contrast in (A). When the liquid crystal is heated above the nematic to isotropic phase transition, the liquid crystal is no longer birefringent and most of the light is blocked by the second polarizer resulting in the dark image shown in (B). The nematic to isotropic phase transition is induced by resistive heating of the liquid crystal cell with an AC electric field of 5 V and 1 kHz, which is accomplished by using an indium tin oxide coated coverslip to construct the liquid crystal cell. The length of the scale bar is 100  $\mu\text{m}$ .

54

**Figure 3.15.** (A ,B, C) Polarized dark-field scattering images recorded without (A) and with (B) an electric field, and after melting the liquid crystal to its isotropic phase (C). The direction of the scattered light polarization is determined from measurements of the intensity vs. polarizer angle for particle 1 (D) and 2 (E) and for  $V_{\text{off}}$  (red),  $V_{\text{on}}$  (blue), and the isotropic phase (cyan). The vertical lines in (D, E) and the arrow in (A) indicate the polarizer angle used for recording the images. (F, G) Dependence of the detected light polarization on the actual nanorod orientation for  $V_{\text{off}}$  (F) and  $V_{\text{on}}$  (G) (black symbols). The nanorod orientation corresponds to the polarization direction in the isotropic phase, i.e. the incident polarization. The polarization varies as  $180^\circ - \phi$  for  $V_{\text{off}}$  (F) and  $90^\circ - \phi$  for  $V_{\text{on}}$  (G), resulting in an overall orthogonal polarization rotation independent of the nanorod orientation  $\phi$  (H). This orthogonal polarization rotation is due to an electric field induced transition from a homogeneous to a twisted nematic phase (I, J), which is confirmed by calculations (F-H, solid lines) and transmission measurements

using linearly polarized light at  $800 \pm 20$  nm from a lamp (F-H, colored symbols).

56

**Figure 3.16.** Modulation depths of single gold nanorods as a function of their apparent orientation without (A) and with (B) an applied electric field. The modulation depth  $M$  is calculated by fitting the measured scattering intensity vs. polarizer angle dependence for each individual gold nanorod with  $I(\theta) = N(1 + M \cos 2(\theta - \phi))$  where  $\theta$  is the polarizer angle and  $\phi$  is the apparent orientation of the nanorod.

59

**Figure 3.17.** Calculated modulation depth and the polarization angle of the detected light is plotted against the incident polarization for homogeneous (A, C) and twisted nematic (B, D) liquid crystal phases of different thickness and incident light wavelength. The calculation was performed using Jones matrices for homogeneous and twisted nematic phases.

60

**Figure 4.1.** Scheme of sample scanning confocal microscope. Samples were excited by a circularly polarized 532 nm laser source focused by a high numerical aperture oil immersion objective. Linearly polarized fluorescence is divided by a polarization beam splitter (PBS) and collected by two avalanche photodiode (APD). Fluorescence images are acquired by scanning the sample across the laser beam with the scanning stage.

68

**Figure 4.2.** (A) Dye labeled four-wheeled nanocar. The vertices in the carborane wheels correspond to B-H units while the black dots correspond to C and C-H units, ipso and para, respectively. The nanocar is  $\sim 2 \times 2$  nm and the dye “trailer” is  $\sim 1 \times 1$  nm. (B) Fluorescence image ( $10 \mu\text{m} \times 10 \mu\text{m}$ ,  $128 \times 128$  pixels, 1 ms/pixel,



$\lambda_{\text{exc.}} = 532 \text{ nm}$ ,  $1 \text{ kW/cm}^2$ ) of single nanocars. (C-F) Time-lapse images ( $2.3 \text{ } \mu\text{m} \times 2.3 \text{ } \mu\text{m}$ ) for the nanocar circled in (B) demonstrating movement of the nanocar at room temperature. The red cross hair provides a stationary reference point.

69

**Figure 4.3.** Analyzed images of nanocar (A) and TRITC (B). Molecules were identified based on intensity and size within the region marked by the red box. The positions of the molecules for a time series of images are shown superimposed on the first frame. 25% of the nanocars showed displacements greater than the error of 100 nm in at least two image frames and are color coded in red as ‘moving’ nanocars. (C) Single molecule trajectory of the nanocar indicated by the red circle in (A). Displacements as large as 500 nm between frames far exceed the changes in position recorded for the representative TRITC molecule labeled with the green circle in (B) (upper left hand corner in (C); note the scale bar). (D) Squared displacements  $SD$  ( $r^2$ ) calculated from the single nanocar trajectory in (C) vs. time. A linear fit according to  $SD = 4dt$  yields a squared displacement rate  $d$  of  $6.7 \times 10^{-16} \text{ m}^2/\text{s}$ . The inset shows a scatter plot of the linear displacements between images for each of the five ‘non-moving’ molecules in (A). The 11 nm shift between the blue and red points, corresponding to the origin and the mean position, confirms a negligible sample drift.

71

**Figure 4.4.** Directionality of nanocar movement. To evaluate if the nanocars showed motion with a preferential direction, we calculated the angular displacements  $\theta$  (Inset) from unidirectional translation using the single molecule trajectories. The equal distribution over all possible values of  $\theta$  indicates movement in all directions without a bias for directional motion. Translation along a straight line would result in a histogram that is peaked at zero.

73

**Figure 4.5.** (A) Polarization anisotropy distribution of ‘moving’ four-wheeled nanocars (red bars). The polarization anisotropy values are peaked at zero, indicating rotation of the nanocars during the image acquisition time. Rotation much faster than the acquisition time would result in the distribution given by the green line for shotnoise limited polarization detection. The black points and line are a simulation of the polarization anisotropy distribution for random hopping with a minimum rate of 10 hops per second, assuming an equal weight for all hopping directions. (B) Polarization anisotropy distribution of TRITC confirming the absence of rotational motion during the image acquisition time. (C) Mean squared displacement  $MSD$  ( $\langle r^2 \rangle - \langle r \rangle^2$ ) vs. time for all ‘moving’ nanocars. A linear fit according to  $MSD = 4Dt$  yields a two-dimensional diffusion constant  $D$  of  $2.7 \times 10^{-16} \pm 0.4 \text{ m}^2/\text{s}$ . The inset shows a histogram of single molecule squared displacement rates  $d$  calculated from individual trajectories such as the one shown in Figure 4.3D. (D) Distribution of speeds of individual ‘moving’ nanocars. The average speed of the nanocars is 4.1 nm/s or two nanocar lengths per second.

74

**Figure 4.6.** Polarization anisotropy distribution of ‘moving’ four-wheeled nanocars. The polarization anisotropies were calculated by integrating over the area of the single molecules (5x5 pixels, red bars) and the center pixel with the highest intensity only (black line). Because of the scanning image acquisition, the different integration areas correspond to integration times of 500 ms and 1 ms, respectively. The polarization anisotropy distributions are peaked at zero indicating depolarization due to rotational movement. However, the larger width in the polarization anisotropy distribution for the center pixel suggests that rotational dynamics occur on the 1-100 ms time.

75

**Figure 4.7.** (A) Schematic comparison of a carborane wheel rolling (top) vs. hopping (bottom). A wheel on the glass surface forms three hydrogen bonds with the oxygen atoms (not shown for clarity) of the SiO<sub>2</sub>. For rolling only one of the three hydrogen bonds has to break while for hopping the whole wheel has to detach from the surface. (B) Dye labeled three-wheeled nanocar. (C) Three representative polarization anisotropy time trajectories for trimer nanocars showing that rotational motion is absent on a time scale of several minutes. Similar results were also obtained for polarization measurements of ‘non-moving’ four-wheeled nanocars and TRITC only. 77

**Figure 4.8.** Polarization anisotropy distribution of three-wheeled nanocars. The equal distribution of polarization anisotropies over the entire region from -1 to +1 indicates the absence of rotational movement of the trimer nanocars within the acquisition time of 500 ms. 79

**Figure 5.1.** AFM images (1 μm x 1 μm) of plasma cleaned glass (A), etched glass (B), and Vectabond<sup>TM</sup> treated glass (C). The insets show line scans taken on each surface. The average surface roughness of these surfaces was measured to be 0.4 ± 0.1 nm (glass), 2.6 ± 0.2 nm (etched glass), and 0.5 ± 0.2 nm (Vectabond<sup>TM</sup> treated glass). The error was determined from several independent areas of the same and different substrates. Surface holes (dark spots) are seen for Vectabond<sup>TM</sup> treated surfaces, which are as big as 50 nm in diameter and 5 nm in height. They are most likely due to an uneven surface functionalization, but contribute at most 3 % to the total surface area. 85

**Figure 5.2.** Chemical structure of the TRITC-tagged (left) and BODIPY-based (right) nanocar with p-carborane wheels, where the black dots indicate the para-carbon atoms. 87

**Figure 5.3.** (A) First of a time series of fluorescence images for single nanocars on a plasma cleaned glass substrate. Individual nanocars indicated by the red circles were identified based on a threshold intensity. (B) XY trajectories of the nanocars identified in (A). Trajectories colored red and green indicate “moving” and “stationary” nanocars, respectively. (C) Squared displacements  $SD$  vs. time  $t$  calculated from the single nanocar trajectory surrounded by the green dotted square in (B). A linear fit according to  $SD = 4Dt$  gives a diffusion constant  $D = 4.6 \times 10^{-16} \text{ m}^2/\text{s}$ . 88

**Figure 5.4.** (A) Distribution of single-molecule diffusion constants  $D$  for the moving BODIPY nanocars on glass (bars). For comparison, the histogram of diffusion constants for a TRITC-tagged nanocar with carborane wheels moving on a glass surface is also included (line). The mean diffusion constants are nearly identical with  $\langle D \rangle = 2.4 \times 10^{-16} \text{ m}^2/\text{s}$  and  $\langle D \rangle = 2.2 \times 10^{-16} \text{ m}^2/\text{s}$ , for the BODIPY-based and TRITC-tagged nanocars, respectively. (B,C) Histograms of diffusion constants for nanocars on reactive ion etched and amine-terminated glass.  $N_m$  and  $N_s$  are the number of moving and stationary nanocars. 90

# CHAPTER 1

## INTRODUCTION

### 1.1. Motivation and background

The coherent oscillations of the conduction band electrons in noble metal nanoparticles, also known as surface plasmons,<sup>1</sup> result in unique optical properties which have attracted a lot of interest. One of the most visually striking examples of these optical properties of metal nanoparticles is the Lycurgus Cup, which appears in different colors depending on the mode of light illumination: reflection of light vs. transmission of light. Optical properties of plasmonic nanoparticles not only depend on their shape and size but also on their spatial arrangements.<sup>2-6</sup> When nanoparticles are closely spaced, plasmon coupling among them allows one to perform surface enhanced spectroscopies, sensing, as well as receiving and transporting optical information below the diffraction limitation of light.<sup>7-12</sup> Assembly of nanoparticles also enables the construction of optical metamaterials with unique optical properties which are not seen in nature, such as negative refractive index.<sup>13,14</sup>

A number of techniques for organizing metal nanostructures have been developed over the past two decades. These can be divided into two broad categories, (1) top down fabrication methods and (2) bottom up approach. Top-down fabrication techniques<sup>15</sup> include, for example, photolithography, electron-beam lithography, or focused ion beam milling. These techniques have been used extensively to prepare solid state features as small as several tens of nanometers and can be repeated periodically over several micrometers<sup>7,16,17</sup>. Although these techniques are well established and very reliable, severe requirements such as clean-room processing are involved and the overall process

is often time consuming and expensive. Also, it is difficult to reproducibly make periodic nanostructures with gaps smaller than 10 nm<sup>16</sup>.

As a complementary technique, bottom up processes where small building blocks are assembled to make functional materials have attracted a lot of attention. Among different self-assembly techniques, template directed assembly techniques are one of the most efficient and widely used techniques to assemble plasmonic nanoparticles<sup>18</sup>. An example of a template driven assembly is the formation of rings of nanorods developed by Zubarev and coworkers.<sup>19</sup> Using the “breath figure” method, they demonstrated the synthesis of rings with diameters of up to several micrometers which have been shown to have efficient plasmon coupling among the constituent nanoparticles.<sup>20</sup> Using a droplet evaporation method, large-area 3D ordered assemblies of different nanostructures have also been synthesized.<sup>21</sup> Other commonly used templates include complementary DNA molecules, polymers, and biological species.<sup>22-24</sup>

There has also been a great interest in using liquid crystals as potential template materials as they possess long range, three dimensional and switchable order, making it possible to change the orientation of nanomaterials through the liquid-crystal mediated rearrangement of the solvated nanomaterials in response to an applied field such as electric or magnetic fields. Indeed, liquid crystal induced ordering of nanomaterials such as carbon nanotubes, polymers, and semiconductor nanorods have been demonstrated over the last few years.<sup>25-27</sup>

Apart from their application as dynamical templates for organizing nanomaterials, nematic liquid crystals also hold great promise for achieving active control over optical properties of plasmonic nanomaterials because of their large refractive index

anisotropy.<sup>28</sup> The average orientation of the rod-like liquid crystal molecules, commonly defined as the nematic director, can be reversibly switched by applying an external electric or magnetic field. Reorientation of the liquid crystal molecules leads to a change in the local refractive index, which in turn can result in a shift of the surface plasmon resonance.<sup>29-33</sup> Anisotropic nanostructures such as conjugated polymer chains, carbon nanotubes, or semiconducting nanorods have been solvated in a liquid crystal matrix with a preferential alignment parallel to the average orientation of the liquid crystal molecules. For polarized excitation and detection, field induced reorientation of the liquid crystal molecules and hence the nanostructure solute can cause an intensity modulation of the anisotropic optical response.<sup>26,27</sup>

The major challenge of using liquid crystals as templates for plasmonic nanoparticles involves their low solubility in nematic liquid crystals. Compared to small semiconductor nanorods or carbon nanotubes, larger anisotropic plasmonic nanoparticles such as gold nanorods are sparsely soluble in nematic liquid crystal solvents. Until now, this has prevented the realization of active plasmon modulation based on the rotation of anisotropic plasmonic nanostructures due to field induced reorientation of the nematic director. However, the necessity for an active control of the plasmonic response still motivates the search for innovative strategies using nematic liquid crystals.

The bottom up assembly approach, which utilizes small building blocks to build functional materials, also presents novel possibilities for the design and synthesis of nanoscale functional materials. Nature has developed a working molecular nanotechnology that it uses in a number of significant biological processes.<sup>34</sup> A classic

example of such nanoscale functional materials or “molecular machines” is kinesin which transports molecules within a cell.<sup>35,36</sup>

Inspired by Nature’s approach, chemists have synthesized a number of synthetic molecular machines resembling macroscopic elevators, rotors, shuttles, ratches, turnstiles, muscles, and scissors over the last few years.<sup>37-45</sup> A recent addition to the list of molecular machines is nanocars which are synthesized by Tour and coworker.<sup>46,47</sup> These molecules consist of four spherical fullerene or carborane wheels attached to an aromatic chassis thus resembling macroscopic cars and are hence called nanocars. These molecular machines are designed for targeted transport of materials over solid surfaces.<sup>46</sup>

Ensemble measurement techniques very often fail to resolve the action of molecular machines due the averaging of the randomly oriented molecules. This is particularly problematic for measuring the movement of individual nanocars. Scanning tunneling microscopy (STM) was successfully applied to resolve the thermally activated nanometer-scale movement of fullerene-wheeled nanocars on a gold surface.<sup>48</sup> Although STM is a very powerful technique in resolving atomic scale details of individual molecules, the experimental conditions are often less ideal. For example, STM imaging is time-consuming, needs a conductive substrate, and often needs high vacuum conditions to obtain images.<sup>49</sup>

Also, for the effective application of nanocars as cargo vehicles for transporting molecules it is desirable to have controllable and directional motion at ambient temperature. The previous study on fullerene wheeled nanocars on a gold surface using STM reveals nanometer-scale movement of nanocars only at very high temperatures.<sup>50</sup> It is obvious that the motion of nanocars will greatly depend on the nature of the



interactions between the surface and the nanocars and especially the wheels. It is therefore necessary to systematically study the motion of nanocars as a function of the chemical nature of the substrate as well as the wheels of the nanocars.

In this thesis, the microscopic ordering and motion of nanomaterials is studied using various optical techniques including dark field microscopy and scanning confocal microscopy. Dark field microscopy utilizes the scattered light from the probe against a dark background. In principle, any particle that scatters light can be visualized by dark field microscopy. Metal nanoparticles are strong scatterers of light because of the surface plasmons. This makes dark field microscopy a very widely used technique to characterize metal nanoparticles and nanospheres. Nanoparticles as small as 30 nm in diameter can be visualized by this technique.<sup>51</sup>

While dark field microscopy is very useful for characterizing metal nanoparticles, which are usually made of thousands of atoms, it cannot be applied to visualize single molecules because of their very low scattering cross section. Single molecules can be visualized by probing either their absorption or fluorescence. Absorption based techniques include direct absorption measurements as well as indirect photothermal imaging.<sup>52,53</sup> A direct absorption measurement, as first shown by Sandogdhar and coworkers, has a simple set up which essentially mimics a conventional UV-VIS spectrometer.<sup>52</sup> However, the signal to noise (S/N) ratio achievable with this technique is very low for any practical application. Photothermal imaging, on the other hand measures the absorption of single molecules by probing the change of the refractive index of the material surrounding them as a result of local heating caused by the absorption of light.<sup>53</sup> This technique gives single molecule images with higher S/N compared to the direct

absorption measurement and is also unaffected by scattering from impurities. However, photothermal imaging uses a very high power probe laser beam which can lead to photo-damage of the single molecules.

Fluorescence visualization is the most widely used technique to visualize single molecules. Fluorescence is red shifted from the excitation laser wavelength and thus can be easily separated from the background scattering thus achieving a very high S/N ratio.<sup>54,55</sup> Both wide-field as well as confocal scanning techniques are used to acquire images of single molecule. Wide field techniques use a CCD camera to image a big area (typically several tens of micrometers) and to acquire images as fast as tens of millisecond, which makes it very useful to study faster dynamics.<sup>56</sup> While in confocal mode either a tightly focused laser is scanned across the sample (laser scanning) or the sample is scanned across a fixed laser spot (sample scanning).<sup>57,58</sup>

While fluorescence imaging is the most commonly used technique to probe single molecules, like all optical techniques its resolution is limited by the diffraction limitation of light. In a typical single molecule fluorescence image, individual molecules appear as bright spots with diameters of several hundred nanometers which is almost two orders of magnitude larger than the molecule itself. However, it is possible to locate the position of a single molecule within a few nanometers for larger photon counts.<sup>54,59</sup>

## **1.2 Specific aims:**

### Specific aim 1:

To increase the solubility of gold nanoparticles in a nematic liquid crystal by appropriate surface modification and to study how the presence of nanoparticles alter the properties of the liquid crystal.

### Specific aim 2:

To achieve active control over plasmonic properties of anisotropic metal nanoparticles using nematic liquid crystals.

### Specific aim 3:

To establish micrometer-scale movement of individual molecular machines which consists of spherical carborane wheels attached to an aromatic backbone, commonly known as nanocars, and to study of the mechanism of their movement.

### Specific aim 4:

To investigate various forces that affect the mobility of nanocars and to control the mobility of nanocars by tuning the surface functionalization.

## **1.3 Overview**

This thesis contains chapters that are based on journal publications relevant to the research topic. Chapter 2 describes work on enhancing the solubility of plasmonic gold nanoparticles as big as 6 nm in diameter. It is shown that surface functionalization of gold nanoparticles with a ligand which resembles the structure of the liquid crystal greatly

enhances their solubility in that liquid crystal. The nanoparticle-liquid crystal composite prepared in this way is shown to have comparable stability with the pure liquid crystal but is more responsive towards an external electric field. This work is published in the *Journal of Physical Chemistry*.<sup>60</sup>

Chapter 3 describes the application of a nematic liquid crystal to actively tune plasmonic properties of individual gold nanorods. Specifically, a new approach has been developed to actively modulate the polarized scattering intensities of individual gold nanorods. Nearly 100% modulations, i.e., complete on/off switching has been achieved for all nanorods irrespective of their orientations with a voltage as low as 4.0 V. This modulation is purely an optical phenomenon, which is realized due to an electric field induced transition of liquid crystals from a homogeneous to a twisted nematic phase. This approach can be applied to various metallic nanostructures as well as anisotropic semiconductor nanorods. This work is published in *Nano Letters*.<sup>61</sup>

In chapter 4, single molecule fluorescence imaging is applied to establish the movement of a molecular machine commonly known as nanocars. These molecular machines consist of four carborane wheels connected to an aromatic chassis and hence the name nanocars. It is shown that individual nanocars have a surprisingly high mobility up to several micrometers on a plasma cleaned glass surface even at ambient temperature. It is also seen that only a fraction (~25%) of the nanocars show displacements higher than the localization error that resulted from limited detected photon counts. The movement of the nanocars is found to be consistent with the rolling of its carborane wheels. This work is published in *ACS Nano*.<sup>57</sup>

Chapter 5 focuses on controlling the movement of nanocars. It is shown that the inherently fluorescent nanocars show an almost two times increase in the fraction of moving nanocars compared to the nanocars studied in chapter 4 where a fluorescent dye was attached to the nanocars. It is also shown that the speed as well as the fraction of moving nanocars can be further controlled by changing the nature of the surface over which they are moving. Controlling the mobility is a very important step towards the potential application of transporting nano-materials over solid surfaces. This work is published in the Journal of the Physical Chemistry Letters.<sup>62</sup>

## CHAPTER 2

# PLASMONIC NANOPARTICLES-LIQUID CRYSTAL COMPOSITES <sup>1</sup>

### 2.1 Abstract

We report on the plasmonic properties of 6 nm gold nanoparticles that form highly stable solutions in the nematic liquid crystal 4-cyano-4-*n*-pentylbiphenyl (5CB). The nanoparticles were covalently functionalized with 4-sulfanylphenyl-4-[4-(octyloxy)phenyl]benzoate (SOPB), which resembles the structure of the 5CB molecules. The solubility of these nanoparticles in 5CB was significantly higher than that of conventional alkanethiol-terminated nanoparticles. An 8 nm shift of the surface plasmon resonance was observed when the gold nanoparticles were dissolved in the nematic phase of 5CB compared to the isotropic solution in methylene chloride. Good agreement of the experimental surface plasmon resonance shift with Mie calculations using an adjusted dielectric function for a reduced electron mean free path in small nanoparticles confirmed that the gold nanoparticles are solvated by the liquid crystal molecules. The stability of this composite was verified by repeated temperature cycling between the isotropic and nematic phases. We also investigated the nematic-to-isotropic phase transition temperature and the threshold voltage for the Fredericksz transition in gold nanoparticle doped and undoped liquid crystal devices.

---

<sup>1</sup> This chapter is based on the manuscript entitled “Plasmonic nanoparticles-liquid crystal composites” by Saumyakanti Khatua, Primit Manna, Wei-Shun Chang, Alexei Tcherniak, Eric Friedlander, Eugene R. Zubarev, and Stephan Link, published in *J. Phys. Chem C* **2010**, 114, 7251-7257.

## 2.2 Introduction

Noble metal nanoparticles are of great interest because of their intense tunable absorption and scattering resonances caused by collective oscillations of the conduction band electrons, which are known as surface plasmons.<sup>1</sup> The surface plasmon resonance maximum is very sensitive to the dielectric constant of the surrounding media<sup>63-65</sup>. The large anisotropy of the liquid crystal refractive index is therefore ideally suited for tuning of the plasmon resonance by electric field-induced switching of the liquid crystal director orientation. This has been demonstrated for thin metal films<sup>66,67</sup>, gold nanoparticle arrays,<sup>32</sup> metallic hole arrays,<sup>29</sup> gold nanorods,<sup>31,68</sup> and single gold nanoparticles.<sup>33</sup> Conversely, the shift in the surface plasmon resonance has been exploited to measure the local orientation of the liquid crystal molecules in close proximity to metal nanostructures.<sup>28,69,70</sup> For all these studies, the metal nanoparticles were first immobilized on a solid surface and then covered by the liquid crystal solvent. However, it is also desirable to switch the plasmonic response of anisotropic nanostructures by inducing an electric field-dependent nanoparticle reorientation in the liquid crystal matrix. To realize such a composite material, it is first necessary to uniformly disperse metal nanoparticles within the bulk of a nematic liquid crystal.

Composite materials consisting of liquid crystals doped with nanoparticles have indeed attracted much scientific and technological interest, but mainly because the incorporation of nanomaterials enhances the electro-optical properties of the liquid crystal itself. For example, doping with MgO and SiO<sub>2</sub> nanoparticles has been reported to decrease the threshold voltage of the Freedericksz transition in a nematic liquid crystal due to a decrease in order parameter.<sup>71</sup> Suspending ferromagnetic Sn<sub>2</sub>P<sub>2</sub>S<sub>6</sub> nanoparticles

in a nematic liquid crystal host was found to enhance the dielectric anisotropy of the liquid crystal, which also led to a lower threshold voltage.<sup>72</sup> Within a small composition gap, multi-wall carbon nanotubes increase the nematic-to-isotropic phase transition temperature because of an enhanced ordering of the liquid crystal molecules along the carbon nanotubes.<sup>73</sup>

On the other hand, solvent-induced anisotropic alignment of carbon nanotubes<sup>25,74</sup> and rod-like polymer chains<sup>75,76</sup> by thermotropic liquid crystals has been shown to create high degrees of solute order that scales with the relative difference in size between the solvent and the solute molecules.<sup>77</sup> As the alignment direction of the rod-like solutes is typically parallel to the nematic director, application of an external electric field can be used to tune the anisotropic properties of the solute molecules through a solvent directed reorientation.<sup>25,26</sup> An anisotropic ordering of 2-3 nm gold nanocrystals into chain-like aggregates by discotic liquid crystals was also observed and greatly enhanced the conductivity of the composite material independent of the phase.<sup>78,79</sup> The solubility of gold nanocrystals in this size range can be enhanced by functionalizing the particle surface with ligands that contain mesogenic units resembling the chemical structure of the liquid crystal solvent.<sup>80-85</sup> However, 2-3 nm gold nanoparticle show only a very weak and broad surface plasmon resonance as the strength of the plasmon oscillation strongly depends on the total number of electrons.<sup>1,82</sup> Hence, the optical properties of larger gold nanoparticles with strong plasmon resonances solvated in thermotropic liquid crystals have not been studied in detail.

Here, we report on the plasmonic properties of 6 nm gold nanoparticles in 4-cyano-4-*n*-pentylbiphenyl (5CB). The commonly-used thermotropic liquid crystal 5CB



forms a nematic phase in which the main molecular axis of each liquid crystal molecule is orientated along a common direction, called the nematic director. An increase in temperature causes a transition to the isotropic phase in which any orientational order is lost, while applying an electric field allows one to re-align the nematic director according to the direction of the electric field. The solubility of the nanoparticles was greatly enhanced after the surface capping material was changed to ligands that chemically resemble the liquid crystal molecules. Modeling of the surface plasmon resonance using Mie calculations corrected for small nanoparticle size effects agreed well with the experimental spectra showing that the nanoparticles are homogeneously solvated in the nematic liquid crystal phase. Optical absorption measurements as a function of temperature and applied electric field confirmed the homogeneous solvation of the gold nanoparticles.

## **2.3 Materials and methods:**

**2.3.1 General:** Gold (III) chloride ( $\text{HAuCl}_4 \cdot 3\text{H}_2\text{O}$ ), 1-decanethiol, sodium borohydride, *N,N*-diisopropylcarbodiimide (DIPC) were purchased from Aldrich Chemical Co. 4-mercaptophenol and 4'-octyloxybiphenyl-4-carboxylic acid were purchased from TCI America and Alfa-Aesar, respectively. 4-(*N,N*-dimethylamino)pyridinium-4-toluenesulfonate (DPTS) was prepared by mixing saturated tetrahydrofuran (THF) solutions of 4-(*N,N*-dimethylamino)pyridine and *p*-toluenesulfonic acid at room temperature. Unless otherwise stated, all chemicals were used without any further purification.

**2.3.2 Synthesis of 1-decanethiol-capped gold nanoparticles.** Decanethiol-functionalized gold nanoparticles (~2 nm in diameter) were prepared by two-phase synthesis described by Brust and coworkers.<sup>87</sup> In a typical synthesis 120 mg of gold (III) chloride were dissolved in 10 mL of DI water. In a separate vial 730 mg of tetraoctylammonium bromide were dissolved in 27 mL of toluene. These two solutions were mixed and stirred vigorously until the gold chloride was completely transferred into the organic layer. To this organic layer 65 mg of 1-decanethiol were added. Then, a freshly-prepared aqueous solution of sodium borohydride (123 mg in 8.5 mL water) was added slowly into the mixture. The organic layer turned dark brown during the reduction. After 5 min. of stirring, an excess of methanol was added and the gold nanoparticles were centrifuged at 1200 rpm for 5 min. Purified particles were dissolved in THF and kept as a stock solution.

**2.3.3 Synthesis of monodisperse 6 nm gold nanoparticles.** 10 mg of decanethiol-capped 2 nm gold particles were dissolved in 3g of neat 1-decanethiol. The solution was transferred into an 8 mL vial and capped with a teflon-coated cap. The vial was heated to 175° C and kept at that temperature for 1 hour. During this annealing process the solution became dark red indicating the overall increase in the size of gold nanoparticles. The solution was then treated with excess methanol and the particles were centrifuged at 1200 rpm for 5 min. The precipitate containing decanethiol-capped 6 nm gold nanoparticles was dissolved in THF.

**2.3.4 Ligand exchange of 6 nm gold nanoparticles.** A concentrated solution was prepared by dissolving 1g of 4-mercaptophenol in 2 mL of isopropanol. Gold nanoparticles (10 mg) dissolved in 2 mL of THF were added drop-wise with vigorous

stirring. The mixture was stirred for 12 hours followed by addition of excess hexane and centrifugation at 1200 rpm for 5 min. The precipitate was washed several times with methylene chloride in order to remove the residual organic ligands. The resulting material was treated with iodine in deuterated THF and the supernatant was analyzed by NMR to determine the ratio of mercaptophenol and residual decanethiol ligands. According to the integration of NMR signals the nanoparticles contained 70 % of mercaptophenol ligands in the organic shell.

**2.3.5 Covalent attachment of 4'-*n*-octyloxybiphenyl-4-carboxylic acid to mercaptophenol-functionalized 6 nm gold nanoparticles.** 4'-*n*-octyloxybiphenyl-4-carboxylic acid (20 mg) was dissolved in 3 mL of methylene chloride followed by addition of 10 mg DPTS and 10 drops of DIPC. After 5 min. of stirring at room temperature the mixture became clear and a concentrated dimethylformamide (DMF) solution of nanoparticles (15 mg in 0.3 mL of DMF) were added to the reaction mixture. The color of the reaction mixture turned dark red indicating the covalent coupling of nanoparticles with the carboxylic acid. After 2 hours DPTS and DMF were removed by multiple extractions with DI water. Methylene chloride was evaporated under reduced pressure and the residue was rinsed several times with DMF (poor solvent for the resulting nanoparticles). The particles were dissolved in methylene chloride and residual DMF was extracted with DI water. Then methylene chloride was evaporated and the product was dissolved in dry THF.

**2.3.6 Synthesis of 4-sulfanylphenyl-4-[4-(octyloxy)phenyl]benzoate (SOPB) thiol.** 200 mg of 4'-*n*-octyloxybiphenyl-4-carboxylic acid and 387 mg of 4-mercaptophenol (5 equiv) were dissolved in 5 mL of methylene chloride. To this mixture 200 mg of DPTS

were added followed by a drop-wise addition of 0.5 mL of DIPC. The reaction was monitored by TLC (10 vol. % THF in methylene chloride) where the strongly UV active spot of the carboxylic acid anhydride ( $R_f = 1$ ) disappeared gradually and the product spot appeared ( $R_f = 0.6$ ). After the completion of the reaction the mixture was diluted 3 times with methylene chloride and DPTS was removed by extracting with DI water. The methylene chloride was evaporated under reduced pressure and the residue was treated with excess methanol. The precipitated product was isolated by centrifugation and rinsed several times with methanol. The product was dried under vacuum to yield 220 mg of a light brown powder (80 % isolated yield).  $^1\text{H NMR}$  (400 MHz,  $\text{CDCl}_3$ ):  $\delta$  0.9 (t, 3H), 1.30-1.35 (m, 11H), 1.80 (m, 2H), 3.5 (s, 1H), 4.02 (t, 2H), 6.90 (d, 2H), 7.01 (d, 2H), 7.39 (d, 2H), 7.58 (d, 2H), 7.68 (d, 2H), 8.08 (d, 2H).

**2.3.7 Preparation of gold nanoparticle-liquid crystal composites.** Gold nanoparticle doped liquid crystal composites were prepared by dissolving the nanoparticles and the nematic liquid crystal 5CB (TCI America) in methylene chloride as a common solvent followed by its slow evaporation.<sup>86</sup> Liquid crystal cells were fabricated from two indium tin oxide (ITO) coated glass slides (Delta Technologies) that were separated by a 50  $\mu\text{m}$  thick self-adhesive mylar spacer (McMaster-Carr) and sealed with epoxy glue. PVA alignment layers were spin-cast onto the slides at 3500 rpm and exposed to unidirectional rubbing. The gold nanoparticle-liquid crystal composite was injected into the cell by capillary forces. To avoid a non-uniform liquid crystal alignment, both the cell and the composite were heated to a temperature above the nematic-to-isotropic phase transition temperature before injecting the composite into the cell. Formation of the nematic liquid crystal phase was confirmed by observing birefringence between crossed polarizers.

**2.3.8 Optical absorption measurements.** Optical absorption measurements were performed with a home-built absorption spectrometer consisting of a halogen lamp (Thorlabs OSL1) as a light source, a polarizer, a depolarizer, and a fiber-coupled spectrometer (Ocean Optics S1024DWX). Samples were mounted on a rotation stage to allow for convenient alignment of the nematic director with respect to the polarization axis. Spectra were integrated for 100 ms and averaged 100 times. Because the scattering in the nematic phase varied slightly from sample to sample, we prepared 6 blank 5CB samples and averaged their spectra to obtain a solvent correction file. The same procedure was also applied for measurements in the isotropic 5CB phase. The isotropic phase was prepared by conductive heating with a variable DC voltage (2-5 V) from a power supply (MPJA 14602PS). The temperature was monitored with a thermocouple and digital thermometer (Omega HH26K) and was equilibrated for 10 minutes before taking a measurement. Homeotropic alignment (i.e. alignment perpendicular to the glass surfaces) was induced by applying an AC electric field (sinusoidal wave with frequency of 1 kHz and maximum amplitude of 50 V) across the two ITO coated slides using a function generator (Stanford Research System DS335) and voltage amplifier (Harrison 6824A). For measurements of the nematic-to-isotropic phase transition temperature,  $T_{IN}$ , and the threshold voltage for the Freedericksz transition, the samples were mounted such that the nematic director made a  $45^\circ$  angle with the polarization axis of the incident light and were placed between crossed polarizers instead of the polarizer-depolarizer combination. A second fiber-coupled spectrometer (Ocean Optics USB4000) was used to measure the relative transmittance. The relative transmittance was defined as the transmittance as a function of temperature or voltage integrated over a spectral range

where the plasmon resonance gave only a minor contribution (>625 nm) minus the transmittance at the maximum temperature or voltage applied.

## 2.4 Results and Discussion

In order to study the plasmonic properties of liquid crystal–gold nanoparticle composites, we focused on the preparation of relatively large and near-monodisperse nanoparticles (5-6 nm) that exhibit a significantly larger and narrower absorption in the visible range when compared to their smaller polydisperse analogues (1-3 nm).<sup>87</sup> Although the synthesis of alkanethiol-capped monodisperse gold nanoparticles is known,<sup>88</sup> there are no examples of monodisperse gold particles coated with functional organic molecules. Here we developed a two-step synthetic route which enabled us to transform decanethiol-coated gold nanoparticles (Figure 2.1) into their functional analogues carrying alkyloxybiphenyl thiols that resemble the structure of the nematic liquid crystal 5CB.

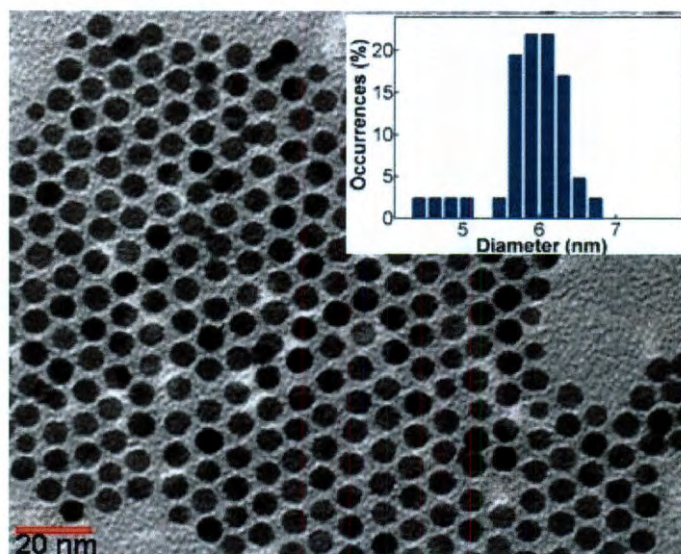
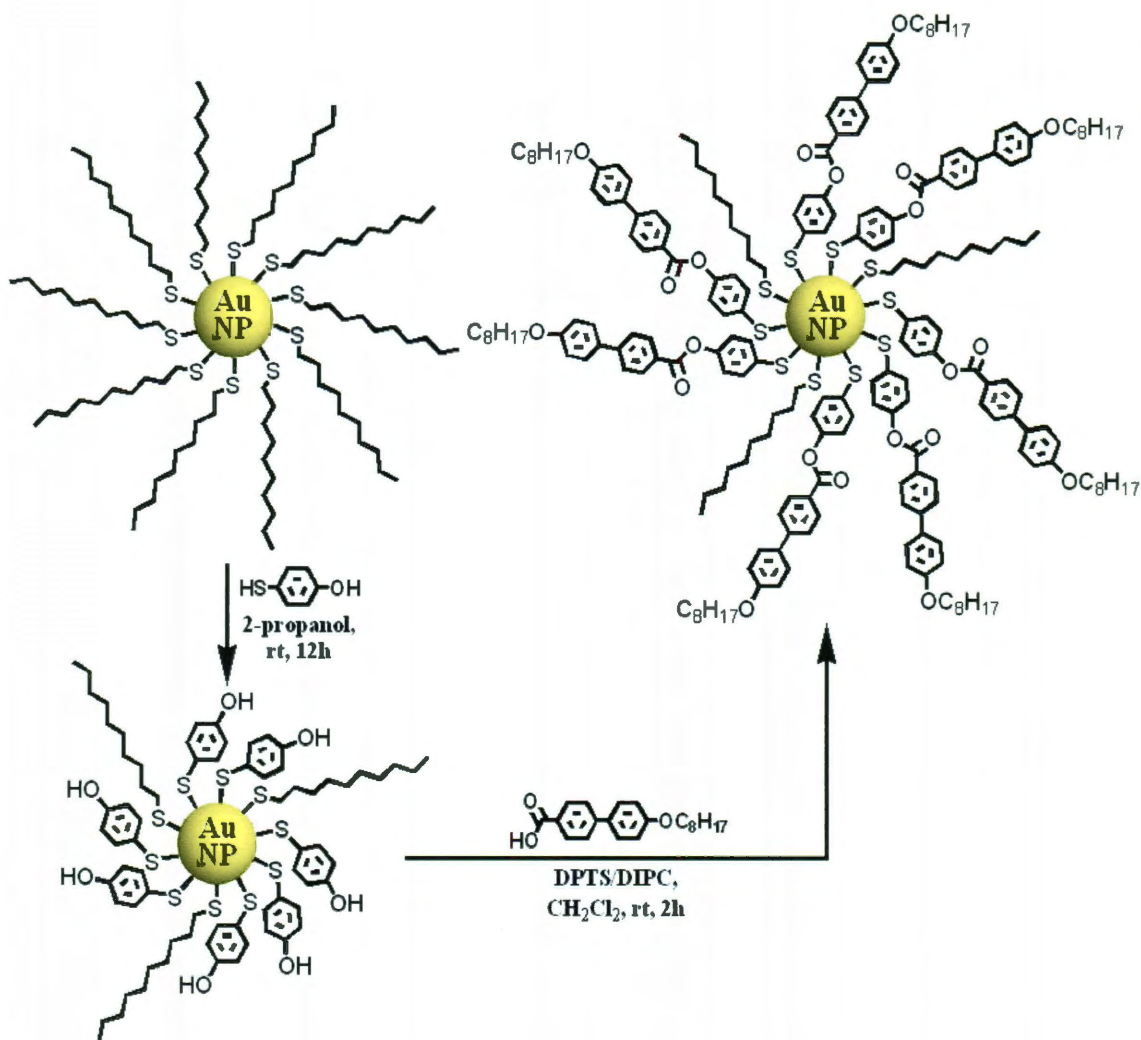


**Figure 2.1.** Transmission electron microscopy image of decanethiol-coated gold nanoparticles. The inset shows the nanoparticle size distribution.



**Scheme 2.1.** Two-step synthesis of SOBP-functionalized gold nanoparticles. Note that the number of ligands attached to the 6 nm gold core is significantly higher (~500) than shown in the scheme.

In the first step outlined in Scheme 2.1 monodisperse decanethiol-coated gold nanoparticles synthesized by literature procedure<sup>88</sup> were treated with a concentrated isopropanol solution of a low molar mass functional thiol 4-mercaptophenol. We found that under these conditions nearly 70% of decanethiol ligands were exchanged for mercaptophenol molecules as determined by <sup>1</sup>H NMR of the organic residue that formed after complete dissolution of gold cores in the presence of iodine. The resulting

nanoparticles became poorly soluble in organic solvents, but retained their narrow size distribution which was similar to that of the starting material (Figure 2.1).

In the second step the mercaptophenol-coated gold nanoparticles were reacted with 4'-octyloxybiphenyl-4-carboxylic acid under mild esterification conditions using DIPC and DPTS as coupling agents. During the coupling reaction the nanoparticles gradually dissolved and formed a stable homogeneous solution in methylene chloride which was indicative of successful covalent attachment of the liquid crystal like 4'-octyloxybiphenyl-4-carboxylic acid ligands. The reaction mixture was purified according to standard procedures published elsewhere<sup>89</sup> and the 6 nm nanoparticles functionalized with SOPB ligands were isolated in a form of a dark red powder with an 80 % yield. The

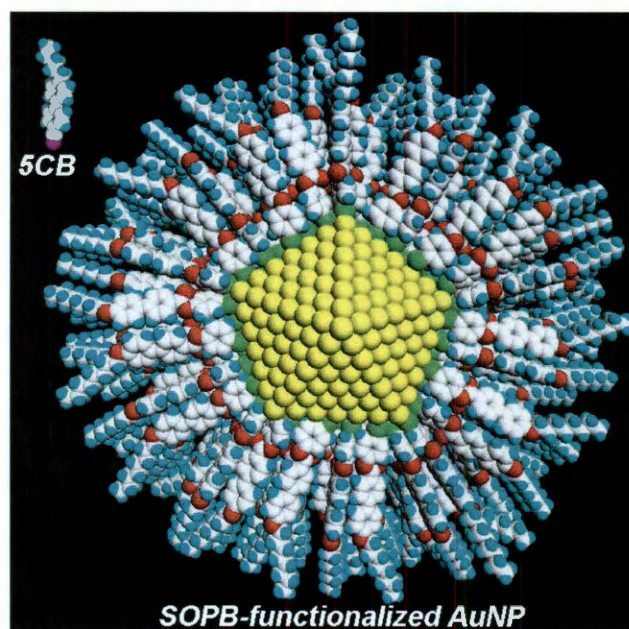


**Figure 2.2.** Molecular graphics representation of a gold nanoparticle functionalized with SOPB thiols. A 5CB molecule is shown for comparison in the upper left corner.

purity of the product was confirmed by a combination of TLC, NMR, and gel permeation chromatography using standard literature protocols.<sup>90</sup> Figure 2.2 shows a molecular



graphics representation of a polyhedral gold nanoparticle functionalized by SOPB ligands and for comparison a molecule of 5CB.

The absorption spectra of decanethiol (blue) and SOPB-functionalized (red) gold nanoparticles in 5CB are compared in the inset of Figure 2.3. The spectra were taken with the maximum possible amount of gold nanoparticles dissolved in the same volume of liquid crystal solvent. The solubility of the decanethiol-coated nanoparticles was very poor as no distinct plasmon peak is observed suggesting that the nanoparticles are actually not solvated inside the 5CB, but rather aggregated at the glass interface. On the other hand, the solubility of SOPB-functionalized gold nanoparticles was much enhanced with a calculated maximum gold nanoparticle concentration of 0.2 wt%. The calculation is based on the experimental optical density (O.D.) at the surface plasmon resonance

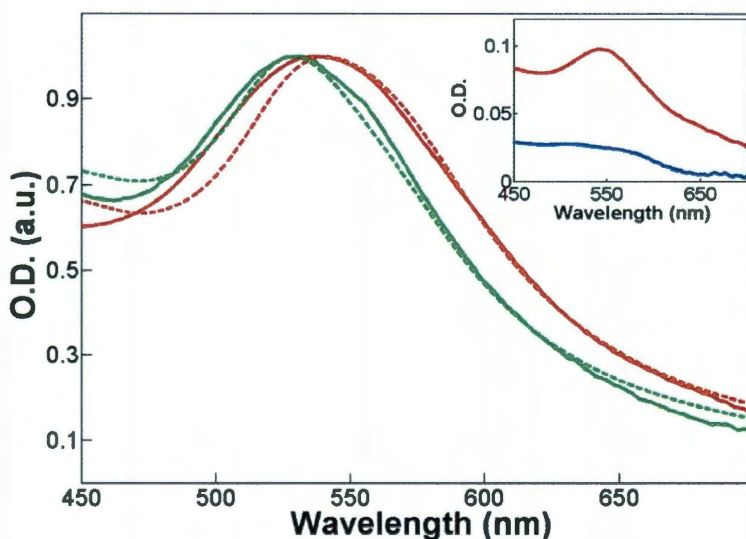


**Figure 2.3.** Experimental (solid lines) and calculated (dashed lines) absorption spectra of SOPB-functionalized gold nanoparticles in methylene chloride (green lines,  $\lambda_{\text{max}} = 531$  nm) and in 5CB (red lines,  $\lambda_{\text{max}} = 539$  nm). The spectra were normalized at the corresponding absorption maxima. The inset compares the absorption spectra of decanethiol- and SOPB-functionalized gold nanoparticles in 5CB (blue and red, respectively). All spectra were taken with the nematic director parallel to the light polarization.

maximum and the known molar extinction coefficient,<sup>91</sup> but was also verified experimentally for these nanoparticles by preparing solutions from a measured amount of solid SOPB-functionalized gold nanoparticle powder. It should be emphasized that the observed optical densities of  $\sim 0.1$  correspond to a path length of only 50  $\mu\text{m}$ . For a 1 mm path length cuvette the O.D. of these nanoparticle-liquid crystal composites would be 2, or 99 % of the incident light absorbed at the plasmon resonance maximum.

The increase in solubility can be explained by the structural similarity of the biphenyl-containing ligands with the 5CB solvent. Complete nematic solvation is further confirmed by the 8 nm red shift of the surface plasmon resonance for SOPB-coated 6 nm nanoparticles in 5CB compared to the isotropic methylene chloride solution (Figure 2.3). The shift of the plasmon resonance maximum is caused by the increase in solvent refractive index<sup>63-65</sup> indicating the successful incorporation of the gold nanoparticles inside the nematic liquid crystal solvent. For comparison, a spectral shift of similar magnitude has been reported for 5 nm alkanethiolate monolayer-protected gold clusters when the solvent refractive index was varied from 1.33 to 1.55.<sup>64</sup> A spectral shift of the plasmon resonance due to particle aggregation can be excluded as a possible explanation here because no distinct shoulder was observed on the red edge of the spectrum<sup>92,93</sup>. In addition, we confirmed that the width of the surface plasmon resonance did not broaden as a function of nanoparticle concentration, indicating no aggregation in the solution or at the glass interface.

The absorption spectra shown in Figure 2.3 were recorded with the nematic director aligned parallel with the polarization axis of the incident light. Rotating the sample 90° to record spectra with a perpendicular orientation of the nematic director as

well as electrically switching the director to a homeotropic orientation had no effects on the absorption of the spherical nanoparticles. Furthermore, as illustrated in Figure 2.4A the absorption spectrum of SOPB-functionalized gold nanoparticles in 5CB showed only a very small shift of  $< 3$  nm when the composite was heated to its isotropic phase

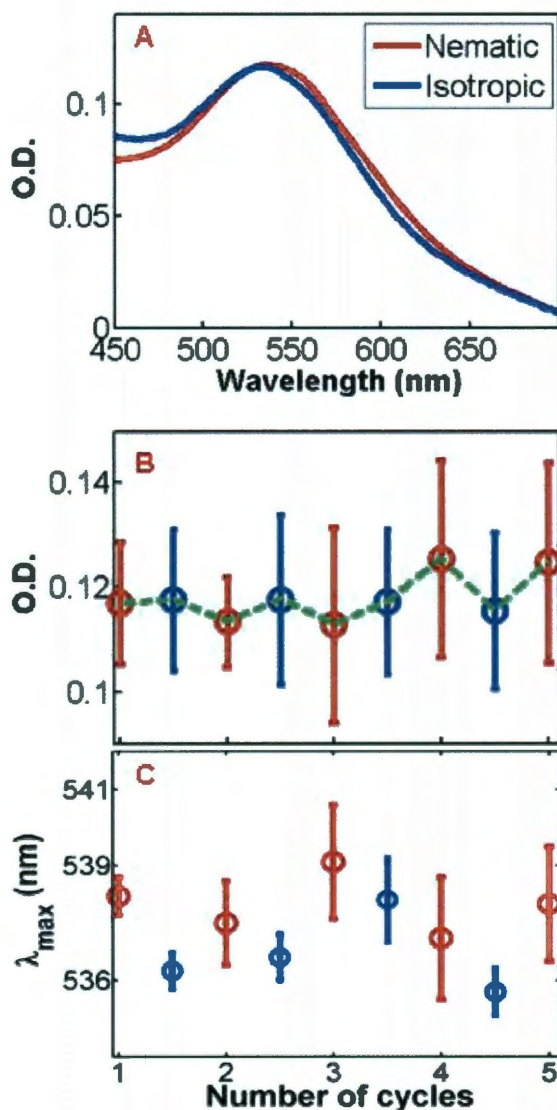


**Figure 2.4.** Absorption spectra of SOPB-functionalized gold nanoparticles in the nematic (red) and isotropic (blue) phases of 5CB (A). The spectra were taken at temperatures of  $T = 25^{\circ}\text{C}$  and  $T = 35^{\circ}\text{C}$ , respectively. Repeated cycling between these temperatures had no effect on the O.D. as measured at the plasmon resonance (B) confirming the stable solvation of the gold nanoparticles inside the liquid crystal. This is furthermore in agreement with the small, but reproducible shift in the plasmon resonance maximum (C).

indicating that the gold nanoparticles experience in the nematic phase a refractive index that is similar to the one of the isotropic liquid crystal. These observations are consistent with the spherical symmetry of the gold nanoparticles and the fact that the particles are in addition free to rotate on the measurement timescale causing the nanoparticles to experience an isotropically averaged environment. The optical measurements therefore confirm the assignment that the nanoparticles are homogeneously solvated by the 5CB molecules. It is important to point out that, as shown by these results, the anisotropy of the liquid crystal refractive index in the nematic phase is not experienced by spherical particles that are isotropically surrounded by the liquid crystal in contrast to previous experiments in which the nanoparticles were immobilized on a substrate.<sup>31-33</sup> The presence of a surface and the absence of free nanoparticle motion hence cause a break in symmetry and allows for the refractive index anisotropy to be experienced by the plasmon resonance.

To further confirm these conclusions, we calculated the absorption spectra of gold nanoparticles in methylene chloride and 5CB using Mie theory.<sup>1</sup> Because of an enhanced electron-surface scattering in metal nanoparticles smaller than the electron mean free path the surface plasmon resonance is strongly damped for the 6 nm gold nanoparticles studied here.<sup>1,94,95</sup> In order to account for the increased plasmon linewidth, we included in the calculations the effect of a reduced mean free path by modifying the damping constant  $\gamma$  of the free electron contribution to the dielectric function according to  $\gamma = \gamma_{bulk} + Av_F / R$ .<sup>1,94</sup>  $\gamma_{bulk}$  represents electron scattering processes for the bulk metal, while the second term accounts for electron-surface scattering, where  $v_F$  is the Fermi velocity of the electrons,  $R$  is the radius of the nanoparticles, and  $A$  is a dimensionless fitting

parameter, which varies between 0 and 1 and describes the nature of the electron-surface scattering.<sup>1</sup> This approach has been successfully used to explain experimentally observed surface plasmon resonance spectra of small gold nanoparticles.<sup>65,96</sup>

We also obtained very good agreement between the experimental (solid lines) and calculated spectra (dashed lines) for 6 nm gold nanoparticles in methylene chloride (green) and 5CB (red) as shown in Figure 2.3. For the refractive index of the solvent we used 1.42 and 1.60 for methylene chloride and 5CB respectively. Because of the spherical symmetry of the gold nanoparticles and consistent with the discussions above, we assumed an isotropic average of the refractive index of 5CB according to  $\langle n_{iso} \rangle = (n_e + 2 n_o)/3$ .<sup>97</sup> The dielectric function of gold was computed using the tabulated values reported by Johnson and Christy.<sup>98</sup> For the  $A$  parameter, we found that a value of 0.25 produced the best match with the experimental spectra in excellent agreement with recent single nanoparticle studies.<sup>99,100</sup> The calculations confirm that the gold nanoparticles are homogeneously solvated. In addition, the calculations also indicate that the co-solvent methylene chloride used in the preparation of the nanoparticle-liquid crystal composites (see experimental section) has been completely evaporated. To further verify the absence of residual methylene chloride that might stabilize the solvation of the nanoparticles in the nematic phase, we also dissolved a dried powder of SOPB-functionalized 6 nm gold nanoparticles directly in 5CB at similar concentrations. The resulting spectra were identical to the ones obtained by using methylene chloride as a co-solvent.

In addition, we tested the stability of the gold nanoparticle-5CB composite by repeated temperature cycling between the nematic and isotropic phases. In Figure 2.4B,

the peak optical densities at the plasmon resonance are plotted for nanoparticle-liquid crystal composites that were consecutively cycled four times between the nematic and isotropic phases at  $T = 25^{\circ}\text{C}$  and  $T = 35^{\circ}\text{C}$ , respectively. The error bars were calculated from three independent measurements from three different samples containing the same amount of SOPB-coated gold nanoparticles. The measured optical densities remained unchanged during the temperature cycling confirming the high stability of the composite. On the other hand, an unstable mixture resulted in a gradual decrease in absorbance upon temperature cycling as observed for the decanethiol-coated gold nanoparticles. The maxima of the plasmon resonance for the same temperature-dependent measurements are shown in Figure 2.4C. The small shift of  $< 3$  nm between the nematic and isotropic phases is reproducible thus further illustrating the thermal stability of the nanoparticle – liquid crystal composite.

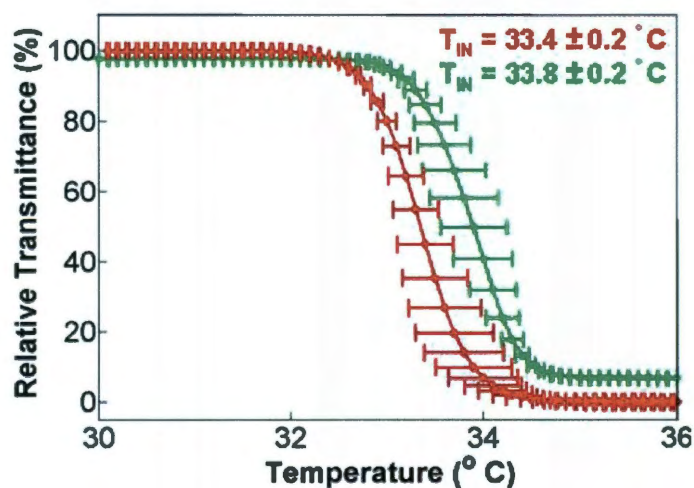


**Figure 2.5.** Nematic-to-isotropic phase transition of neat 5CB (red) and 5CB doped with SOPB-functionalized gold nanoparticles (green). The temperature dependence of the relative transmittance (data points) was fitted with a sigmoidal function (solid lines). Error bars were calculated from three independent measurements.

The presence of nanoparticles in a liquid crystal has been shown to alter the nematic-isotropic phase transition temperature<sup>73</sup> and threshold voltage<sup>71,72</sup> of the pure liquid crystal. Anisotropic solutes such as carbon nanotubes can cause an enhancement of the liquid crystal order and hence an increase in the nematic-to-isotropic phase transition temperature.<sup>73</sup> We measured the phase transition temperature in the presence of spherical gold nanoparticles and compared the results to pure 5CB. As Figure 2.5 shows, the nematic-to-isotropic phase transition temperature slightly increased by 0.4°C. Although this effect is small, it is outside the experimental error bars. The small increase in the phase transition temperature implies a slight increase in the liquid crystal order parameter due to the presence of the gold nanoparticles. A stabilization of the liquid crystalline phase due to local ordering around the nanoparticle solute is indeed expected for rod-shaped nanoparticles as previously observed for multi-wall carbon nanotubes in a nematic liquid crystal.<sup>73</sup> However, the lack of shape anisotropy for the gold nanoparticles suggests that other factors than a change in order parameter could possibly contribute as well to the increase in the phase transition temperature. To investigate the electro-optical

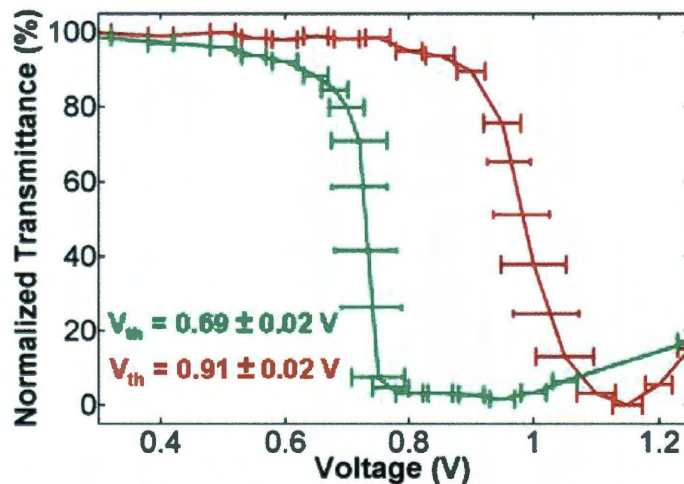


**Figure 2.6:** Fredericksz transition of nanoparticle-doped (green) and undoped (red) liquid crystal devices. The lines connect the experimental points and are included as guides for the eyes only. Error bars were calculated from two independent measurements.

properties of gold nanoparticle doped 5CB devices, we furthermore compared the threshold voltages for the Freedericksz transition for doped and neat liquid crystal cells. The transition of the electric field induced re-orientation of the liquid crystal is known as the Freedericksz transition. The threshold voltage ( $V_{th}$ ) for this transition was measured where the transmission of the cell decreased by 10% of its maximum value.<sup>101</sup> The results are presented in Figure 2.6 and show a decrease of the threshold voltage for the nanoparticles–liquid crystal composite by about 0.22 V. Two previous studies on nanoparticle doped liquid crystal devices also found a decrease of the threshold voltage,<sup>71,72</sup> which was explained by a decrease of the order parameter for MgO and SiO<sub>2</sub> nanoparticle solutes<sup>71</sup> and an enhancement of the liquid crystal dielectric anisotropy in the case of Sn<sub>2</sub>P<sub>2</sub>S<sub>6</sub> nanoparticles.<sup>72</sup> Considering the slight increase in the nematic-to-isotropic phase transition temperature, an enhancement of the dielectric anisotropy due to metallic 6 nm particles is the more likely explanation for the observed trend. To gain further insight into the thermal and electro-optical properties of the nanoparticle doped liquid crystal devices, future measurements will be aimed at directly determining the solvent order parameter.

## 2.5 Conclusions

We have shown that a two-step synthetic replacement of decanethiol with SOPB functional ligands renders 6 nm gold nanoparticles soluble in the nematic phase of 5CB. We demonstrated spectroscopically that the nanoparticles are indeed dissolved rather than dispersed and explain the enhanced solubility by the chemical similarity between the surface capping material and the liquid crystal solvent. The stability of this composite



was further verified by cycling between the isotropic and nematic phases of the liquid crystals. In addition, we found a small increase of the nematic-to-isotropic phase transition temperature of 0.4°C and a desirable decrease of the threshold voltage by about 25% for an electric field induced homeotropic director alignment when a maximum nanoparticle concentration of 0.2 wt% was added to 5CB. These results present an important step towards dissolving nanoparticles with size and shape tunable plasmonic properties inside liquid crystal solvents.

## **2.6 Acknowledgements**

I would like to thank Dr. Prमित Manna and Dr. Eugene Zubarev with whom I collaborated on this project. This work was supported by the Robert A. Welch Foundation (C-1664) and a 3M Nontenured Faculty Grant.

## CHAPTER 3

### ACTIVE MODULATION OF NANOROD PLASMON <sup>1</sup>

#### 3.1 Abstract

Confining visible light to nanoscale dimensions has become possible with surface plasmons. Many plasmonic elements have already been realized. Nanorods, for example, function as efficient optical antennas. However, active control of the plasmonic response remains a roadblock for building optical analogs of electronic circuits. We present a new approach to modulate the polarized scattering intensities of individual gold nanorods by 100 % using liquid crystals with applied voltages as low as 4 V. This novel effect is based on the transition from a homogenous to a twisted nematic phase of the liquid crystal covering the nanorods. With our method it will be possible to actively control optical antennas as well as other plasmonic elements.

---

<sup>1</sup> This chapter is based on the manuscript entitled “Active modulation of nanorod plasmon” by Saumyakanti Khatua, Wei-Shun Chang, Pattanawit Swanglap, Jana Olson, and Stephan Link, published in *Nano Lett.* **2011**, *11*, 3797-3802.

## 3.2 Introduction

The coherent oscillations of the conduction band electrons in metals, known as surface plasmons, offer many unique opportunities ranging from enhancing spectroscopic signals and sensing in nanoscale volumes to receiving and transporting optical information in miniaturized circuits that are much smaller than the incident wavelength.<sup>8,10-12,102-104</sup> Metallic nanoparticles of arbitrary size and shape can be fabricated, thereby making it possible to broadly tune the resonance wavelength of the localized surface plasmon.<sup>2-4</sup> Recent progress in the rational design of coupled plasmonic nanostructures has also shown how surface plasmons on different nanoparticles interact collectively to form hybridized modes with tailored resonances.<sup>5,6</sup> However, in addition to designing complex plasmonic architectures for various applications, new approaches for externally manipulating surface plasmons are still in great demand.

In addition to using electro- and photochromic molecules,<sup>105-108</sup> thermotropic liquid crystals hold great promise for achieving active control over the optical properties of plasmonic nanostructures because of their large refractive index anisotropy,<sup>28</sup> as well as their ability to function as dynamic templates for organizing nanomaterials.<sup>25-27,77</sup> By applying an external electric field, the average orientation of the rod-like liquid crystal molecules, commonly defined by the nematic director, can be reversibly switched. For immobilized nanoparticles, a reorientation of the liquid crystal molecules leads to a change in the local refractive index, which in turn causes a spectral shift of the surface plasmon resonance.<sup>29-32,109</sup> Alternatively, rod-like nanostructures such as carbon nanotubes, semiconducting nanorods, and conjugated polymer chains have been solvated

in a liquid crystal matrix with a preferential alignment parallel to the nematic director.<sup>25-</sup>  
<sup>27,77</sup> For polarized excitation and detection, an electric field induced reorientation of the liquid crystal solvent molecules and hence the nanostructure solute causes intensity modulations of the anisotropic optical response.<sup>26,27</sup>

However, major challenges exist for both of these approaches. In the case of local refractive index modulation, large surface anchoring forces impede a maximum reorientation of the liquid crystal molecules.<sup>28,32,109</sup> The difference in the ordinary and extraordinary refractive indices can be as large as 0.2 for thermotropic liquid crystals<sup>28-30</sup> and should therefore result in spectral shifts of the localized surface plasmon resonance by as much as  $\sim 100$  nm for the most sensitive nanoparticles.<sup>110,111</sup> However, in practice this strategy, applied to supported nanoparticles covered with a liquid crystal solvent, has yielded only modest spectral shifts of 10 – 20 nm for isolated<sup>31,109</sup> and 10 – 40 nm for coupled nanoparticles.<sup>29,30,32</sup>

The challenge for modulating the nanostructure orientation inside a liquid crystal matrix involves low solubility. Compared to small semiconductor nanorods or thin carbon nanotubes, larger plasmonic nanoparticles such as gold nanorods have a much smaller solubility in thermotropic liquid crystal solvents.<sup>57</sup> So far, this has therefore prevented active plasmon modulation based on nanorod rotation due to electric field induced switching of the nematic director. However, because of the mature liquid crystal device technology, the existing need for external control of the plasmonic response still motivates the search for innovative strategies involving thermotropic liquid crystals.

Here we present a new approach, which is not limited by either strong anchoring forces or a low solubility, to externally control the polarized scattering from individual

gold nanorods using liquid crystals. We demonstrate how the intensity of the longitudinal surface plasmon resonance in such optical antennas can be reversibly modulated with 100% efficiency (complete on/off switching) using applied voltages as low as 4 V. We show that this novel intensity modulation is realized by an electric field induced transition from a homogenous to a twisted nematic phase of the liquid crystal 5CB (4-cyano-4-*n*-pentylbiphenyl), which causes an orthogonal rotation of the scattered light polarization independent of the nanorod orientation.

### **3.3 Materials and methods:**

**3.3.1. Materials:** Gold nanorods were purchased from Nanopartz. Two nanorod samples were used and characterized by scanning electron microscopy (SEM) on a FEI Quanta 400 ESEM and transmission electron microscopy (TEM) on a JEOL 2010 TEM. The liquid crystal solvent (4-cyano-4-*n*-pentylbiphenyl) was purchased from TCI America. The photoresist (S1813) was purchased from MicroChem Corporation. The developer solution (MF 321) was bought from Rohm Hass. Polyimide was purchased from Nissan Chemicals (SE 3510). Acetone was purchased from Sigma Aldrich. All chemicals were used as received without further purification.

**3.3.2 Fabrication of interdigitated electrode arrays:** Interdigitated electrode arrays were fabricated over a 1 mm thick glass slide using standard photolithography. A positive photoresist (S1813, Microchem Corporation) was spin-coated (3000 rpm for 45 seconds) on the glass slide followed by a 90 seconds soft baking at 115 °C. The negative of the pattern was then written in the photoresist coated glass by exposure to UV light (Mercury lamp, 365 nm) through a mask (silicon wafer) using a mask aligner (SUSS MJB4).

Exposed photoresist was developed with a developer solution (MF 321, Rohm Hass) and rinsed with deionized water. Gold was evaporated (60 nm thick, with a deposition rate of  $0.1 \text{ nm s}^{-1}$ ) on top of the patterned photoresist using an electron beam evaporator (Telemark). A thin layer of Ti (5 nm) was used prior to the gold evaporation to achieve better adhesion of gold with glass. Once the evaporation was completed, the lift-off was followed immediately using acetone as the solvent. Successful fabrication of the electrode arrays was verified by taking optical and SEM images as well as measuring the resistance. A photograph of an interdigitated electrode array is shown in figure 3.1.

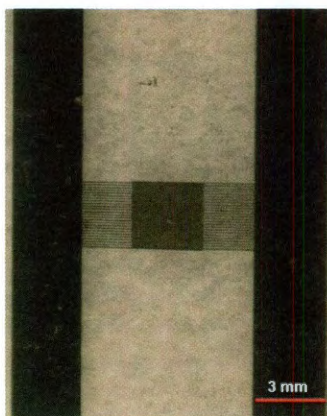


**Figure 3.1:** Photograph of an interdigitated electrode array with  $10 \mu\text{m}$  gaps between electrodes fabricated using photolithography. The electrodes are 60 nm thick.

**3.3.3. Characterization of single gold nanorods:** Gold nanorods (Nanopartz), coated with cetyl trimethylammonium bromide (CTAB), were deposited on the glass slides with the interdigitated electrode arrays by drop casting them from a water solution. Presence of single gold nanorods was confirmed by SEM imaging (Figure 3.2). It is important to mention that exposure to the electron beam damages the surface and prevents the formation of the liquid crystalline phase. For this reason, SEM imaging was performed

only for the characterization of nanorods. These samples were not used in the single particle measurements.

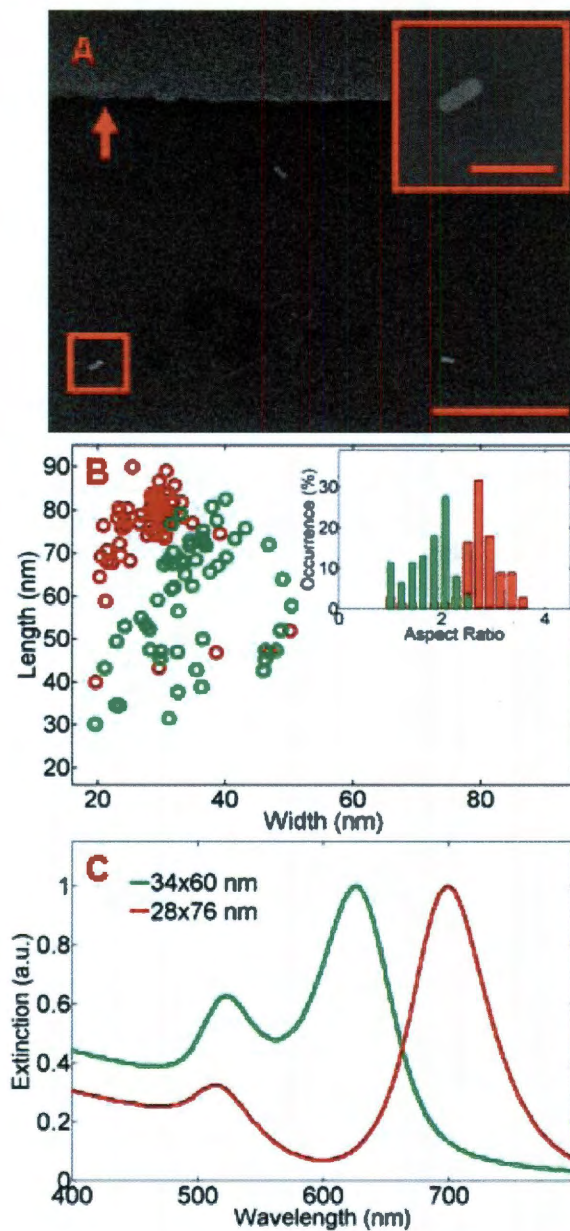


**Figure 3.2:** (A) SEM image of gold nanorods deposited in between interdigitated electrodes. The bright area at the top of the image is a gold electrode, as indicated by the arrow. The scale bar is 1  $\mu\text{m}$ . A higher magnification image of a single nanorod is shown in the inset where the scale bar corresponds to 100 nm. (B) Size distribution of two different gold nanorod samples used in this experiment as determined by TEM. The average sizes are  $(28 (\pm 5) \times 76 (\pm 10))$  nm and  $(35 (\pm 8) \times 60 (\pm 15))$  nm. The inset shows the distribution of aspect ratios for these nanorods. The average aspect ratios are 1.7 and 2.7. (C) Ensemble extinction spectra of the two nanorod samples measured with a Shimadzu UV-3101PC spectrophotometer with water as the solvent.

**3.3.3. Liquid crystal cell assembly:** A glass coverslip (0.13 mm thick, Fisher Scientific) was coated with a polyimide alignment layer and rubbed unidirectionally with a lens cleaning tissue. A liquid crystal cell was prepared by gluing the glass slide and coverslip together with Torr seal in such a way that the polyimide rubbing direction was parallel to the electrodes. Liquid crystal (5CB, TCI America) was then inserted into the cell by capillary action while heating to a temperature above the nematic to isotropic phase transition temperature. After the liquid crystal insertion, the cell was very slowly cooled down to room temperature.

The alignment of the liquid crystal and its response to the electric field was verified by taking polarized microscopy images (Zeiss Axioplan 2). Switching of the liquid crystal alignment, as shown in Figure 3.3, was achieved by applying an electric field of 4 - 8 V across the electrodes. This electric field strength is consistent with values reported for the electric field induced Freedericksz transition of 5CB.<sup>26,30</sup> The electric field was generated by a sinusoidal wave with a 1 kHz frequency using a function generator (Fluke 271 DDS). This frequency is faster than the liquid crystal response time leading to a static orientation of the liquid crystal.<sup>26</sup> An AC voltage was preferred over a DC voltage to eliminate the possibility of charge migration and build-up at the electrodes due to the presence of impurities.



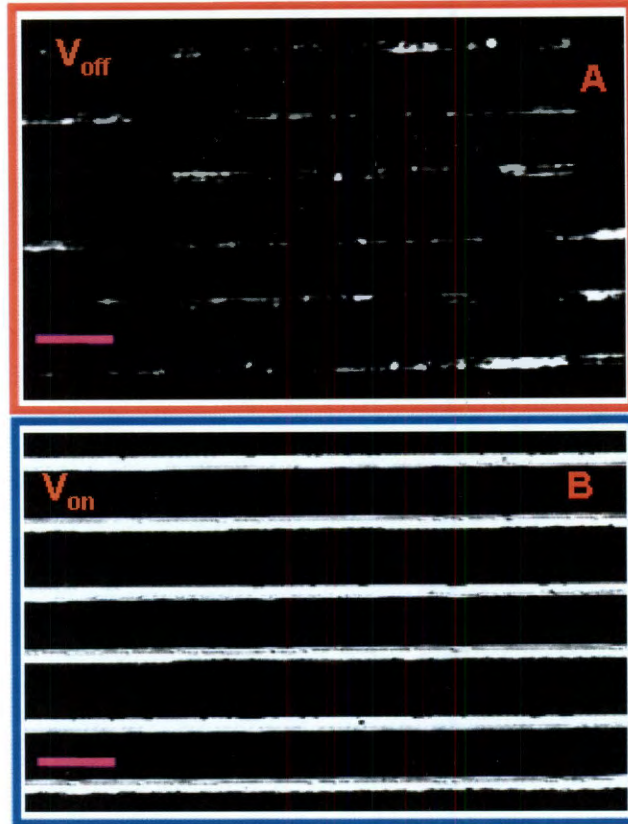


**Figure 3.3:** (A) Transmitted light microscope image of a liquid crystal cell in between two crossed polarizers. The sample is mounted in such a way that the nematic director of the liquid crystal is parallel to one of the polarizer axes. (B) Same as (A) while applying an AC electric field of 6 V and 1 kHz. The gaps between the electrodes now appear brighter because of the electric field induced reorientation of the liquid crystal director causing a change of the transmitted light polarization allowing more light to pass through the second polarizer. The liquid crystal molecules between the electrodes are switched in-plane from parallel (voltage off) to perpendicular (voltage on) with respect to the electrode array while the liquid crystal molecules close to the glass coverslip retain their initial orientation due to strong anchoring by the polyimide alignment layer. This results in the formation of a twisted nematic phase in which the director changes direction by  $90^\circ$  from one side of the cell to the other. The change in contrast in these transmitted light microscope images is consistent with this phase transition of the liquid crystal in response to the applied electric field and hence demonstrates the successful operation of this liquid crystal cell.

**3.3.4 Liquid crystal cell thickness measurement:** The cell thickness  $d$  was determined from extinction spectra according to:

$$d = \frac{1}{2 \times \left( \frac{1}{\lambda_1} - \frac{1}{\lambda_2} \right)}$$

where  $\lambda_1$  and  $\lambda_2$  are two consecutive maxima in the extinction spectrum. To validate this analysis, cells with a known gap were measured in parallel.

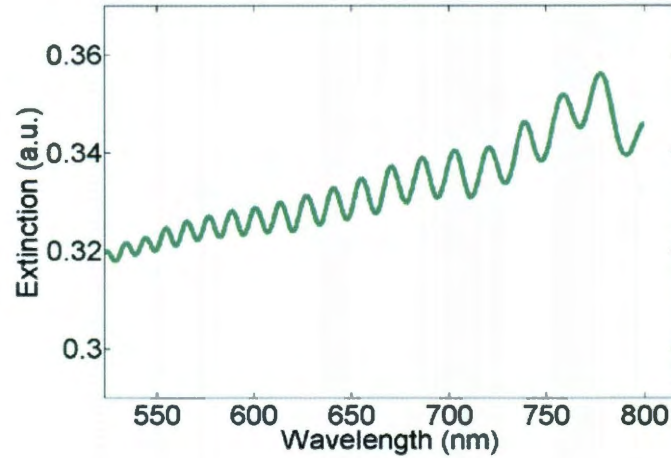


**Figure 3.4:** Extinction spectrum of an empty cell. From the interference fringes due to multiple reflections at the glass interfaces a cell gap of  $14.2 \pm 0.5 \mu\text{m}$  is obtained.

**3.3.5 Single particle measurements:** All single particle scattering measurements were performed with a home built dark-field microscope (Zeiss, Observer.D1m) working in transmission geometry (Figure 3.5). A halogen lamp was used as the light source. The unpolarized light from the lamp was focused by a dark-field condenser (Zeiss, numerical aperture (NA) = 1.40) and transmitted scattered light was collected by a 63X oil immersion objective (Zeiss, NA = 0.7) and guided to either an avalanche photodiode detector (Perkin Elmer) or a CCD camera (Horiba Jobin Yvon). The scattering images were taken by scanning the sample with a XY piezo scanning stage (Physik Instrumente) across a  $50 \mu\text{m}$  pinhole located at the first image plane of the microscope. A LabView interface was designed to synchronize the stage movement and the data acquisition. A

typical image was  $5\ \mu\text{m} \times 5\ \mu\text{m}$  in dimensions consisting of  $128 \times 128$  pixels with a 500 ms line time. Single particle spectra were collected by guiding the light towards a liquid nitrogen cooled CCD camera attached to a spectrograph (Triax 190). A polarizer was inserted in front of both detectors. All measured single particle images and spectra were corrected for the background scattering of the liquid crystal solvent. All data analysis was carried out using Matlab.

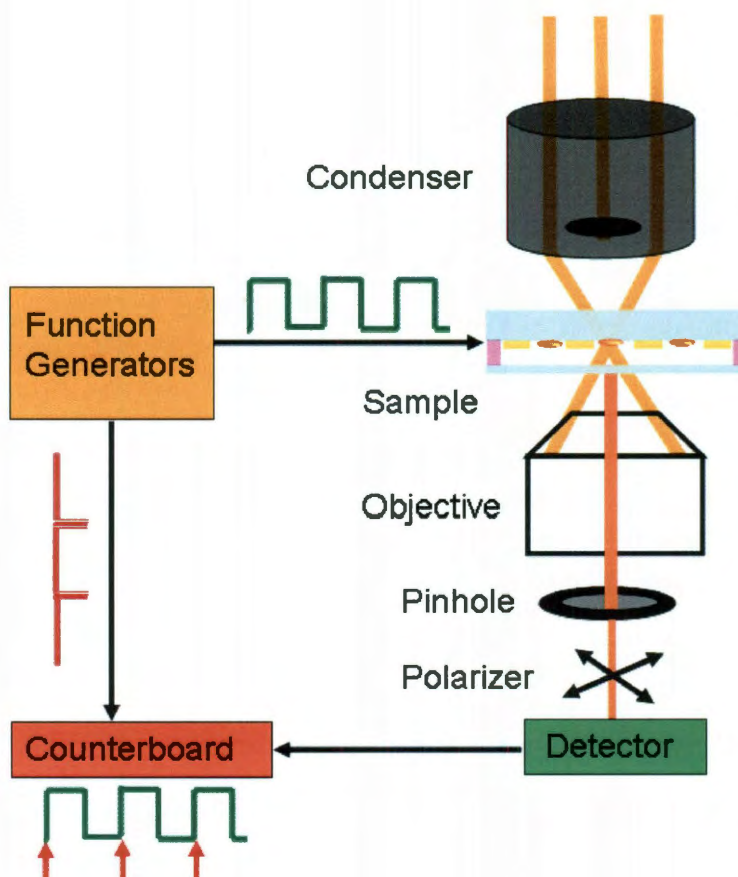
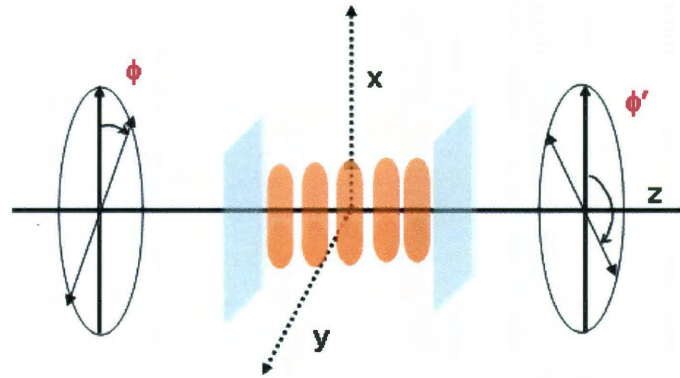


**Figure 3.5:** Transmitted light dark-field microscope setup. The sample is excited with unpolarized light from a lamp. The polarized plasmon scattering passes through the liquid crystal and is collected by an objective. After going through a pinhole to spatially select individual nanorods and a polarizer, the scattered light is detected either by an avalanche photodiode detector or a CCD camera. The signal from the avalanche photodiode detector is fed into a counterboard (Becker&Hickl), which is synchronized to the signal applied to the liquid crystal cell using a set of three function generators. One of the function generators supplies the voltage

modulation for the sample (square wave with 4 – 8 V and 1 Hz). To accurately determine the beginning and end of the square pulses, marker pulses are sent from a second function generator to another channel of the counterboard. These two function generators are synchronized by a master function generator<sup>112</sup>.

### 3.5.6 Analytical solution for the polarization change of light passing through homogeneous and twisted nematic liquid crystal phases:

#### A. Homogeneous nematic liquid crystal phase



**Scheme 3.1:** Change of polarization of the incident light when passing through a homogeneous liquid crystal device. The nematic director is oriented along x. The input ( $\phi$ ) and output ( $\phi'$ ) polarization angle are defined with respect to the nematic director.

The director of the liquid crystal is assumed to be along the x-axis. The input and output polarization directions are  $\phi$  and  $\phi'$  defined with respect to the x-axis, respectively. For a homogenous nematic liquid crystal, the Jones matrix describing the change in polarization of an incident electromagnetic wave is given by<sup>113</sup>:

$$M_{HNLCD} = \begin{pmatrix} 1 & 0 \\ 0 & e^{-i\chi} \end{pmatrix} \quad (1)$$

where  $\chi = \frac{2\pi d \Delta n}{\lambda}$ . With a measured cell thickness  $d = 14 \mu\text{m}$ , a difference in extraordinary and ordinary refractive indices  $\Delta n = 0.2$ , and a wavelength  $\lambda = 800 \text{ nm}$  equation (1) yields:

$$M_{HNLCD} = \begin{pmatrix} 1 & 0 \\ 0 & -1 \end{pmatrix} \quad (2)$$

The Jones vector describing the polarization of the incident light wave is:

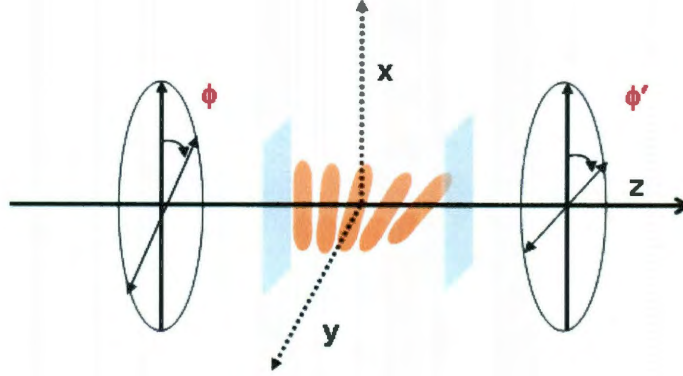
$$\begin{bmatrix} E_x \\ E_y \end{bmatrix} = \begin{bmatrix} \cos \phi \\ -\sin \phi \end{bmatrix} \quad (3)$$

After passing through the homogeneous liquid crystal cell one obtains:

$$\begin{aligned} \begin{bmatrix} E'_x \\ E'_y \end{bmatrix} &= \begin{bmatrix} \cos \phi' \\ -\sin \phi' \end{bmatrix} \\ &= M_{HNLCD} \begin{bmatrix} E_x \\ E_y \end{bmatrix} = \begin{pmatrix} 1 & 0 \\ 0 & -1 \end{pmatrix} \begin{bmatrix} \cos \phi \\ -\sin \phi \end{bmatrix} = \begin{bmatrix} \cos \phi \\ \sin \phi \end{bmatrix} \end{aligned} \quad (4)$$

According to equation (4) the output polarization  $\phi'$  becomes  $-\phi$  or  $180^\circ - \phi$ .

## B. Twisted nematic liquid crystal phase



**Scheme 3.2:** Change of polarization of the incident light when passing through a twisted nematic liquid crystal device. The initial and final orientation of the nematic director is along x and y respectively. The input ( $\phi$ ) and output ( $\phi'$ ) polarization angle are defined with respect to the initial nematic director orientation (along x).

The director of the twisted nematic liquid crystal cell rotates from the x- to the y-axis across the sample thickness (z-axis). The input and output polarization directions are  $\phi$  and  $\phi'$  defined with respect to the x-axis, respectively. For a twisted nematic liquid crystal, the Jones matrix describing the change in polarization of an incident electromagnetic wave is given by equation (3):

$$M_{TNLCD} = \exp(-i\beta) \begin{pmatrix} \cos \alpha & -\sin \alpha \\ \sin \alpha & \cos \alpha \end{pmatrix} \begin{pmatrix} \cos \gamma - \frac{i\beta \sin \gamma}{\gamma} & \frac{\alpha \sin \gamma}{\gamma} \\ -\frac{\alpha \sin \gamma}{\gamma} & \cos \gamma + \frac{i\beta \sin \gamma}{\gamma} \end{pmatrix} \quad (5)$$

where  $\alpha = \frac{\pi}{2}$ ,  $\beta = \pi d \Delta n / \lambda$ , and  $\gamma = \sqrt{\alpha^2 + \beta^2}$ . With a measured cell thickness  $d = 14 \mu\text{m}$ , a difference in extraordinary and ordinary refractive indices  $\Delta n = 0.2$ , and a wavelength  $\lambda = 800 \text{ nm}$  equation (5) yields:

$$M_{TNLCD} = \begin{pmatrix} -0.14i & -0.98 - 0.11i \\ -0.98 + 0.11i & -0.14i \end{pmatrix} \quad (6)$$

The Jones vector describing the light polarization after the twisted liquid crystal cell is given by:

$$\begin{aligned} \begin{bmatrix} E'_x \\ E'_y \end{bmatrix} &= \begin{bmatrix} \cos \phi' \\ -\sin \phi' \end{bmatrix} \\ &= M_{TNLCD} \begin{bmatrix} E_x \\ E_y \end{bmatrix} \\ &= \begin{pmatrix} -0.14i & -0.98 - 0.11i \\ -0.98 + 0.11i & -0.14i \end{pmatrix} \begin{bmatrix} \cos \phi \\ -\sin \phi \end{bmatrix} \\ &= \begin{bmatrix} 0.98 \sin \phi - i(0.14 \cos \phi - 0.11 \sin \phi) \\ -0.98 \cos \phi + i(0.11 \cos \phi + 0.14 \sin \phi) \end{bmatrix} \end{aligned} \quad (7)$$

Considering only the real part, equation (7) can be approximated giving:

$$\begin{bmatrix} E'_x \\ E'_y \end{bmatrix} \cong \begin{bmatrix} 0.98 \sin \phi \\ -0.98 \cos \phi \end{bmatrix} \cong \begin{bmatrix} \sin \phi \\ -\cos \phi \end{bmatrix} \quad (8)$$

According to equation (8) the output polarization  $\phi'$  becomes  $90^\circ - \phi$ .

### 3.4 Results and discussion

A critical step in our method is to employ a planar electrode geometry that allows for in-plane switching of the liquid crystal director. Photolithography is used to fabricate interdigitated electrode arrays with a gap of 10  $\mu\text{m}$ . The height of the gold electrodes is 60 nm. Figure 3.1 and Figure 3.6 show a photograph (Figure 3.1), scheme (Figure 3.6A), and reflected light microscope image (Figure 3.6B) of the electrode array. Individual gold nanorods with average dimensions of (28 x 76) nm or (35 x 60) nm are isolated in between the electrodes (Figure 3.2). The nanorods are then covered with the liquid crystal 5CB after constructing cells consisting of a microscope glass slide and a coverslip: the glass slide serves as the substrate for the interdigitated electrode array while the coverslip is coated with a polyimide alignment layer, which ensures the alignment of the liquid crystal director parallel to the electrodes without an applied voltage<sup>114</sup>. For each sample, polarized light microscopy is used to verify the formation of a homogeneous nematic liquid crystal phase and to determine the threshold voltage for the electric field induced reorientation of the liquid crystal director (Figure 3.3).

Using dark-field imaging, we observe reversible and up to 100 % intensity modulation of the polarized light scattered by the longitudinal surface plasmon resonance of randomly orientated single gold nanorods. Figure 3.6C illustrates the orientation of the sample with respect to the incident and detected light (see also (Figure 3.5)). The images in Figure 3.6D and 3.6E are recorded without an applied electric field and for scattered light polarizations parallel (3.6D) and perpendicular (3.6E) to the electrodes. A dark-field transmitted light geometry with unpolarized excitation is used to record the spectrally



integrated scattering intensity after passing a polarizer in the detection path of a home-built single particle microscope. SEM confirms that the signal originated from mainly single nanorods (Figure 3.2). Because the longitudinal plasmon mode, polarized parallel to the long nanorod axis dominates the scattering spectrum,<sup>115</sup> the relative scattering

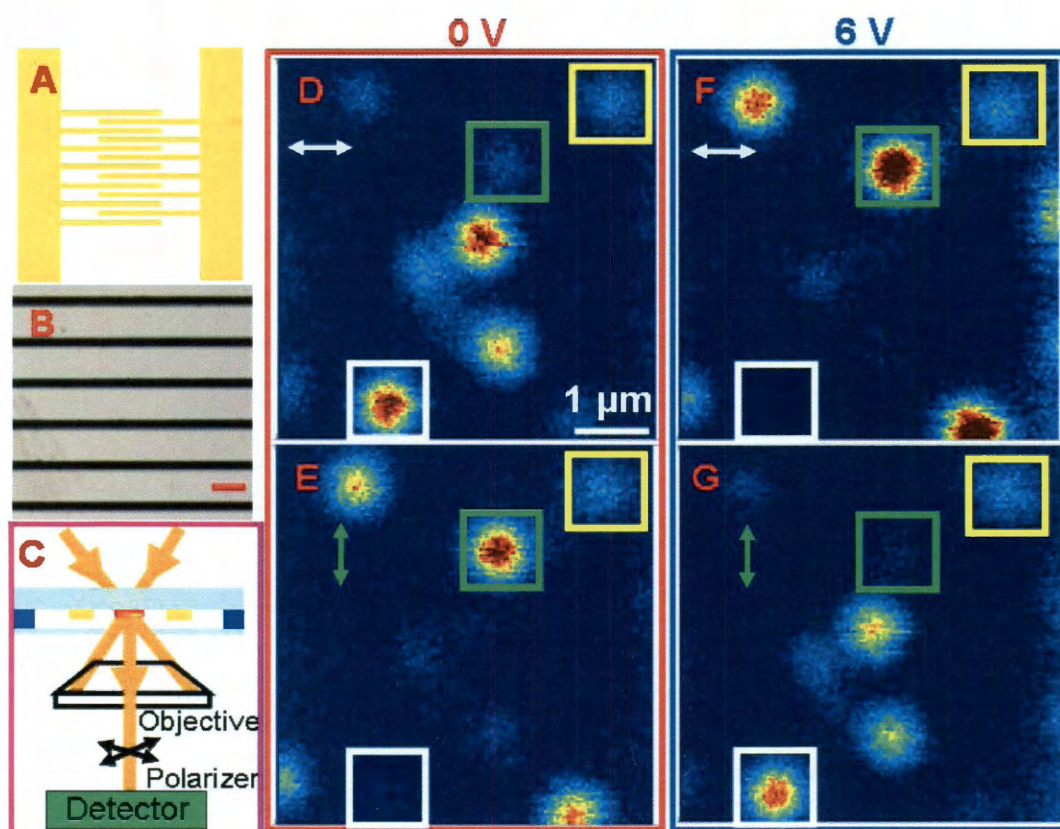


**Figure 3.6.** (A, B) Geometry of the interdigitated electrode array as illustrated by a schematic drawing (A) and a reflected light microscope image (B) of an array fabricated on glass using photolithography. The bright areas in (B) are the electrodes (scale bar corresponds to 50  $\mu\text{m}$ ). The nematic director of the liquid crystal 5CB is orientated parallel to the electrodes without an applied electric field. (C) Scheme of the experimental setup showing the direction of light propagation and sample geometry. (D, E) Polarized dark-field scattering images of single gold nanorods located in the electrode gaps and covered with 5CB. The detected light polarizations are chosen to be parallel (white) and perpendicular (green) to the electrode array as indicated by the arrows. (F, G) Same as (D, E) recorded with an applied electric field (6V, 1 kHz).

intensity in the two orthogonally polarized images is a measure of the nanorods' apparent orientations. Therefore, the nanorods marked with the white and green boxes in Figure 3.6D and 3.6E appear mainly orientated parallel and perpendicular to the electrodes,

respectively. When an electric field is applied, the scattering intensities of these nanorods are reversed in the two corresponding images (Figures 3.6F and 3.6G), indicating an orthogonal rotation of the polarized plasmon scattering.

The intensity of the plasmon scattering spectrum can be completely turned on and off as demonstrated by single particle dark-field scattering spectroscopy. Figures 3.6A and 3.6B show dark-field scattering spectra for two different gold nanorods recorded with and without an applied electric field. The polarized spectra are taken by directing the scattered light to a CCD camera attached to a spectrograph and setting the polarizer axis parallel to the electrode array. This intensity modulation of the scattering spectrum of individual gold nanorods is different in comparison to previously observed spectral shifts using liquid crystals.<sup>29-32,109</sup>

Orthogonal rotation of the polarized scattering occurs for all nanorods, independent of their apparent orientations. The scattering intensity of the nanorod marked by the yellow box in Figure 3.6 does not show a significant change when the electric field is applied. However, the almost equal scattering intensities in the orthogonally polarized images imply that this nanorod has an apparent orientation of approximately 45° with respect to the electrode array. A 90° rotation of the scattered light polarization therefore has no effect on the collected signal. As shown in the insets of Figures 3.7A-3.7C, this conclusion is confirmed by recording the scattering intensity as a function of polarizer angle  $\theta$ , which yields a  $\cos^2(\theta - \phi)$  dependence where the phase

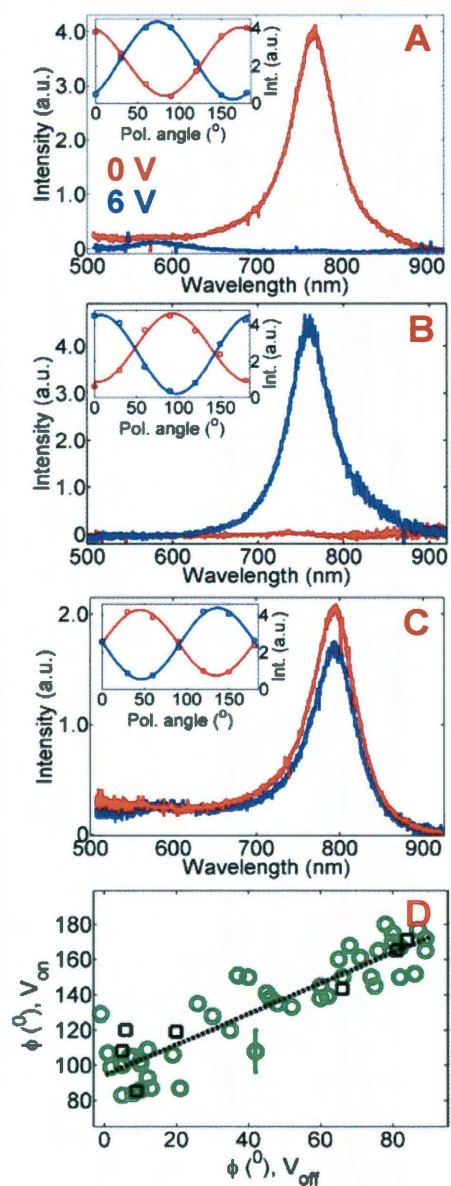


**Figure 3.7.** (A, B, C) Polarized dark-field scattering spectra of individual gold nanorods with (blue) and without (red) an electric field (6 V, 1 kHz). The polarizer is set parallel to the electrodes, causing the nanorods in (A) and (B) to appear bright and dim at 0 V, respectively. At 6 V the behavior is reversed as the direction of the scattered light polarization  $\phi$  is rotated by  $90^\circ$ . This is further evident from the insets showing the scattering intensity as a function of polarizer angle. For the nanorod in (C), the change in  $\phi$  is also  $90^\circ$ . However, because the initial polarization for 0 V is not aligned with the polarizer, a reduced intensity modulation of the scattering spectra is observed. (D) Orthogonal polarization rotation of the plasmon scattering measured for a total of 59 nanorods from two samples with the surface plasmon maximum varying between 680 and 850 nm. The error in determining the polarization is  $\sim 10^\circ$  mainly due to the limited number of polarization angles sampled. The black line is a linear fit with a slope of 0.9, where deviations from ideal behavior are likely due to local imperfections in the liquid crystal alignment and thickness.

$\phi$  indicates the polarization direction of the light received at the detector. As expected based on the spectra for the nanorods in Figures 3.7A and 3.7B,  $\phi$  changes by  $\sim 90^\circ$ , from  $174 \pm 8^\circ$  to  $75 \pm 7^\circ$  (3.7A) and  $95 \pm 9^\circ$  to  $9 \pm 6^\circ$  (3.7B). Although the intensity of the scattering spectra for the nanorod in Figure 3.7C varies little for the polarizer angle set parallel to the electrode array, the direction of the scattered light polarization is still rotated by  $\sim 90^\circ$ , from  $46 \pm 8^\circ$  to  $138 \pm 9^\circ$ . These results suggest that depending on the

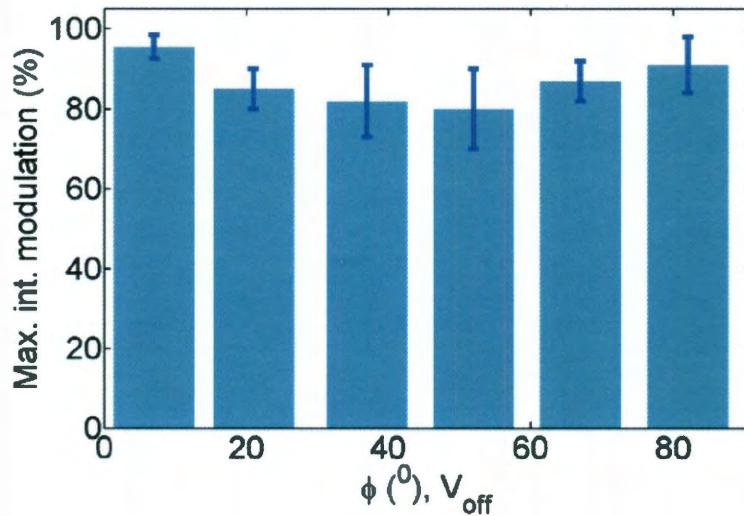


**Figure 3.8:** Maximum intensity modulation achieved from individual nanorods as a function of their apparent orientation in the homogeneous liquid crystal phase. The intensity modulation is calculated by placing the polarizer along the apparent orientation of the nanorods in the voltage off state, which is achieved by maximizing the scattering intensity by varying the polarizer angle. The modulation depth is then obtained as  $(I(V_{off}) - I(V_{on})) / I(V_{off})$ . These results demonstrate highly efficient plasmon modulation for all nanorods independent of their orientation.

relative orientation of the nanorod and the polarizer angle a variable intensity modulation of the longitudinal surface plasmon resonance can be achieved. Conversely, when the polarizer is placed parallel or perpendicular to the scattered light polarization in the voltage off state nearly 100% intensity modulation is seen for all nanorods (Figure 3.8).

This orthogonal rotation of the polarization for plasmon scattering from individual nanorods is highly reproducible. Figure 3.7D summarizes the results for 9 different samples by plotting the polarization direction  $\phi$  with an applied electric field ( $V_{\text{on}}$ ) vs.  $\phi$  measured with a voltage of 0 V ( $V_{\text{off}}$ ). A polarization change of  $60^\circ$  to  $90^\circ$  is found for over 85 % out of a total of 59 nanorods with resonance wavelengths varying between 680

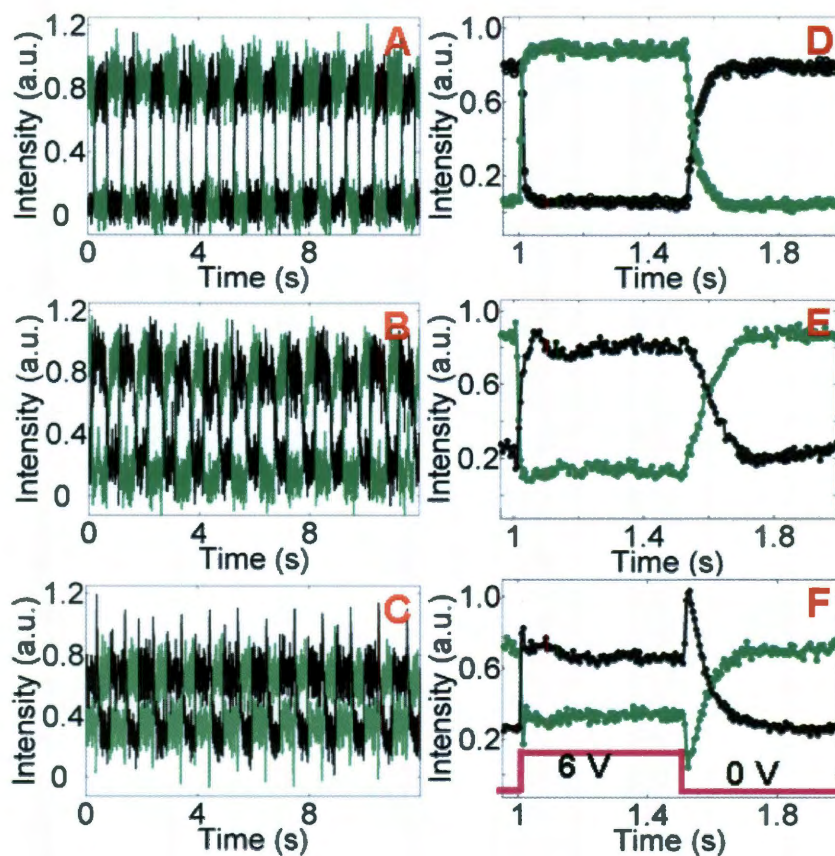


**Figure 3.9.** (A, B, C) Reversible polarization rotation at a 1 Hz modulation frequency recorded using a 6 V square waveform and a 5 ms bin time. Time transients of the integrated scattering intensity are recorded using single photon counting detectors with two orthogonal polarizations (black: parallel; green: perpendicular with respect to the electrode array) for nanorods having apparent initial orientations and surface plasmon resonance maxima of  $10^\circ$  and 725 nm (D),  $80^\circ$  and 761 nm (E), and  $60^\circ$  and 809 nm (F). (D, E, F) Same as (A, B, C) but averaged for one cycle of the applied square waveform, yielding response times of  $20 \pm 10$  ms and  $170 \pm 40$  ms for on and off switching, respectively. The intensities in each channel are corrected for background scattering and then normalized by dividing by the total intensity, i.e. sum of both channels.

and 850 nm. Nanorods from two samples with different aspect ratios are included (Figure 3.2). Deviations from a perfect orthogonal polarization rotation are attributed to imperfection in the local liquid crystal alignment and thickness.

The response time for modulating the plasmon scattering intensity is determined by the intrinsic relaxation dynamics of 5CB. To show this, we synchronize the photon counting acquisition for two orthogonally polarized detection channels with the electric field modulation (Figure 3.5).<sup>112</sup> Figures 3.9A-3.9C show integrated scattering intensity vs. time traces for three gold nanorods. The intensities of the two channels are 90° out of phase, where the green and black curves correspond to detected polarizations parallel and perpendicular to the electrodes, respectively. The modulation depth is decreased to 31 % for the nanorod in Figure 3.9C as the scattered light polarization in this case is neither parallel (as in 3.9A) nor perpendicular (as in 3.9B) to the electrodes and hence polarizer when no field is applied. Because of the stable modulation phase and the external synchronization, averaging these time transients gives one-cycle response curves (Figures 3.9D-3.9F), from which time constants of  $20 \pm 10$  ms and  $170 \pm 40$  ms can be determined for switching the voltage on and off, respectively. These timescales are consistent with the dielectric response of 5CB,<sup>116</sup> as also verified by analyzing the intensity modulation of the background scattering from the liquid crystal solvent (Figure 3.10).

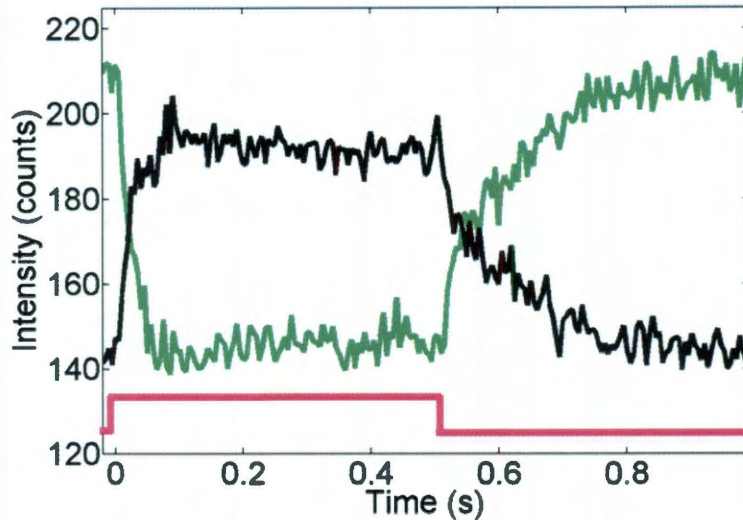


**Figure 3.10:** Background scattering from the liquid crystal solvent 5CB recorded at a 1 Hz modulation frequency using a 6 V square waveform and a 5 ms counterboard bin time. The black and green lines show the intensities for polarization parallel and perpendicular with respect to the electrode array. The fast rise ( $25 \pm 10$  ms) and slow relaxation ( $200 \pm 50$  ms) times of the liquid crystal are calculated by fitting the intensities with an exponential function. These response times are in good agreement with the corresponding values measured for the intensity modulation of the polarized scattering from the individual nanorods.

The intensity modulation of the polarized scattering from individual gold nanorods is due to the electric field induced response of the liquid crystal as no changes are observed for cells filled with either air (Figure 3.11) or water (Figure 3.12), even at higher voltages. For the mechanism of the observed orthogonal polarization rotation we therefore need to consider the following possibilities: (1) a mechanical rotation of the nanorods by  $90^\circ$  due to strong surface anchoring forces by the liquid crystal molecules<sup>117,118</sup> or (2) an optical effect caused by a change in the birefringence due to the reorientation of the liquid crystal molecules in response to an applied electric field. The first explanation can be ruled out because no change in scattering intensity is seen when the same liquid crystal cell is studied in a reversed geometry, in which the polarized

scattering from the gold nanorods does not pass through the liquid crystal medium before being detected (Figure 3.13).

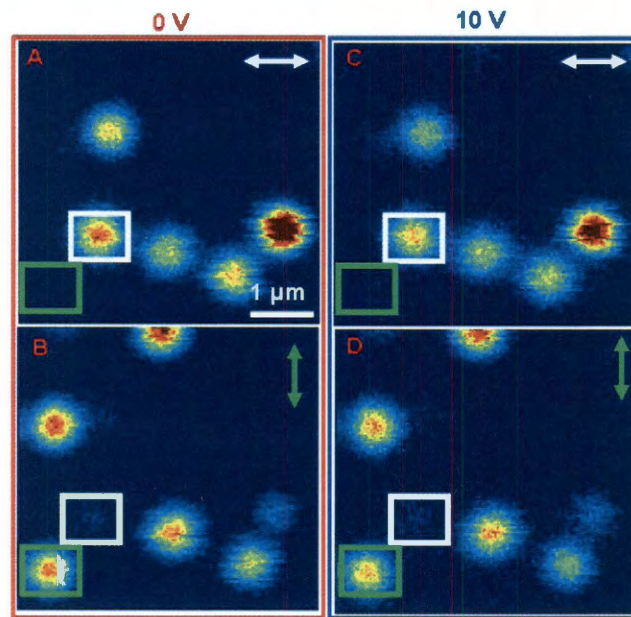


**Figure 3.11:** Effect of the electric field on the polarization direction of the light scattered by single gold nanorods in air. This cell is prepared in the same way as the liquid crystal samples except that no liquid crystal is injected into the cell. (A, B) represent polarized images of single gold nanorods without an electric field. (C, D) represent polarized scattering images with an applied electric field of 10 V. No change in the scattered light polarization and no physical rotation of the nanorods are observed.



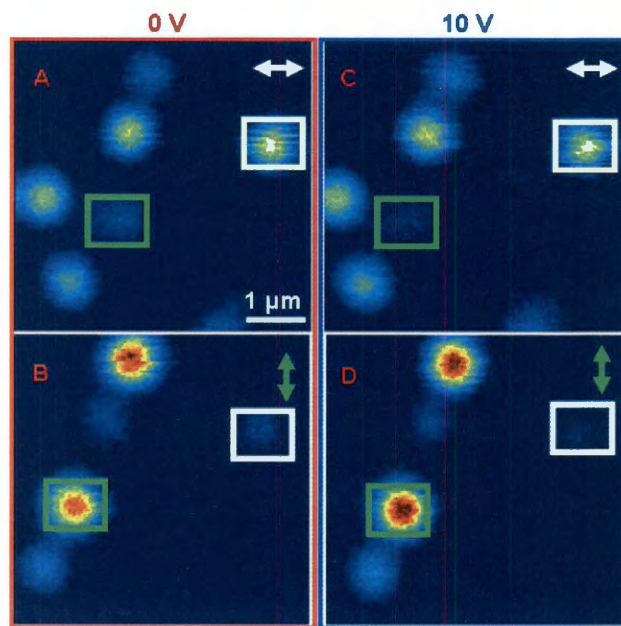


**Figure 3.12:** Effect of the electric field on the polarization direction of the light scattered by single gold nanorods in water. This cell is prepared in the same way as the liquid crystal samples except that water is injected into the cell instead of the liquid crystal solvent. (A, B) represent polarized images of single gold nanorods without an electric field. (C, D) represent polarized scattering images with an applied electric field of 10 V. No change in the scattered light polarization and no physical rotation of the nanorods are observed.

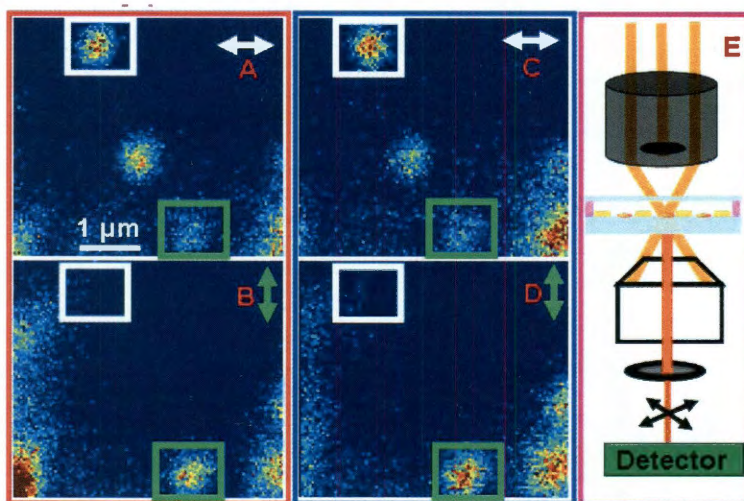


**Figure 3.13:** Effect of the electric field on the polarization direction of the light scattered by single gold nanorods in 5CB when the cell is placed upside down. (A, B) represent polarized images of single gold nanorods without an electric field. (C, D) represent polarized scattering images with an applied electric field of 6 V. The experimental geometry is given in (E). No change in the scattered light polarization is observed. The reduced contrast in the dark-field scattering images compared to Figure 3.6 is because of the use of a lower NA objective (Zeiss LD Achromplan, 40X, 0.60 NA) that can image through the thicker glass slide.

The second mechanism can be tested by comparing the polarization direction of the scattered light with and without an applied field to the actual nanorod orientation. In our experimental geometry (Figure 3.6C), the polarized scattering from the single gold nanorods passes through the liquid crystal before reaching the detectors. Because of the birefringence of the liquid crystal, the polarization of the scattered light is rotated before reaching the detector. The ‘apparent’ nanorod orientation, which is calculated from the dependence of the scattering intensity on the polarizer angle (see insets in Figure 3.7A-3.7C) does therefore not necessarily correspond to the ‘actual’ nanorod orientation. Correlated SEM imaging of the same gold nanorods to determine their actual orientation is not possible as exposure to the electron beam damages the surface and prevents the formation of the liquid crystalline phase. However, because the birefringence is lost in the isotropic phase of the liquid crystal (Figure 3.14) no change in polarization can occur.

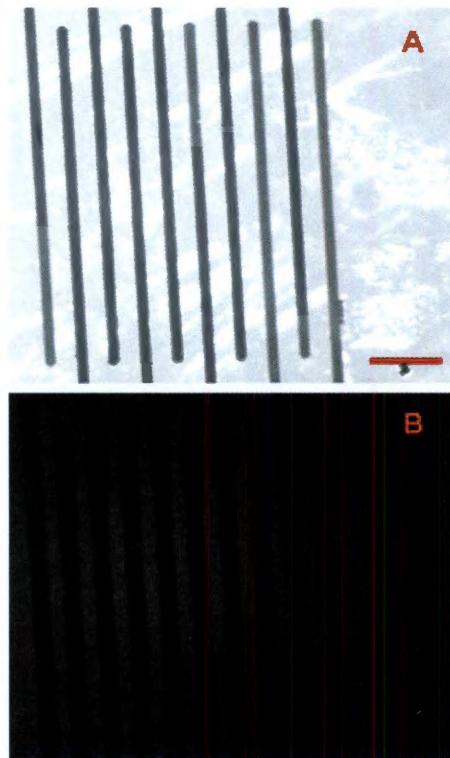


**Figure 3.14:** Nematic to isotropic phase transition of the liquid crystal 5CB. The images are

taken with an optical microscope employing a bright-field transmitted light geometry. The liquid crystal director of the sample is aligned at  $45^\circ$  with respect to two crossed polarizers. In the nematic phase, the liquid crystal acts as a birefringent material rotating the polarization of the incident light and hence giving a bright contrast in (A). When the liquid crystal is heated above the nematic to isotropic phase transition, the liquid crystal is no longer birefringent and most of the light is blocked by the second polarizer resulting in the dark image shown in (B). The nematic to isotropic phase transition is induced by resistive heating of the liquid crystal cell with an AC electric field of 5 V and 1 kHz, which is accomplished by using an indium tin oxide coated coverslip to construct the liquid crystal cell. The length of the scale bar is 100  $\mu\text{m}$ .

The actual nanorod orientations can hence be obtained by optical means when melting the liquid crystal to its isotropic phase. This approach is illustrated in Figures 3.15A-C, which show polarized dark-field scattering images of two single gold nanorods without (3.15A,  $V_{\text{off}}$ ) and with (3.15B,  $V_{\text{on}}$ ) an applied electric field and after resistive heating of the liquid crystal to the isotropic phase (3.15C). This is done for a particular sample that is prepared with an indium tin oxide coated coverslip to which a 5 V AC (1 kHz frequency) voltage is applied to heat the liquid crystal. It is evident from these images that the polarization of the plasmon scattering is altered by the nematic liquid crystal phase, which can be quantified by recording the scattering intensity as a function of polarizer angle  $\theta$  for particles P1 and P2 (Figures 3.15D and 3.15E). Fitting the data to  $\cos^2(\theta - \phi)$  again yields  $\phi$ , which for the isotropic phase gives the actual nanorod orientation (P1:  $55^\circ$  and P2:  $175^\circ$ ).

While the  $90^\circ$  polarization rotation between  $V_{\text{on}}$  and  $V_{\text{off}}$  is easily seen in Figures 3.15D and 3.15E, the relationship between the actual nanorod orientation and the directions of the scattered light polarization in the nematic phase with and without an applied field is much less obvious from only these two particles. Figures 3.15F ( $V_{\text{off}}$ ) and 3.15G ( $V_{\text{on}}$ ) therefore display the dependence of the detected light polarization on

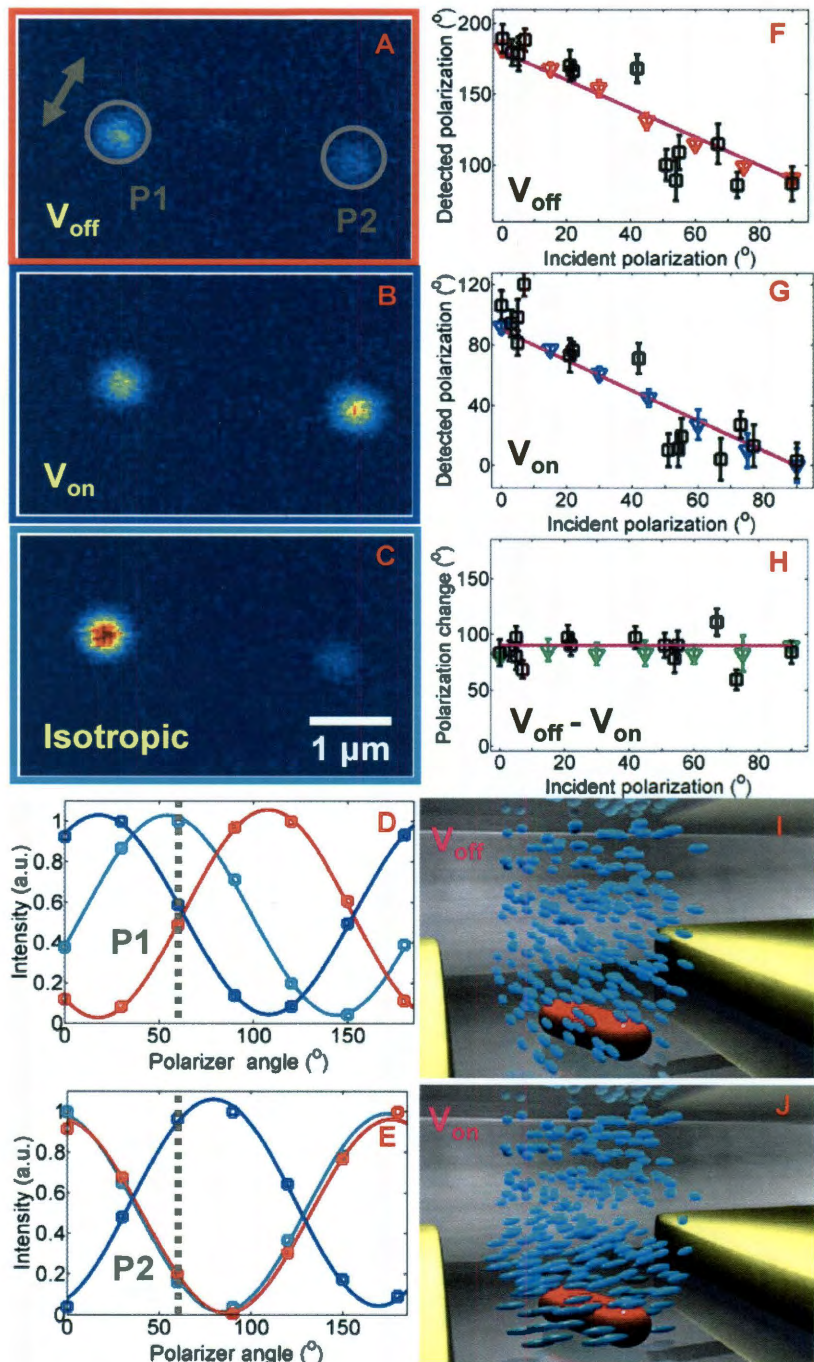


**Figure 3.15.** (A ,B, C) Polarized dark-field scattering images recorded without (A) and with (B) an electric field, and after melting the liquid crystal to its isotropic phase (C). The direction of the scattered light polarization is determined from measurements of the intensity vs. polarizer angle for particle 1 (D) and 2 (E) and for  $V_{off}$  (red),  $V_{on}$  (blue), and the isotropic phase (cyan). The vertical lines in (D, E) and the arrow in (A) indicate the polarizer angle used for recording the images. (F, G) Dependence of the detected light polarization on the actual nanorod orientation for  $V_{off}$  (F) and  $V_{on}$  (G) (black symbols). The nanorod orientation corresponds to the polarization

direction in the isotropic phase, i.e. the incident polarization. The polarization varies as  $180^\circ - \phi$  for  $V_{\text{off}}$  (F) and  $90^\circ - \phi$  for  $V_{\text{on}}$  (G), resulting in an overall orthogonal polarization rotation independent of the nanorod orientation  $\phi$  (H). This orthogonal polarization rotation is due to an electric field induced transition from a homogeneous to a twisted nematic phase (I, J), which is confirmed by calculations (F-H, solid lines) and transmission measurements using linearly polarized light at  $800 \pm 20$  nm from a lamp (F-H, colored symbols).

the actual nanorod orientation as determined in the isotropic phase for a total of 15 nanorods measured for this sample (black squares). Considering that in the dark-field illumination geometry the nanorods basically act as individual light sources, the nanorod orientation corresponds to the incident light polarization. This is further supported by measuring the change in polarization for 800 nm light from a lamp, which is transmitted through a liquid crystal sample without and with an applied voltage (colored symbols). The data suggest that the incident polarization direction  $\phi$  is rotated by  $180^\circ - \phi$  for  $V_{\text{off}}$  (3.15F) and  $90^\circ - \phi$  for  $V_{\text{on}}$  (3.15G) while passing through the liquid crystal. The difference between  $V_{\text{off}}$  and  $V_{\text{on}}$  is therefore a  $90^\circ$  change of the polarization direction, independent of the incident polarization and hence the actual orientation of the nanorods (Figure 3.15H).

The results in Figure 3.15 can be explained by an electric field induced transition from a homogenous to a twisted nematic liquid crystal phase, schematically illustrated in Figures 3.15I and 3.15J. The electrodes are much thinner compared to the thickness of the cell, and therefore only the liquid crystal molecules between the electrodes and close to the surface are rotated by  $90^\circ$  when an electric field is applied, effectively creating a twisted nematic phase. To verify this suggested mechanism and explain the data in Figure 3.15, we model the polarization rotation of light passing through the homogeneous and twisted nematic liquid crystal phases using Jones matrices as shown in the materials and

methods section (3.5.6). Assuming an incident wavelength of 800 nm, the calculations show that the polarization of incident light is indeed rotated by  $180^\circ - \phi$  and  $90^\circ - \phi$  in the homogeneous and twisted nematic phases if the sample thickness is 6  $\mu\text{m}$ , 10  $\mu\text{m}$ , 14  $\mu\text{m}$ , 18  $\mu\text{m}$ , etc. Measuring the thickness of an empty sample cell by spectral interference confirms a value of 14  $\mu\text{m}$  (Figure 3.4). The solid lines in Figures 3.15F-3.15H, showing excellent agreement with the experiments, are obtained using this model with a thickness of 14  $\mu\text{m}$ , light of 800 nm wavelength, and the refractive indices of 5CB.

It should be pointed out that the transition from a homogenous to a twisted nematic liquid crystal phase, as suggested for the mechanism, differs significantly from the working principle of typical twisted nematic liquid crystal display devices. The latter operate by switching between a twisted nematic phase (voltage off) and a homeotropic alignment (voltage on) with an electric field applied in the direction of the light passing through the cell.<sup>119</sup> In contrast, in our devices an electric field is applied in the sample plane (perpendicular to the light direction) and induces a homogeneous to twisted nematic transition.

To achieve the highest contrast in intensity modulation for all nanorods it is important that the scattered light from the polarized surface plasmon resonance remains linear while passing through the liquid crystal layer, independent of the nanorod orientation. The measured scattering intensities as a function of polarizer angle for the nanorods shown in the insets of Figures 3.7A-3.7C and in Figures 3.15D and 3.15E demonstrate that the modulation depth is close to 100% confirming the linear polarization of the detected light. Our results are further summarized in Figures 3.16A and 3.16B,

which show histograms of modulation depths as a function of apparent nanorod orientation with the voltage off and on, respectively. A small depolarization is noticeable

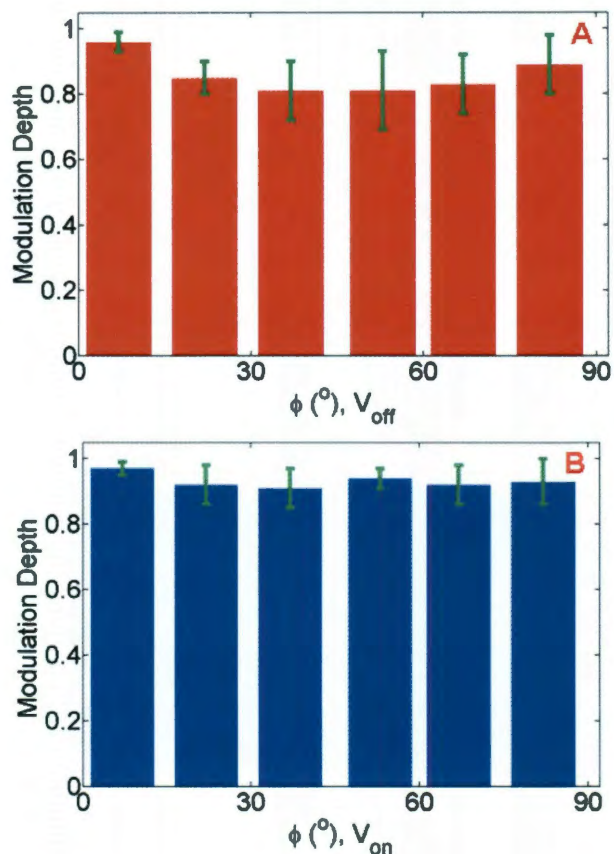


**Figure 3.16:** Modulation depths of single gold nanorods as a function of their apparent orientation without (A) and with (B) an applied electric field. The modulation depth  $M$  is calculated by fitting the measured scattering intensity vs. polarizer angle dependence for each individual gold nanorod with  $I(\theta) = N(1 + M \cos 2(\theta - \phi))$  where  $\theta$  is the polarizer angle and  $\phi$  is the apparent orientation of the nanorod.

for nanorods that are not aligned parallel or perpendicular to the electrodes. This behavior can be explained by variations of the liquid crystal thickness and differences in the surface plasmon resonance wavelength as illustrated in Figures 3.17A and 3.17B where these factors are modeled using Jones matrices. Interestingly, the effects of sample thickness and incident wavelength are less pronounced for the polarization rotation of

incident light by the liquid crystal in both the homogenous and twisted nematic phases (Figure 3.17C and 17D). Local imperfections in the liquid crystal alignment due to the nanorods acting as defect sites could further contribute to the spread in measured values for the change of polarization shown in Figure 3.7D. Sampling the polarization of the scattered light polarization from individual nanorods at only  $30^\circ$  intervals also causes a large error.

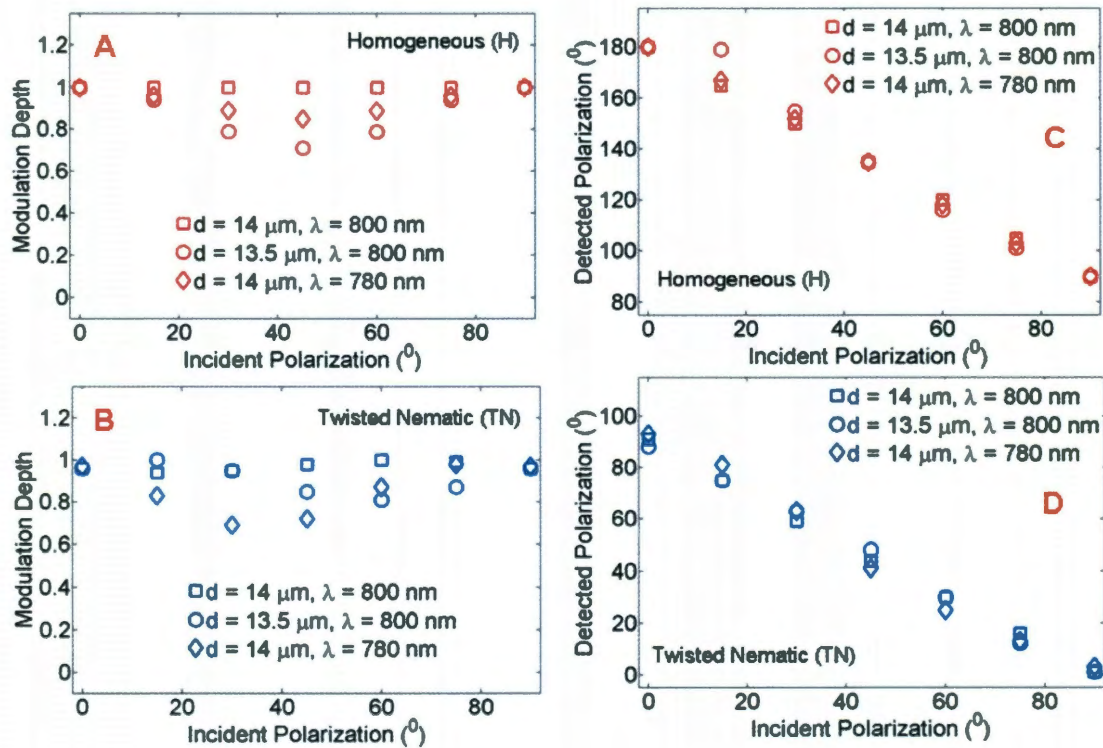


**Figure 3.17:** Calculated modulation depth and the polarization angle of the detected light is plotted against the incident polarization for homogeneous (A, C) and twisted nematic (B, D) liquid crystal phases of different thickness and incident light wavelength. The calculation was performed using Jones matrices for homogeneous and twisted nematic phases.



### **3.5 Conclusions**

In closing, we have described a novel approach to modulate the response of individual optical antennas by electrically switching between homogeneous and twisted nematic phases of a thermotropic liquid crystal. Even our non-optimized prototype devices show a surprisingly robust long-term stability enduring several thousand reversible switching cycles at 1 Hz for an hour without a change in scattering intensity, initial nanorod orientation, and nanorod position. We anticipate that the performance of our devices can be further improved in terms of operating voltage and response time by carefully selecting other liquid crystal solvents. While plasmonic nanorods represent the simplest form of an optical antenna, the described strategy should directly translate to more complex antenna architectures and other plasmonic elements for the electrical manipulation of visible light in structures with nanoscale dimensions.

### **3.6 Acknowledgements**

I thank Dr. Christy Landes and Dr. Naomi Halas for very fruitful suggestions throughout the course of this work and Mr. Britain Willingham for the art work. I also thank Mr. Ivan Knez for his help with the mask maker and mask aligner. This work was supported by the Welch Foundation (C-1664), the Office of Naval Research (N00014-10-1-0989), the ACS Petroleum Research Fund (50191-DNI6), and a 3M Nontenured Faculty Grant.

## CHAPTER 4

### MICROMETER-SCALE TRANSLATION AND MONITORING OF INDIVIDUAL NANOCARS ON GLASS <sup>1</sup>

#### 4.1 Abstract

Nanomachines designed to exhibit controlled mechanical motions on the molecular scale present new possibilities of building novel functional materials. Single molecule fluorescence imaging of dye-labeled nanocars on a glass surface at room temperature showed a coupled translational and rotational motion of these nanoscale machines with an activation energy of  $42 \pm 5$  kJ/mol. The 3 nm-long dye-labeled carborane-wheeled nanocars moved by as much as 2.5  $\mu\text{m}$  with an average speed of 4.1 nm/s. Translation of the nanocars due to a wheel-like rolling mechanism is proposed which is consistent with the absence of movement for a three-wheeled nanocar analog and the stationary behavior of unbound dye molecules. These findings are an important first step towards the rational design and ultimate control of surface-operational molecular machines.

---

<sup>1</sup> This chapter is based on the manuscript entitled “Micrometer-Scale Translation and Monitoring Individual Nanocars on Glass” by Saumyakanti Khatua, Jason M. Guerrero, Kavin Claytor, Guillaume Vives, Anatoly B. Kolomeisky, James M. Tour, and Stephan Link, published in ACS Nano **2009**, 2, 351-356.

## 4.2 Introduction

Science and engineering on the nanoscale offers novel possibilities for the design and synthesis of functional materials. In contrast to the engineering of macroscopic objects, where large pieces of materials are formed into smaller building blocks, nanoscale engineering is driven by a bottom-up materials synthesis. Inspiration for this approach can be drawn from nature, where self-assembly of smaller molecules into larger networks through often weak interactions play an important role. Nanomachines are promising new materials that are designed to exhibit controlled mechanical motions resembling macroscopic rotors<sup>42,120-122</sup>, elevators<sup>37</sup>, shuttles<sup>40,123,124</sup>, ratchets<sup>125</sup>, turnstiles<sup>44</sup>, scissors<sup>45</sup>, and muscles<sup>126</sup>. Performing electronic and mechanical operations with specifically designed molecules presents the ultimate limit of miniaturization and has a profound impact on many diverse fields ranging from molecular computing to medicine. Among the most important tasks for molecular machines is the directed transport of molecules and charges. To accomplish molecular directed motion and transport, molecular machines that resemble the chassis and wheels of a car, hence called nanocars, have been synthesized<sup>47,50,127</sup>. The rotation of the nanocar wheels is thought to induce a directional rolling of the nanocars on a surface<sup>50</sup>. Understanding the mechanisms by which these molecular machines work under different conditions is crucial for the future design of even more complex machines and essential for finding novel ways to control the forces that are responsible for their mechanical nanoscale motion.

Ensemble characterization techniques often fail to measure the detailed mechanical action of molecular machines as a random alignment of the individual molecules can lead to an orientational averaging, which is particularly problematic for the

two-dimensional motion of a nanocar on a flat surface. Thermally activated rolling of individual fullerene-wheeled nanocars has previously been studied by scanning tunneling microscopy (STM) on a gold surface<sup>50</sup>. While STM is extremely powerful in resolving atomic scale details of single molecules<sup>128</sup>, the substrate surface must be conductive. As a complementary single molecule technique fluorescence imaging<sup>54,129,130</sup> is capable of monitoring the motion of single molecules on non-conductive glass. Although the resolution of optical single molecule spectroscopy is limited by diffraction, localization of individual molecules below 100 nm down to a few nanometers has become possible for large photon count rates<sup>54,130</sup> while, at the same time, acquiring images that are tens of microns large.

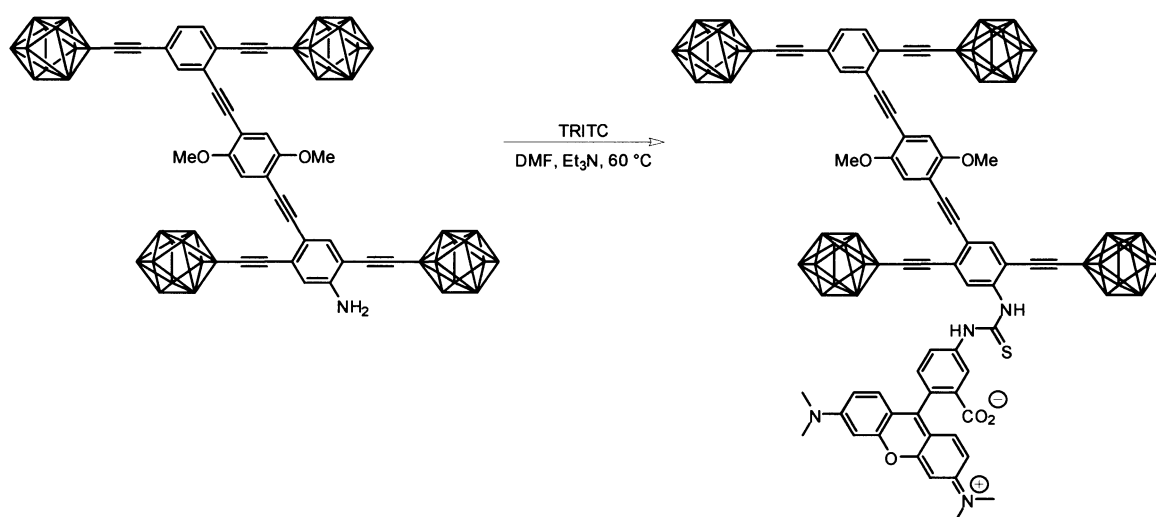
Here, we report on the translational motion of single dye-labeled carborane-wheeled nanocars on a glass surface, studied for the first time by single molecule fluorescence spectroscopy. Using polarization sensitive fluorescence detection in combination with a comparative analysis that employed three-wheeled nanocars and the dye tag only, we were able to investigate possible mechanisms for the movement of carborane-wheeled nanocars. Our results are consistent with a wheel-like rolling of the nanocars.

### **4.3 Materials and methods:**

#### **4.3.1 General synthetic methods**

All reactions were performed under an atmosphere of nitrogen unless stated otherwise. Dry dimethylformamide (DMF) was purchased from Sigma Aldrich and used as received. Reagent grade triethylamine (TEA) and dichloromethane (CH<sub>2</sub>Cl<sub>2</sub>) were

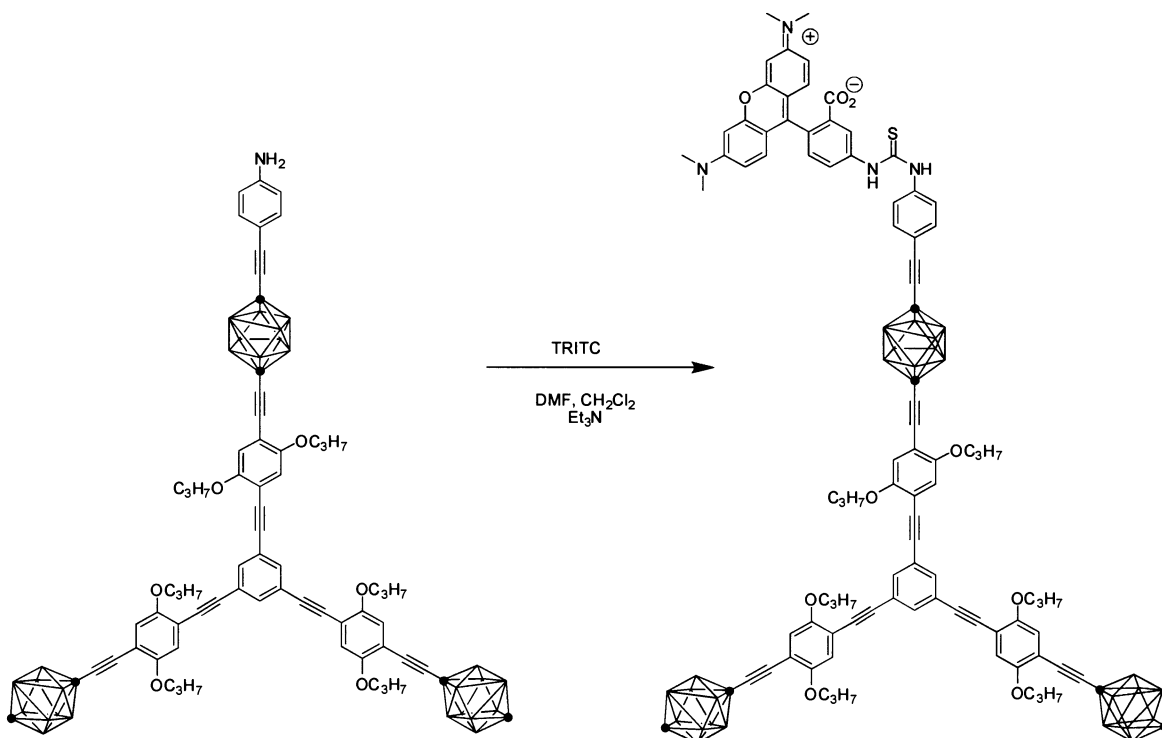
distilled over  $\text{CaH}_2$ . Flash column chromatography was performed using 230-400 mesh silica gel from EM Science. Thin layer chromatography was performed using glass plates pre-coated with silica gel 40 F<sub>254</sub> purchased from EM Science.  $^1\text{H}$  NMR and  $^{13}\text{C}$  NMR spectra were recorded at 400 and 100 MHz, respectively. Proton chemical shifts ( $\delta$ ) are reported in ppm downfield from tetramethylsilane (TMS). All matrix-assisted laser desorption-ionization mass spectrometry (MALDI) were performed at the University of South Carolina Mass Spectrometry Laboratory and run in a CHCA matrix in positive ion mode. Infrared spectra (IR) assignments have  $2\text{ cm}^{-1}$  resolution.



**Scheme 4.1:** Synthesis of dye tagged 4-wheeled nanocars.

**Synthesis of the Dye-Labeled Nanocar.** Into a Schlenk tube under nitrogen the aniline nanocar (21 mg, 0.026 mmol) was dissolved in DMF (1.0 mL) and  $\text{Et}_3\text{N}$  (0.1 mL). Tetramethylrhodamine isothiocyanate (TRITC, 5.8 mg, 0.013 mmol) in DMF solution (1.0 mL) was added dropwise and the mixture was heated to  $60\text{ }^\circ\text{C}$  while stirring overnight in the dark. The solvents were then removed by distillation under reduced pressure. The resulting solid was purified by column chromatography ( $\text{SiO}_2$ ,  $\text{CH}_2\text{Cl}_2/\text{MeOH}$ , 9/1) to yield a purple solid (3.0 mg, 16%). IR (drop cast) 3349, 2960, 2921, 2851, 2615, 2359, 2342, 1737, 1596, 1510, 1249, 1185, 1112, 1039, 828,  $803\text{ cm}^{-1}$ ;  $^1\text{H}$  NMR (400 MHz,

CDCl<sub>3</sub>) δ 7.98 (br s, 1H), 7.82 (d, *J* = 8.8 Hz, 1H), 7.48 (m, 1H), 7.15 (m, 5H), 6.82 (m, 2H), 6.69 (d, *J* = 8.6 Hz, 2H), 6.50 (d, *J* = 2.0 Hz, 2H), 6.42 (dd, *J* = 7.6 Hz, *J* = 2.0 Hz, 2H), 4.01 (s, 6H), 3.00 (s, 12H), 3.00-1.47 (br m, 44H). The molecule was not soluble enough for <sup>13</sup>C analysis. MALDI calculated for C<sub>65</sub>H<sub>80</sub>B<sub>40</sub>N<sub>4</sub>O<sub>5</sub>S: 1462.0, found: 1462.2



**Scheme 4.2:** Synthesis of dye tagged 3-wheeled nanocars.

**Synthesis of the Dye-Labeled Three-Wheeled Nanocar.** Into a Schlenk tube under nitrogen, the trimer (15 mg, 0.011 mmol) was dissolved in DCM (1 ml) and Et<sub>3</sub>N (0.1 ml). TRITC (5 mg, 0.011 mmol) in DMF solution (1 ml) was added dropwise and the mixture was stirred overnight in the dark at room temperature. The solvents were removed by distillation under reduced pressure. The crude product was purified by column chromatography (SiO<sub>2</sub>, CH<sub>2</sub>Cl<sub>2</sub>/MeOH, 9/1) to yield a purple solid (9 mg, 45%).

IR (drop cast) 3350, 2961, 2924, 2853, 2615, 2369, 1596, 1500, 1421, 1365, 1349, 1218, 1188  $\text{cm}^{-1}$ ;  $^1\text{H}$  NMR (400 MHz  $\text{CDCl}_3$ )  $\delta$  8.05 (br s, 1H), 7.89 (d,  $J = 8.8$  Hz, 1H), 7.74 (br s, 1H), 7.58 (m, 1H), 7.52 (s, 3H), 7.20 (m, 4H), 7.05 (d,  $J = 9.5$  Hz, 1H), 6.85 (s, 3H), 6.72 (dd,  $J = 8.3$  Hz  $J = 2.0$  Hz, 2H), 6.71 (s, 3H), 6.67 (d,  $J = 2.0$  Hz, 2H), 3.88 (t,  $J = 6.5$  Hz, 6H), 3.82 (t,  $J = 6.5$  Hz, 6H), 3.21 (s, 12H), 3.00-1.47 (br m, 33H), 1.77 (m, 12H), 1.02 (m, 18H); MALDI calc'd for  $\text{C}_{93}\text{H}_{110}\text{B}_{30}\text{N}_4\text{O}_6\text{S}$ : 1784.1, found: 1785.1 (M+H).

#### 4.3.2 Sample preparation

TRITC and TRITC labeled nanocars were spin-casted (3500 rpm for 90 seconds) on plasma cleaned coverslips (Fisher Scientific, 12-545-F) from DMF solution with concentrations of  $10^{-10}$  -  $10^{-12}$  mol/L. Prior to spin-casting and plasma cleaning, the coverslips were sonicated in acetone for 15 minutes. DMF was purchased from Sigma-Aldrich and used as received.

#### 4.3.3 Single molecule imaging

Single molecule fluorescence imaging was performed on a home-built sample scanning confocal microscope consisting of a frequency doubled diode-pumped laser (Coherent, Verdi), an inverted microscope (Zeiss, Axiovert 200), and avalanche photodiode (APD) detectors (Figure 4.1). Samples were mounted on a xyz piezo scanning stage (Physik Instrumente, P-517.3CL) connected to a surface probe microscope

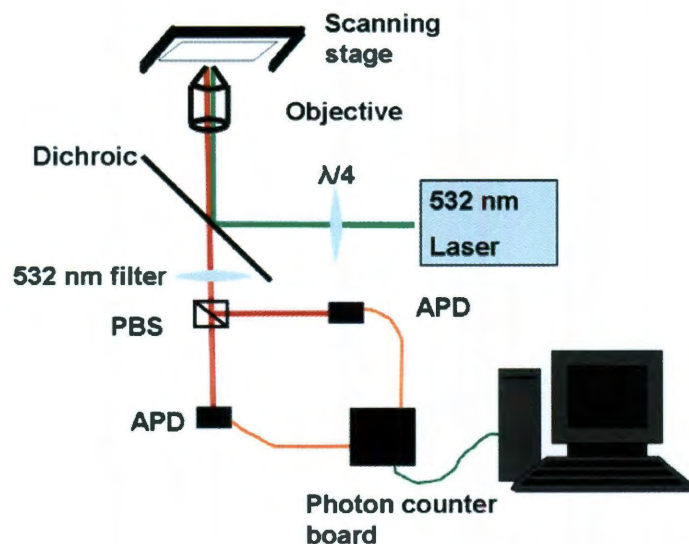


**Figure 4.1.** Scheme of sample scanning confocal microscope. Samples were excited by a circularly polarized 532 nm laser source focused by a high numerical aperture oil immersion objective. Linearly polarized fluorescence is divided by a polarization beam splitter (PBS) and collected by two avalanche photodiode (APD). Fluorescence images are acquired by scanning the sample across the laser beam with the scanning stage.

controller (RHK Technology, SPM 1000) and were excited by circularly polarized 532 nm laser light with an average power of 500 nW focused to a diffraction limited spot size of 250 – 300 nm. Emitted fluorescence from individual molecules was collected by a 100X oil-immersion objective with a numerical aperture of 1.3 (Zeiss, Fluar) and filtered by a dichroic mirror and a notch filter to reduce scattered laser light. Fluorescence images were constructed by scanning the sample across the excitation laser. Typical images had dimensions of 10 x 10  $\mu\text{m}$  and consisted of 128 x 128 pixels with an integration time of 1 ms/pixel (Figure 4.2B). Matlab software was written to automatically identify the position of each molecule in every image frame. For polarization sensitive detection, the fluorescence was separated into orthogonally polarized components  $I_x$  and  $I_y$  using a polarizing beamsplitter and detected by two APDs. After integrating the intensities over



an area of 5x5 pixels corresponding to the size of a single molecule, the polarization anisotropy was calculated according to  $P = (I_y - I_x)/(I_y + I_x)$ .

#### 4.4 Results and discussions

Fluorescence visualization of the nanocars with 532 nm excitation light was achieved by first attaching an appropriate dye label TRITC to the end of the nanocar

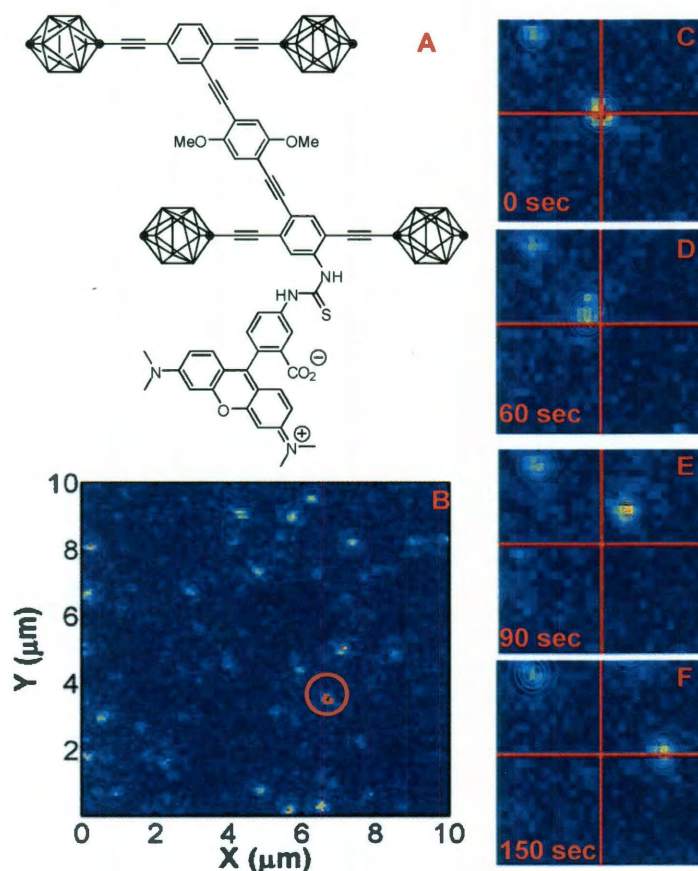


**Figure 4.2.** (A) Dye labeled four-wheeled nanocar. The vertices in the carborane wheels correspond to B-H units while the black dots correspond to C and C-H units, ipso and para, respectively. The nanocar is  $\sim 2 \times 2$  nm and the dye “trailer” is  $\sim 1 \times 1$  nm. (B) Fluorescence image ( $10 \mu\text{m} \times 10 \mu\text{m}$ ,  $128 \times 128$  pixels,  $1 \text{ ms/pixel}$ ,  $\lambda_{\text{exc.}} = 532 \text{ nm}$ ,  $1 \text{ kW/cm}^2$ ) of single nanocars. (C-F) Time-lapse images ( $2.3 \mu\text{m} \times 2.3 \mu\text{m}$ ) for the nanocar circled in (B) demonstrating movement of the nanocar at room temperature. The red cross hair provides a stationary reference point.

chassis (Figure 4.2 A). TRITC tagging of the nanocars was accomplished through an aniline-bearing nanocar reacting with the isothiocyanate residue on the fluorophore. At room temperature without thermal activation, the dye-labeled carborane-wheeled nanocars showed significant displacement in successively scanned fluorescence images directly confirming movement of the nanocars on a glass surface. Individual nanocars were isolated on a glass surface by spin-casting from a  $10^{-12}$  mol/L DMF solution. Single photobleaching steps in fluorescence-time trajectories confirmed the presence of single molecules within the diffraction limited fluorescence signal.<sup>130</sup>  $10 \times 10 \mu\text{m}$  fluorescence images were acquired by scanning the sample over a focused laser beam in a home-built confocal microscope setup (Figure 4.2 B). Movement of a single nanocar is shown in the images in Figs. 4.2C – 4.2F. The images were acquired continuously every 30 sec. for a total time of 5 min.

Single nanocar trajectories were obtained by an automated routine that first identified individual molecules based on the intensity and size (e.g. number of pixels) of the fluorescent spot in the starting image for a time series of frames. If a molecule is found at the same position or within a search area in the subsequent frame, the molecule is associated with the corresponding one in the previous image. This procedure is repeated for all molecules and every frame. Large displacements within the relatively long image acquisition time of 30 sec., photo-blinking of the dye, and high single molecule coverage could lead to an incorrect association. This was addressed by excluding all data points for which an unambiguous assignment could not be made. In addition, the dimensions of the search area and the concentration of nanocars were carefully adjusted in order to minimize intersecting search regions. A typical search

radius was 600 nm for images with coverages of 10 - 15 molecules per 100  $\mu\text{m}^2$ . Figure 4. 3A shows the first analyzed frame of a time series of fluorescence images for carborane-wheeled nanocars together with superimposed trajectories obtained from the following images demonstrating that the displacements of individual nanocars can be as large as 500 nm between frames.

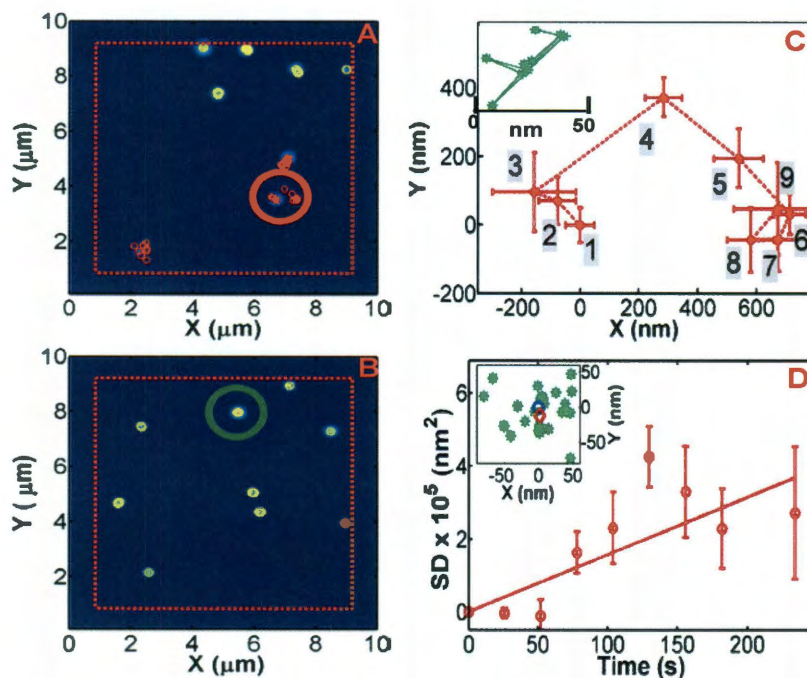


**Figure 4.3.** Analyzed images of nanocar (A) and TRITC (B). Molecules were identified based on intensity and size within the region marked by the red box. The positions of the molecules for a time series of images are shown superimposed on the first frame. 25% of the nanocars showed displacements greater than the error of 100 nm in at least two image frames and are color coded in red as ‘moving’ nanocars. (C) Single molecule trajectory of the nanocar indicated by the red circle in (A). Displacements as large as 500 nm between frames far exceed the changes in position recorded for the representative TRITC molecule labeled with the green circle in (B) (upper left hand corner in (C); note the scale bar). (D) Squared displacements  $SD$  ( $r^2$ ) calculated from the single nanocar trajectory in (C) vs. time. A linear fit according to  $SD = 4dt$  yields a squared displacement rate  $d$  of  $6.7 \times 10^{-16} \text{ m}^2/\text{s}$ . The inset shows a scatter plot of the linear displacements between images for each of the five ‘non-moving’ molecules in (A). The 11 nm shift between the blue and red points, corresponding to the origin and the mean position, confirms a negligible sample drift.

A non-specific movement of individual molecules on glass can be excluded here because fluorescence imaging of the dye only showed no measurable displacements outside our experimental error. We repeated the same single molecule experiments and analysis for individual TRITC molecules isolated on a glass surface (Figure 4.3B). The TRITC by itself showed no translational motion, which can be seen from the comparison of two typical trajectories obtained for the nanocar and TRITC (Figure 4.3C). The magnified nanocar trajectory in Figure 4.3C includes the error bars calculated from fitting each fluorescence spot to the microscope point spread function, which was approximated as a two-dimensional Gaussian.<sup>129,130</sup> For TRITC, the displacements are comparable or even smaller than the error bars verifying that the TRITC molecules remained stationary. On the other hand, the movement of the nanocars is much larger than our spatial resolution of 100 nm. The resolution is mainly limited by photon shotnoise and photoblinking of the dye as well as a pixel size of 78 nm.<sup>129</sup> Despite a longer image acquisition time and reduced spatial resolution, the main advantage of our confocal sample scanning setup over wide-field imaging is that a non-constant laser illumination of all molecules allowed us to extend the total acquisition time and to obtain trajectories spanning several minutes.

It is interesting to note from Figure 4.3A that not all molecules that were identified actually moved. In fact, about 25 % of the nanocars showed translational motion, which further illustrates the power and need for single molecule measurement techniques. A main factor contributing to the large fraction of ‘non-moving’ nanocars is most likely the surface roughness of the glass surface as it is not atomically flat; it is merely a glass cover slip (Fisher Scientific, 12-545-F) and the nanocars could become

lodged at lattice defects. Secondly, a fluorescent spot only indicates the presence of TRITC, which by itself did not move (Figure 4.2B), and the presence of some non-linked TRITC molecules due to decomposition cannot be excluded. In the following, we will concentrate only on the nanocars that showed a displacement which exceeded the error bar in at least 2 image frames. These ‘moving’ nanocars are colored red in Figure 4.3A. However, the ‘non-moving’ nanocars colored yellow in Figure 4.3A served the important role of an internal marker against overall sample drift. We found that sample drift (inset in Figure 4.3D) was 11 nm during the experiment shown in Figure 4.3, which is much smaller than the micron-scale movement of the nanocars as well as our spatial resolution of 100 nm.

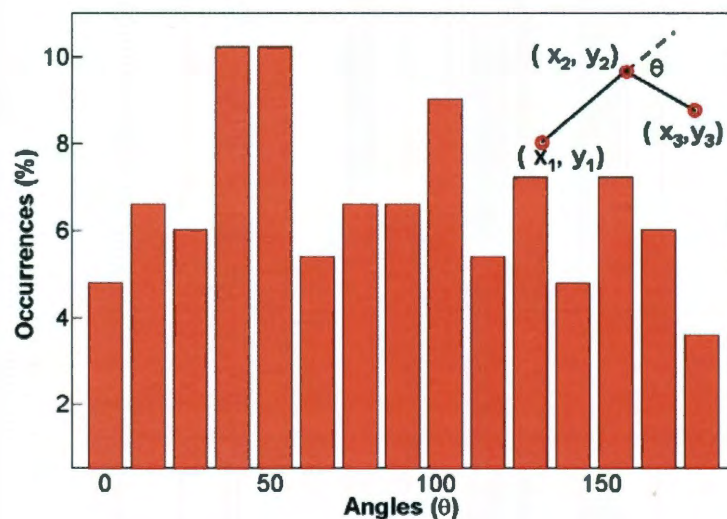


**Figure 4.4.** Directionality of nanocar movement. To evaluate if the nanocars showed motion with a preferential direction, we calculated the angular displacements  $\theta$  (Inset) from unidirectional translation using the single molecule trajectories. The equal distribution over all possible values of  $\theta$  indicates movement in all directions without a bias for directional motion. Translation along a straight line would result in a histogram that is peaked at zero.

We observed no biased movement of the nanocars on this amorphous surface. A histogram of angles obtained from the single molecule trajectories for all moving

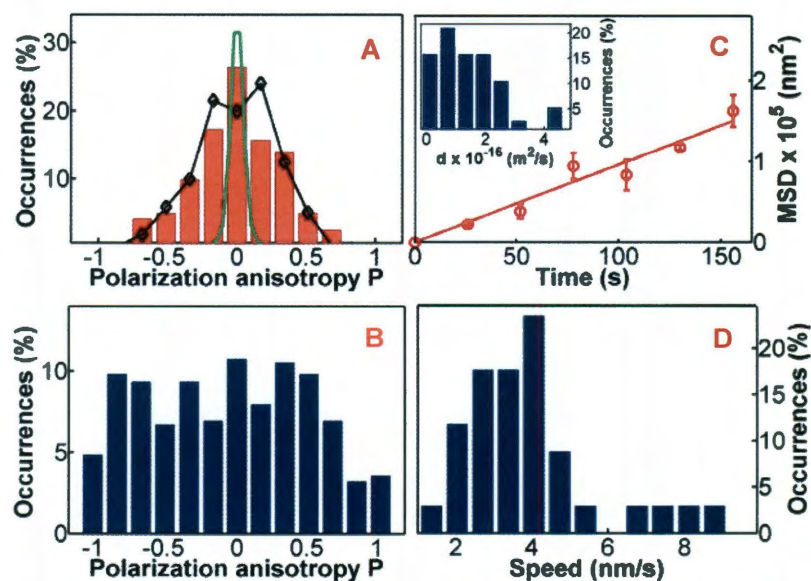


**Figure 4.5.** (A) Polarization anisotropy distribution of ‘moving’ four-wheeled nanocars (red bars). The polarization anisotropy values are peaked at zero, indicating rotation of the nanocars during the image acquisition time. Rotation much faster than the acquisition time would result in the distribution given by the green line for shotnoise limited polarization detection. The black points and line are a simulation of the polarization anisotropy distribution for random hopping with a minimum rate of 10 hops per second, assuming an equal weight for all hopping directions. (B) Polarization anisotropy distribution of TRITC confirming the absence of rotational motion during the image acquisition time. (C) Mean squared displacement  $MSD$  ( $\langle r^2 \rangle - \langle r \rangle^2$ ) vs. time for all ‘moving’ nanocars. A linear fit according to  $MSD = 4Dt$  yields a two-dimensional diffusion constant  $D$  of  $2.7 \times 10^{-16} \pm 0.4 \text{ m}^2/\text{s}$ . The inset shows a histogram of single molecule squared displacement rates  $d$  calculated from individual trajectories such as the one shown in Figure 4.3D. (D) Distribution of speeds of individual ‘moving’ nanocars. The average speed of the nanocars is 4.1 nm/s or two nanocar lengths per second.

nanocars showed an equal distribution of all angles between 0 and 180 degrees (Figure 4.

4). Polarization anisotropy analysis of the fluorescence images furthermore revealed that the nanocars, when they changed directions, underwent the change rapidly and within the time it took to scan the molecule over the laser beam ( $\sim 500 \text{ ms}$ , Figure 4.5A). The polarization anisotropy distribution of the nanocars is peaked at zero indicating depolarization due to rotational movement. A rotation of the TRITC on the nanocar can be excluded as the major depolarization mechanism because an analysis of only the center pixel showed a broader polarization distribution (Figure 4.6). This is consistent

with rotational dynamics on the 1-100 ms time scale and is much slower than a bond rotation. In contrast, TRITC only did not rotate as the polarization anisotropy values for TRITC (Figure 4.5B) ranged from -1 to 1 consistent with a random and stationary distribution of molecular orientations.<sup>131,132</sup> The fact that the molecules rotate is not surprising, considering that previous STM results<sup>50</sup> showed a combined pivot and translation motion of fullerene-wheeled nanocars on the nanometer length scale due to an independent wheel movement. The roughness of the glass surface is likely to further enhance pivoting of the nanocars.

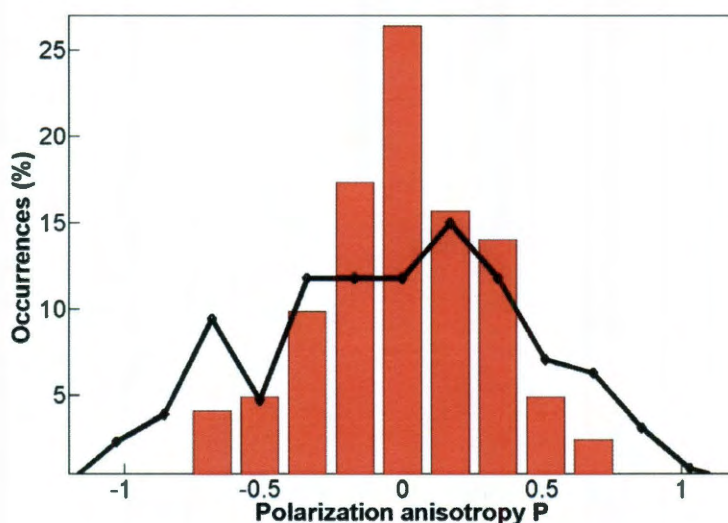


**Figure 4.6:** Polarization anisotropy distribution of ‘moving’ four-wheeled nanocars. The polarization anisotropies were calculated by integrating over the area of the single molecules (5x5 pixels, red bars) and the center pixel with the highest intensity only (black line). Because of the scanning image acquisition, the different integration areas correspond to integration times of 500 ms and 1 ms, respectively. The polarization anisotropy distributions are peaked at zero indicating depolarization due to rotational movement. However, the larger width in the polarization anisotropy distribution for the center pixel suggests that rotational dynamics occur on the 1-100 ms time.

Given the lack of long-range directionality, we analyzed the single nanocar trajectories to obtain displacement rates in analogy to two-dimensional surface diffusion.<sup>133</sup> Figure 4.3D shows the squared displacement  $SD$  of a single nanocar vs.

time as obtained from the trajectory in Figure 4.3C. A linear fit according to  $SD = 4dt$  yields a squared displacement rate  $d$  of  $6.7 \times 10^{-16} \text{ m}^2/\text{s}$ . A histogram of single molecule diffusion constants is shown in the inset of Figure 4.5C. The average single molecule squared displacement rate of  $2.2 \times 10^{-16} \text{ m}^2/\text{s}$  agrees well with the diffusion constant  $D$  of  $2.7 \times 10^{-16} \text{ m}^2/\text{s}$  calculated from a mean squared displacement  $MSD$  analysis ( $MSD = 4Dt$ , Figure 4.5C). We also calculated the average minimum speed of the four-wheeled nanocars at room temperature and found a value of 4.1 nm/s (Figure 4.5D). Based on a diameter of 0.8 nm for a carborane wheel and assuming here that the translation was purely due to a rolling mechanism, a minimum wheel rotation frequency of 2 rotations per second was calculated. In contrast, fullerene-wheeled nanocars on a gold surface only moved after increasing the temperature to 500 K.<sup>50</sup> The difference is due to the much larger surface interaction energy of 200 - 250 kJ/mol per fullerene wheel on gold.<sup>134,135</sup>

Instead of a wheel-like rolling motion, the nanocars could also translate by hopping as has been observed for a large organic molecule such as hexa-*tert*-butyldecacyclene (HtBDC, C<sub>60</sub>H<sub>66</sub>), on Cu (110) by STM imaging.<sup>136</sup> We evaluated this scenario using the measured diffusion constant and estimating a minimum hopping rate based on the polarization anisotropy distribution of the nanocars. A simulation of the polarization anisotropy distribution (Figure 4.5A), assuming random hopping with an equal weight for all directions, gives a minimum hopping rate  $h$  of 10 hops per second. According to  $D = 1/4 \lambda^2 h$ ,<sup>137</sup> a maximum hop length  $\lambda$  of 10 nm is calculated, which is several times the size of the nanocar. If the nanocars are unable to rotate freely while



hopping, the hopping rate increases and the step size decreases, which eventually will become indistinguishable from a sliding or rolling motion.

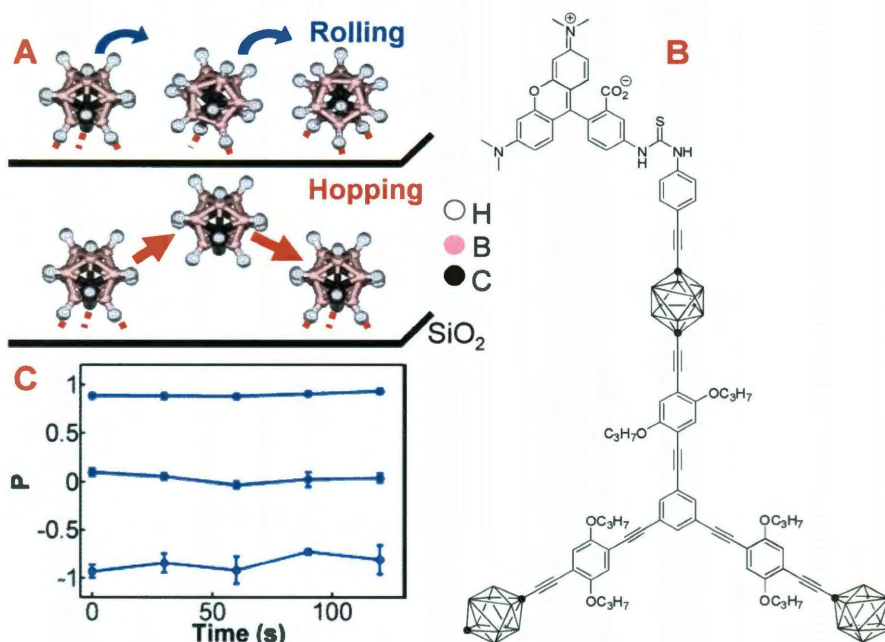


**Figure 4.7.** (A) Schematic comparison of a carborane wheel rolling (top) vs. hopping (bottom). A wheel on the glass surface forms three hydrogen bonds with the oxygen atoms (not shown for clarity) of the SiO<sub>2</sub>. For rolling only one of the three hydrogen bonds has to break while for hopping the whole wheel has to detach from the surface. (B) Dye labeled three-wheeled nanocar. (C) Three representative polarization anisotropy time trajectories for trimer nanocars showing that rotational motion is absent on a time scale of several minutes. Similar results were also obtained for polarization measurements of ‘non-moving’ four-wheeled nanocars and TRITC only.

Using a simple model, we can estimate the contributions due to rolling and hopping of the nanocars based on the activation energy for translational motion, which can be estimated from the measured diffusion constant  $D$  according to

$$D = D_0 \exp\left(-\frac{E}{kT}\right).^{137,138}$$

Here,  $T$  is the temperature and  $k$  the Boltzmann constant.  $D_0$  is

the two-dimensional diffusion constant of the nanocar in air given by the Stokes-Einstein

$$\text{diffusion equation } D_0 = \frac{kT}{4\pi\eta a}$$

where  $\eta$  is the viscosity of air and  $a$  is the radius of the

nanocar. If the motion of the nanocar molecule on the surface were free it would have a

diffusion constant  $D_0$ . However, because of interactions with the surface the diffusion is significantly smaller. This model yields an activation energy  $E$  of  $42 \pm 5$  kJ/mol at room temperature. For a carborane wheel to sit on a surface, three hydrogen atoms are necessary to bond to the substrate, which is illustrated in Figure 4.7A together with a suggested rolling mechanism. The bond strength between a carborane hydrogen and an oxygen atom on the glass surface is estimated to be 4.8 kJ/mol.<sup>139</sup> In order for the nanocar to roll it has to break one hydrogen bond per wheel and overcome a rotational energy barrier of 4.2 kJ/mol per bond connecting the wheel to the chassis,<sup>46</sup> which equals a total energy of 36 kJ/mol for a total of four wheels per car, in good agreement with the measured activation energy. On the other hand, if the nanocars were hopping, 12 hydrogen bonds have to be broken yielding an activation energy of 57 kJ/mol. This exceeds the experimentally measured value making hopping the less likely mechanism.

In order to further test this assignment, we measured single molecule trajectories and polarization anisotropy distributions for a TRITC-labeled three-wheeled nanocar, (Figure 4.7B). Compared to the four-wheeled car, the trimer nanocar is expected to have only 75% of the interaction energy with the glass surface and would therefore be more likely to hop. However, we found no movement of the trimer nanocars as the trajectories were similar to those measured for TRITC only or the non-moving four-wheeled nanocars. In addition to the absence of any translational movement of the trimer nanocars, we also did not observe rotational motion as confirmed by the polarization anisotropy distribution obtained from the fluorescence images (Figure 4.8) and the absence of a change of polarization anisotropy between image frames (Figure 4.7C). Although the trimer nanocar is expected to rotate, an important difference between the

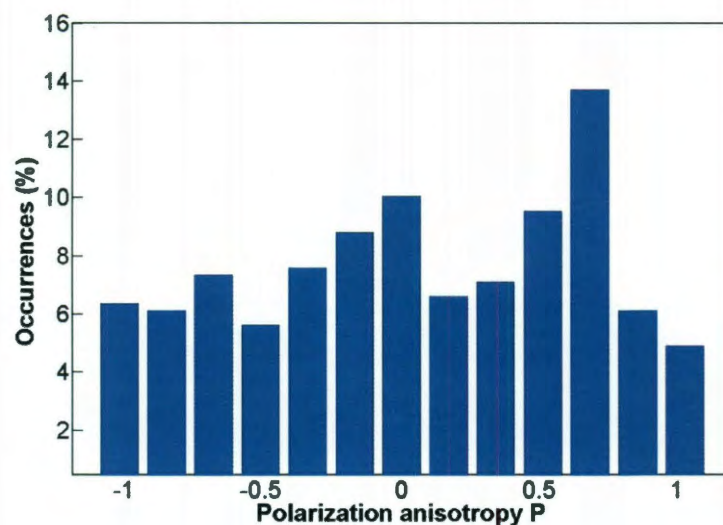


**Figure 4.8.** Polarization anisotropy distribution of three-wheeled nanocars. The equal distribution of polarization anisotropies over the entire region from -1 to +1 indicates the absence of rotational movement of the trimer nanocars within the acquisition time of 500 ms.

two nanocars is that TRITC is attached directly to the wheel of the trimer nanocar (Figs. 4.2A and 4.7B) and could hinder a free wheel rotation.

## 2.5 Conclusion

Using single molecule fluorescence imaging, we have observed micrometer movement of dye-labeled carborane nanocars on a glass surface at room temperature. Polarization-sensitive measurements showed that translation is coupled with rotational motion. By comparing the four-wheeled nanocars to a three-wheeled nanocar analog and the unbound dye molecules, we conclude that the translation of the nanocars is consistent with a wheel-like rolling mechanism. While atomic resolution as with STM is not possible using single molecule fluorescence imaging, the results presented here demonstrate that our approach yields complementary data and gives useful insights into the micrometer-scale motion of molecular machines.

It is interesting to speculate how a truly unidirectional motion of nanocars can be achieved. Our results suggest that the speed of the nanocars is dictated by the strength of the interactions between the nanocar wheels and the surface. Changing the surface should therefore have a large impact on the mobility of the nanocars. However, even more important for a controlled directional motion seems to be the reduction of pivoting, which was found to occur with a minimum frequency of 10 turns per second for the carborane-wheeled nanocars on glass. An extended nanocar chassis with an increased even number of wheels should be less susceptible to random pivot motion caused by an independent wheel movement, but at the expense of a reduced speed due to a stronger surface attraction and increased entropy for synchronized bond rotations.

## **2.6 Acknowledgements**

I thank Dr. Jason Gurrero and Dr. James M Tour with whom I collaborated on this project, Dr. Christy Landes and Dr. Kevin Kelly for useful discussions, RHK Technology for technical support, and Dr. Jason Hafner for letting us use the plasma cleaner. This work is supported by an NSF NIRT grant (ECCS-0708765), an NSF Penn State MRSEC, the Robert A. Welch Foundation (Grants C-1664 and C-1489), a 3M Nontenured Faculty Grant, and the Energy and Environmental Systems Institute (EESI) at Rice University.

## CHAPTER 5

# INFLUENCE OF THE SUBSTRATE ON THE MOBILITY OF INDIVIDUAL NANOCARS <sup>1</sup>

### 5.1 Abstract

We monitored the mobility of individual fluorescent nanocars on three surfaces; plasma-cleaned, reactive ion-etched, and amine-functionalized glass. Using single-molecule fluorescence imaging, the percentage of moving nanocars and their diffusion constants were determined for each substrate. We found that the nanocar mobility decreased with increasing surface roughness and increasing surface interaction strength.

### 5.2 Introduction

The desire to control motion at the nanoscale has led to the design of a range of different synthetic molecular machines that are inspired by macroscopic tools and devices<sup>37-45,126</sup>. Nanocars<sup>140</sup>, molecules with spherical fullerene or carborane wheels attached to a flexible aromatic chassis, are intended for targeted transport of atoms or molecules on surfaces.<sup>140</sup> The movement of individual nanocars on solid surfaces has been shown using scanning tunneling microscopy and fluorescence imaging, and found to be consistent with a “rolling”-type motion.<sup>50,57</sup> The key aim of those studies was to monitor the translation of the nanocars on a particular surface. The speed of the nanocars varied greatly among the individual nanocars, and a significant fraction of the nanocars did not move at all remaining “stationary” during the observation window.<sup>57</sup> To maximize the chance of successful transport of nanomaterials using nanocars as

---

<sup>1</sup> This chapter is based on the manuscript entitled “Influence of the Substrate on the Mobility of Individual Nanocars” by Saumyakanti Khatua, Jazmin Godoy, James M. Tour, and Stephan Link, published in the *Journal of Physical Chemistry Letters* **2010** 1, 3288-3291.

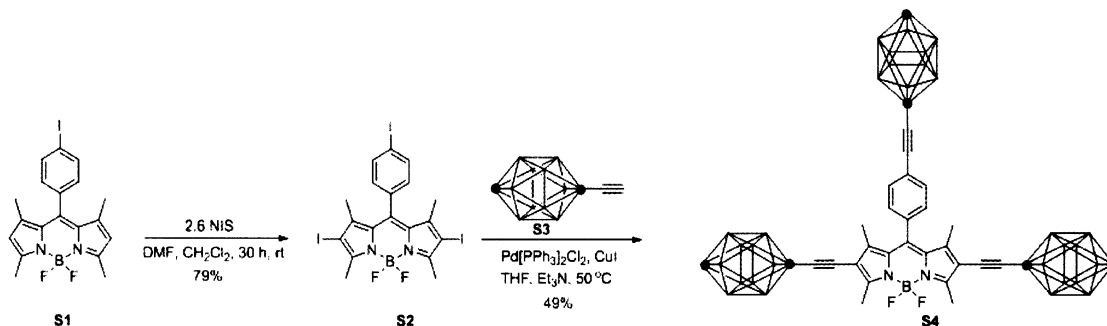
molecular transporter, it is therefore desirable to maximize the number of “moving” nanocars, to control their speed, and finally achieve control over the direction of their movement. In this study, we explore the effect of chemical nature and roughness of the surface on the mobility of individual nanocars.

### **5.3 Materials and methods:**

#### **5.3.1 General synthetic methods**

$^1\text{H}$  NMR and  $^{13}\text{C}$  NMR spectra were recorded at 400 or 500 and 100 or 125 MHz, respectively. Chemical shifts ( $\delta$ ) are reported in ppm from tetramethylsilane (TMS). FTIR spectra were recorded using a Nicolet FTIR Infrared Microscope with ATR objective and  $2\text{ cm}^{-1}$  resolution. Melting points were not recorded as the compounds did not melt below  $200\text{ }^\circ\text{C}$ . Reagent grade tetrahydrofuran (THF) was distilled from sodium benzophenoneketyl. Triethylamine ( $\text{Et}_3\text{N}$ ) and dichloromethane ( $\text{CH}_2\text{Cl}_2$ ) were distilled from  $\text{CaH}_2$  under  $\text{N}_2$  atmosphere. THF and  $\text{Et}_3\text{N}$  were degassed with a stream of argon for 30 minutes before being used in the Sonogashira coupling reaction. Hexanes were distilled. Optima grade chloroform ( $\text{CHCl}_3$ ) was used. All other chemicals were purchased from commercial suppliers and used without further purification. The reactions were conducted under nitrogen atmosphere. Flash column chromatography was performed using 230-400 mesh silica gel from EM Science. Thin layer chromatography was performed using aluminum plates pre-coated with silica gel 60 F<sub>254</sub> 0.20 mm layer thickness purchased from Sigma Aldrich. The synthesis and characterization of the BODIPY-based nanocar was reported previously<sup>141</sup>. The syntheses of BODIPY **S1**<sup>141</sup> and 1-ethynyl-*p*-carborane **S3**<sup>142</sup> was performed according to reported protocols.

### 5.3.2 Synthesis of BODIPY S2 and BODIPY-based trimer S4



**Scheme 5.1:** Synthesis of inherently fluorescent 3-wheeled nanocars.

**BODIPY S2:** A 25 mL round-bottomed flask equipped with a magnetic stir bar was charged with BODIPY **S1** (100 mg, 0.22 mmol), 5 mL of CH<sub>2</sub>Cl<sub>2</sub>, and 5 mL of DMF. *N*-iodosuccinimide (130 mg, 0.58 mmol) was added and the orange solution was stirred at room temperature for 30 hours. A red solution was obtained. The CH<sub>2</sub>Cl<sub>2</sub> was removed under vacuum and the residue was treated with 10 mL of water. The mixture was then extracted with Et<sub>2</sub>O (25 mL × 3). The combined organic fractions were mixed with 20 mL of CH<sub>2</sub>Cl<sub>2</sub> and then dried with MgSO<sub>4</sub>. The solvent was removed under vacuum and the residue was purified by flash column chromatography (silica gel, 40% CH<sub>2</sub>Cl<sub>2</sub> in hexanes) to provide **S2** (123 mg, 0.17 mmol, 79%) as a red solid. FTIR (neat) 2957, 2918, 2850, 2360, 2341, 1539, 1400, 1190, 1181 cm<sup>-1</sup>; <sup>1</sup>H NMR (400 MHz, CDCl<sub>3</sub>, ppm) δ 7.88 (d, 2H, *J* = 8.0 Hz), 7.02 (d, 2H, *J* = 8.0 Hz), 2.64 (s, 6H), 1.43 (s, 6H); <sup>13</sup>C NMR (100 MHz, CDCl<sub>3</sub>, ppm) δ 157.4, 145.3, 139.9, 138.9, 134.5, 131.2, 129.9, 95.6, 86.2, 17.5, 16.3; EI-HRMS *m/z* calcd for C<sub>19</sub>H<sub>15</sub>BF<sub>2</sub>I<sub>3</sub>N<sub>2</sub> [M-H]<sup>-</sup> 700.8428, found 700.8439.

**BODIPY-based trimer S4:** A Schlenk tube equipped with a magnetic stir bar was filled with **S2** (100 mg, 0.14 mmol), **S3** (110 mg, 0.64 mmol), Pd[PPh<sub>3</sub>]<sub>2</sub>Cl<sub>2</sub> (10 mg,

14.2  $\mu\text{mol}$ ), CuI (5.5 mg, 28.4  $\mu\text{mol}$ ), THF (9 mL), and Et<sub>3</sub>N (3 mL). The solvent mixture of THF: Et<sub>3</sub>N = 3:1 was well-degassed under argon for 30 minutes prior to addition of the reactants. The solution was stirred overnight at 50 °C. The reaction was quenched with a saturated solution of NH<sub>4</sub>Cl. The organic layer was diluted with CH<sub>2</sub>Cl<sub>2</sub> two times. The aqueous layer was extracted with CH<sub>2</sub>Cl<sub>2</sub> once. The combined organic layers were dried over MgSO<sub>4</sub>. The solvent was removed under vacuum and the residue was purified by column chromatography (silica gel, 30-35% CHCl<sub>3</sub> in hexanes) to provide **S4** (57 mg, 0.069 mmol, 49%) as a red solid. FTIR (neat) 3066, 2922, 2852, 2609, 2360, 2342, 1537, 1476, 1394, 1319, 1261, 1186, 1057, 1013 cm<sup>-1</sup>; <sup>1</sup>H NMR (500 MHz, CDCl<sub>3</sub>, ppm)  $\delta$  7.43 (d, 2H,  $J = 8.0$  Hz), 7.09 (d, 2H,  $J = 8.0$  Hz), 3.3–1.7 (br m, 39H), 1.28 (s, 6H); <sup>13</sup>C NMR (125 MHz, CDCl<sub>3</sub>, ppm)  $\delta$  159.2, 145.3, 141.9, 134.8, 133.0, 130.9, 128.0, 123.0, 114.7, 93.3, 87.3, 78.3, 72.0, 70.0, 69.3, 60.6, 59.9, 13.7 (overlap of two CH<sub>3</sub>); EI-HRMS  $m/z$  calcd for C<sub>31</sub>H<sub>48</sub><sup>11</sup>B<sub>25</sub><sup>10</sup>B<sub>6</sub> F<sub>2</sub>N<sub>2</sub> [M-H]<sup>-</sup> 821.6819, found 821.6856.

### 5.3.3 Surface modification

Hydroxyl-terminated glass was prepared by exposing the glass surface to oxygen plasma (Harrick Plasma) for 45 seconds. Hydroxy-terminated, but roughened glass substrates were prepared by reactive ion etching (Trion Technology) using the following conditions: 5 sccm O<sub>2</sub>, 10 sccm CF<sub>4</sub>, 100 W RF power, 30 mTorr total pressure. For the Vectabond<sup>TM</sup> treatment of the glass, plasma cleaned glass coverslips were immersed into Vectabond<sup>TM</sup> reagent solution (Vector Laboratories, 20  $\mu\text{l/ml}$  in Acetone) for 5 min.<sup>143</sup> The coverslips were then taken out of the Vectabond<sup>TM</sup> solution and rinsed with molecular biology grade water (Thermo Scientific) for 30 seconds and dried under



nitrogen. The Vectabond™ treatment changes the surface functionality from hydroxyl- to amine-terminated. All solvents used in these experiments were of spectroscopic grade and were used as received. Blank tests were always performed before nanocar deposition to test for fluorescence impurities from the solvent and the substrate.

### 5.3.4 AFM imaging on different surfaces

AFM imaging was performed on plasma cleaned glass, Vectabond™ treated glass, and plasma etched glass using a Nanoscope IIIA atomic force microscope. The average surface roughness of these substrates were measured to be  $0.4 \pm 0.1$  nm (glass),  $2.6 \pm 0.2$  nm (etched glass), and  $0.5 \pm 0.2$  nm (Vectabond™ treated glass).

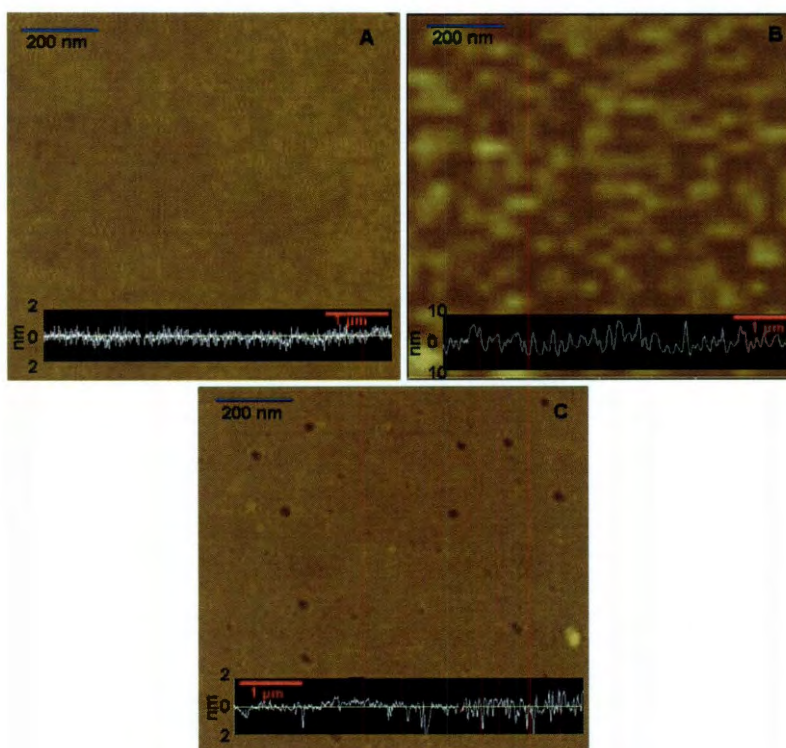


**Figure 5.1.** AFM images ( $1 \mu\text{m} \times 1 \mu\text{m}$ ) of plasma cleaned glass (A), etched glass (B), and Vectabond™ treated glass (C). The insets show line scans taken on each surface. The average surface roughness of these surfaces was measured to be  $0.4 \pm 0.1$  nm (glass),  $2.6 \pm 0.2$  nm (etched glass), and  $0.5 \pm 0.2$  nm (Vectabond™ treated glass). The error was determined from several independent areas of the same and different substrates. Surface holes (dark spots) are seen for Vectabond™ treated surfaces, which are as big as 50 nm in

diameter and 5 nm in height. They are most likely due to an uneven surface functionalization, but contribute at most 3 % to the total surface area.

### **5.3.5 Sample preparation**

Single nanocars were isolated on different substrates by spin coating them from a  $10^{-12}$  mol/L solution in chloroform (Sigma Aldrich) at 3000 rpm for 60 seconds. Chloroform was purchased from Sigma Aldrich and used as received.

### **5.3.6 Single molecule spectroscopy**

Single-molecule fluorescence images were taken with a home-built confocal microscope consisting of a 514 nm Ar<sup>+</sup> laser (Modu-Laser) as the excitation source, an inverted microscope (Zeiss Axiovert 200), a xyz piezo scanning stage (Physik Instrumente), an oil-immersion objective lens (Zeiss Fluar), and two avalanche photodiodes (Perkin-Elmer). The nanocars were excited using circularly polarized light with a power of 500 nW. Fluorescence was separated from the laser excitation using appropriate dichroic and notch filters. The fluorescence images were formed by scanning the sample across the focused laser beam with the scanning stage. Image dimensions were 10  $\mu$ m x 10  $\mu$ m and consisted of 128 x 128 pixels with an integration time of 1 ms/pixel. The S/N ratio was comparable for all substrates suggesting that the results were not influenced by different degrees of fluorescence quenching through nanocar-surface interactions. All experiments were repeated at least three times starting every measurement with the preparation of the substrates, nanocar deposition, and fluorescence imaging. The average diffusion constants obtained for each measurement were used to calculate the reported errors.

## 5.4 Results and discussions

As a first step towards controlling the mobility of these nano-transporters, we studied the movement of inherently fluorescent nanocars with carborane wheels on different surfaces. This new nanocar model incorporated axles that were based on the

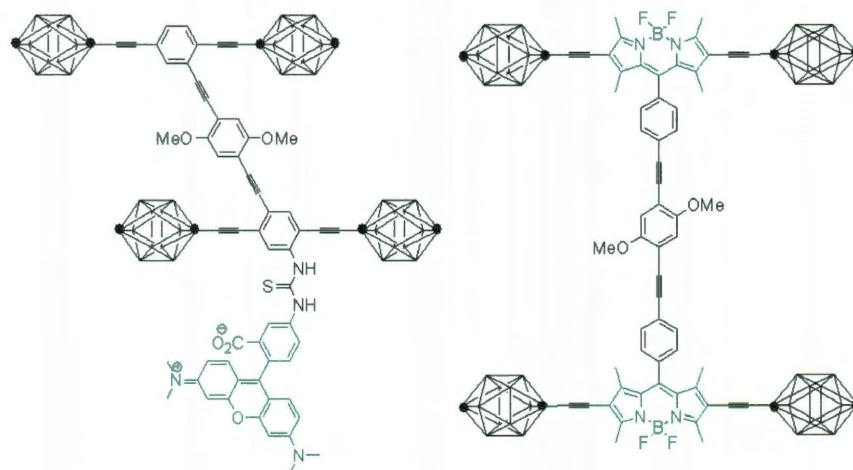


**Figure 5.2:** Chemical structure of the TRITC-tagged (left) and BODIPY-based (right) nanocar with p-carborane wheels, where the black dots indicate the para-carbon atoms.

fluorophore BODIPY (4,4-difluoro-4-bora-3a,4a-diaza-s-indacene, Figure 5.2, right).<sup>141</sup>

The mobility of individual BODIPY-based nanocars was determined from time-lapsed confocal fluorescence images.<sup>144</sup> Figure 5.3A shows the first of a series of images taken for nanocars dispersed on plasma cleaned glass coverslips. The bright spots in the fluorescence image correspond to individual nanocars. As illustrated in Figure 5.3B, XY trajectories of the nanocar motion were computed from the entire series of images taken over the same area using a single-molecule tracking algorithm that can account for fluorescence blinking and bleaching.<sup>144</sup> The single-molecule trajectories were each analyzed to give a 2-dimensional diffusion constant (Figure 5.3C), enabling a quantitative comparison between different nanocars and surfaces.

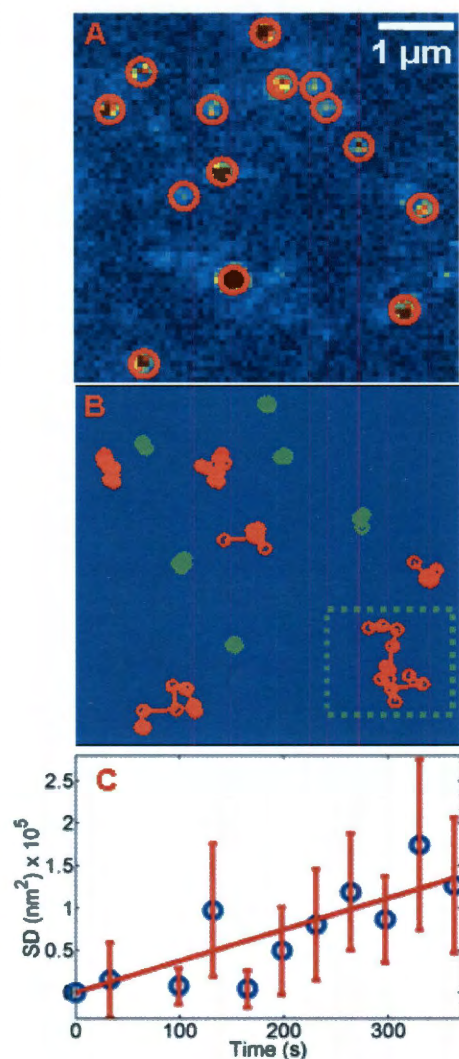


**Figure 5.3:** (A) First of a time series of fluorescence images for single nanocars on a plasma cleaned glass substrate. Individual nanocars indicated by the red circles were identified based on a threshold intensity. (B) XY trajectories of the nanocars identified in (A). Trajectories colored red and green indicate “moving” and “stationary” nanocars, respectively. (C) Squared displacements  $SD$  vs. time  $t$  calculated from the single nanocar trajectory surrounded by the green dotted square in (B). A linear fit according to  $SD = 4Dt$  gives a diffusion constant  $D = 4.6 \times 10^{-16} \text{ m}^2/\text{s}$ .

Not all nanocars in Figure 5.3B showed movement within our diffraction-limited spatial resolution as indicated by the different colors. We previously found a similar anisotropy in the movement of a collection of individual nanocars, which also had the *p*-carborane wheels but were tagged at the nanocar axle with a dye molecule (Figure 5.2, left).<sup>57</sup>

Tetramethylrhodamine isothiocyanate (TRITC) was used as the dye to visualize those nanocars by fluorescence microscopy. However, TRITC was about half the nanocar size itself. Here we found that a significantly greater fraction of the BODIPY-based nanocars (45% out of 279) showed movement under the same experimental conditions compared to the TRITC-tagged nanocars (25% out of 191). This increase in the percentage of moving nanocars is likely due to the bulky TRITC tag. Future experiments, using for example a TRITC-tagged BODIPY-based nanocar, will verify this conclusion.

To verify that the movement for the majority of the nanocars is consistent with a rolling-type motion, we separately measured a BODIPY-based trimer. Under the same experimental condition, we found that ~10% of the trimers moved on plasma cleaned glass. Because of the perpendicular orientation of the third wheel, a rolling-type motion is hindered, as indeed found experimentally. The opposite trend is expected for motion by hopping or slipping due to the decrease in the number of wheels and hence the surface interaction. While the percentage of moving nanocars increased by almost a factor of 2 compared to the TRITC-tagged nanocars, their average diffusion constant on glass remained unchanged (line in Figure 5.4A). Because both BODIPY-based and TRITC-tagged nanocars had the same *p*-carborane wheels, it is expected that they experience comparable interactions with the surface. The similar distributions of diffusion constants for these two nanocars indeed suggests that the mobility of the nanocars is mainly governed by the interactions between the substrate and the nanocar wheels, and independent of the nanocar chassis.

To further investigate how the substrate influences the percentage of moving nanocars and their diffusion constants, we measured BODIPY-based nanocars on reactive

ion etched glass (Figure 5.4B) and Vectabond™ treated glass coverslips (Figure 5.4C). The latter changes the surface functionality from hydroxyl to amine termination.<sup>143</sup> We observed a decrease in the number of moving nanocars and diffusion constants for both of these substrates. While on plasma cleaned glass almost 45% of the nanocars moved,

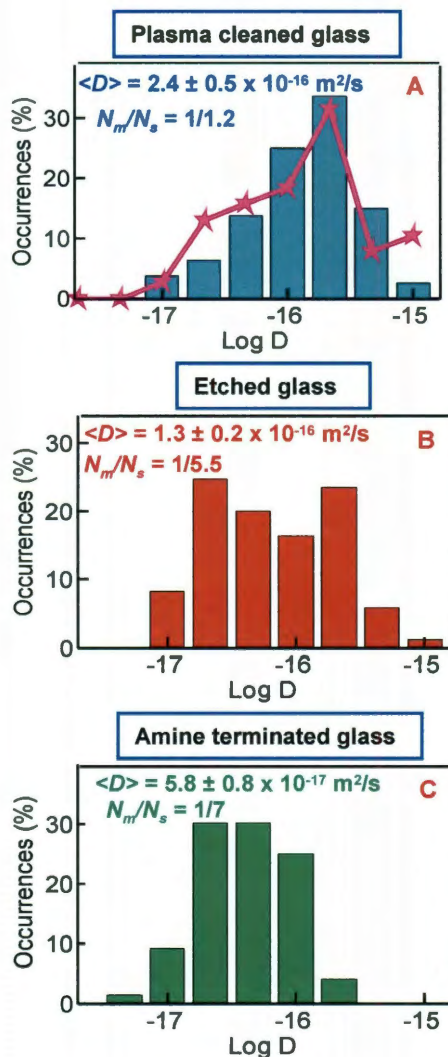


**Figure 5.4:** (A) Distribution of single-molecule diffusion constants  $D$  for the moving BODIPY nanocars on glass (bars). For comparison, the histogram of diffusion constants for a TRITC-tagged nanocar with carborane wheels moving on a glass surface is also included (line). The mean diffusion constants are nearly identical with  $\langle D \rangle = 2.4 \times 10^{-16} \text{ m}^2/\text{s}$  and  $\langle D \rangle = 2.2 \times 10^{-16} \text{ m}^2/\text{s}$ , for the BODIPY-based and TRITC-tagged nanocars, respectively. (B,C) Histograms of diffusion constants for nanocars on reactive ion etched and amine-terminated glass.  $N_m$  and  $N_s$  are the number of moving and stationary nanocars.

on Vectabond<sup>TM</sup> treated glass the percentage dropped to 13% with a decrease in the average diffusion constant by a similar factor of about 4. With these experiments we have separately varied two important factors: 1) the surface roughness and 2) the interaction potential between the carborane wheels and the substrate.

Considering first the effect of surface roughness, we determined the height variations of the plasma cleaned and the ion etched glass coverslips using AFM). The average surface roughness for these two substrates was  $0.4 \pm 0.1$  nm and  $2.6 \pm 0.2$  nm (Figure 5.1A and 5.1B). With increasing roughness the percentage of moving nanocars decreased to 18% with a drop in average diffusion constant by a factor of almost 2. While the interaction between the nanocar wheels and the substrate remained unchanged, the height variation for the etched glass was comparable to or could even locally exceed the dimensions of the nanocar. It is therefore likely that the nanocars were stuck at surface bumps, which is also consistent with a rolling- type motion instead of surface hopping.

The percentage of moving nanocars dropped even more for Vectabond<sup>TM</sup> treated glass (Figure 5.4C), although its surface roughness was similar to the untreated coverslips (Figure 5.1). An uneven amine functionalization of the surface led to holes on these substrates, which were as big as 50 nm in diameter and 5 nm in height and could have trapped the much smaller nanocars. However, a more detailed AFM analysis revealed that the holes constitute less than 3% of the total surface area and therefore should not significantly interfere with the nanocar movement.

The diffusion constant is related to the activation energy for nanocar movement on the different substrates.<sup>57</sup> Two factors contribute to the activation energy for wheel-

like rolling: 1) the rotational energy barrier for the bond connecting the wheel to the chassis has to be overcome and 2) at least one hydrogen bond per wheel must be broken assuming that the carborane wheels interact with the surface through hydrogen bonding.<sup>57</sup> The difference in diffusion constants and hence activation energies for the nanocar diffusion on hydroxyl- vs. amine-terminated glass can indeed be explained by the strength of the different types of hydrogen bonds formed for these substrates. On amine-terminated glass, the carborane wheels form BH-HN dihydrogen bonds.<sup>145,146</sup> Formation of this type of hydrogen bond is more common between boron and nitrogen than BH-N type hydrogen bonds. The dihydrogen bonds are stronger with an energy of about 2.1 – 5.8 kcal/mol<sup>145</sup> compared to 1.1-3.7 kcal/mol<sup>147,148</sup> for BH-O hydrogen bonds on hydroxyl-terminated glass. This suggests that the lower diffusion constant and smaller number of moving nanocars on amine-terminated glass is due to the larger attractive interactions of the wheels with the substrate because of stronger hydrogen bonding.

## 5.5 Conclusions

In conclusion, we have shown that a significant improvement in the number of moving nanocars can be achieved with an intrinsically fluorescent nanocar. Furthermore, we found that both the surface roughness and the interaction strength between the nanocar wheels and the substrate are important factors in determining the percentage of moving nanocars and their speeds. When changing the surface from hydroxyl to amine termination the speed decreased two times from 4.2 nm/s to 2.1 nm/s.



## **5.6 Acknowledgements**

I thank Jazmin Godoy and Dr. James M. Tour with whom I collaborated on this project. I thank Dr. Landes and her group members for help with the Vectabond<sup>TM</sup> treated coverslips, and Dr. Kolomeisky for useful discussions. This work was supported by the Robert A. Welch Foundation (C-1664 to SL), 3M (NTFG to SL), and NSF (CHE-1007483). I would also like to acknowledge Rice University for a Stauffer-Rothrock Fellowship.

## CHAPTER 6

### CONCLUSIONS

Nematic liquid crystal promises a long range three, dimensional and switchable ordering of nanomaterial through the liquid crystal mediated rearrangement of liquid crystal in response to external fields. However, the major challenge of using liquid crystal as template for plasmonic nanoparticles involves their low solubility in nematic liquid crystal. We have shown that replacement of decanethiol with SOPB functional ligands renders 6 nm gold nanoparticles soluble in the nematic phase of 5CB. We demonstrated spectroscopically that the nanoparticles are indeed dissolved rather than dispersed and explain the enhanced solubility by the chemical similarity between the surface capping material and the liquid crystal solvent. The stability of this composite was further verified by cycling between the isotropic and nematic phases of the liquid crystals. In addition, we found a small increase of the nematic-to-isotropic phase transition temperature of  $0.4^{\circ}\text{C}$  and a desirable decrease of the threshold voltage by about 25% for an electric field induced homeotropic director alignment when a maximum nanoparticle concentration of 0.2 wt% was added to 5CB.

We have also developed a novel approach to modulate the response of individual gold nanorods by electrically switching between homogeneous and twisted nematic phases of a thermotropic liquid crystal. Even our non-optimized prototype devices show a surprisingly robust long-term stability enduring several thousand reversible switching cycles at 1 Hz for an hour without a change in scattering intensity, initial nanorod orientation, and nanorod position. We anticipate that the performance of our devices can

be further improved in terms of operating voltage and response time by carefully selecting other liquid crystal solvents. While plasmonic nanorods represent the simplest form of an optical antenna, the described strategy should directly translate to more complex antenna architectures and other plasmonic elements for the electrical manipulation of visible light in structures with nanoscale dimensions.

Using single molecule fluorescence imaging, we have observed micrometer-scale movement of dye-labeled carborane nanocars on a glass surface at room temperature. Polarization-sensitive measurements showed that translation is coupled with rotational motion. By comparing the four-wheeled nanocars to a three-wheeled nanocar analog and the unbound dye molecules, we conclude that the translation of the nanocars is consistent with a wheel-like rolling mechanism. Furthermore, we found that both the surface roughness and the interaction strength between the nanocar wheels and the substrate are important factors in determining the percentage of moving nanocars and their speeds. When changing the surface from hydroxyl to amine termination the speed decreased two times from 4.2 nm/s to 2.1 nm/s.

**APPENDIX A**  
**MOST COMMONLY USED PROGRAMS THAT WERE WRITTEN AND USED**  
**IN THE COURSE OF THIS WORK**

**1. SMCP.m:** This program reads binary files (.SM3) generated by RHK and calculates intensities and polarization anisotropies of single molecules. A stage drift correction program is also built into this program. This allows the detection of polarization anisotropy and intensity time traces of individual stationary molecules over time. This program has been used for the initial optimization of the confocal instrument and the nanocar project.

**I. Main sub-routines under SMCP.m:**

ReadImage.m	Reads the binary image files generated by RHK. It only works for older versions of SM3 files.
ReadImagel.m	Reads the binary image files generated by RHK. It works for newer versions of SM3 files (updated in 2007).
One.m	Calculates the intensity and local background values for each molecule. Actual intensities of individual molecules are calculated by subtracting the local background values. Polarization anisotropies of individual molecules are also calculated. This program works for only one image.
Findpoints.m	Finds individual molecules in the 1 <sup>st</sup> image from a time-lapse image series.

Findshift.m	This function corrects the possible sample drift among time-lapse images.
Pointengine.m	This function calculates the intensity and polarization anisotropies of individual molecules in all images and their background values.
Plotkinetics.m	Plots time traces of intensities and polarization anisotropies of individual molecules. It also plots the average intensities and polarization anisotropies of all the molecules present in one image as a function of time.
Pointrevedit.m	Filters out some of the molecules based on a trajectory filter.

## II. Some important buttons in the GUI interface:

- (a) **Dir:** It allows setting the path to the directory which contains the images to be analyzed.
- (b) **Create Exp:** It loads the .SM3 file (or the series of files) and saves the output values from Readimager.m as 'e' and 'i' structured arrays.
- (c) **Movie:** It makes a movie of all the images in a time-lapse image series loaded using **Create Exp**.
- (d) **First:** It plots only the first image from a time-lapse image series. Similarly, **Last** button plots the last images of the sequence.
- (e) **Find:** It finds individual molecules in a sequence of images and plots the mean intensity, sum of the intensities from the donor and acceptor channels, intensity of

individual channels, polarization anisotropy, and mean polarization anisotropies as a function of time.

- (f) **One:** It finds molecules in a single image and makes histograms of intensities from donor and acceptor (corrected for their local background) channels and their local backgrounds.
- (g) **Kinetics:** It revises the molecules found by the **Find** button based on certain filters (trajectory filters) and plots average intensity, sum of the intensities in donor and acceptor channels, intensity of donor channel, polarization anisotropies, and mean polarization anisotropies as function of time.
- (h) **Onek:** It makes histograms for donor and acceptor intensities (corrected to their background) and the local background.
- (i) **ROI:** It allows selecting the region of interest. You can do all the analysis taking only very few molecules.
- (j) **Oneimage:** It shows the current image only.
- (k) **Params:** It allows selecting some important parameters like molecule size and background size.
- (l) **Gausefit:** A Gaussian fit program to detect the full width half maxima of single molecules.

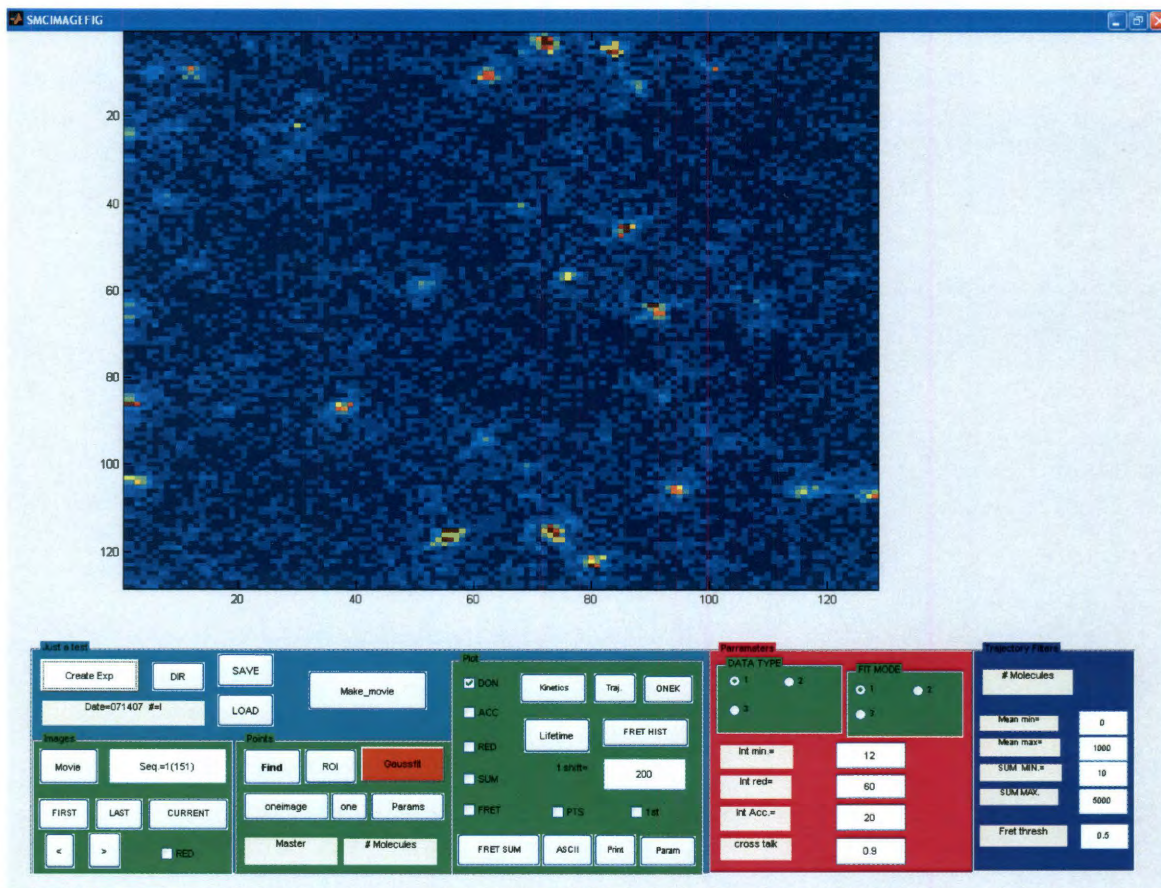


Figure A1: Screenshot of the SMCP program showing the front panel.

### III. How to operate the SMC program:

#### 1. For one image only:

- (a). Click DIR button and set the path of the folder containing the images you want to analyze.
- (b). Click Creat Exp button and enter the file name you want to analyze (do not forget to put the folder name in the first line).
- (c). Select the donor, acceptor, or SUM panel depending on whether you want to analyze one channel or the total intensity of the two channels.
- (d) Click the FIRST button. It will show the selected channels in (c).

- (e) Click the ONE button. It finds the molecules, calculates intensities of each molecule over a predefined number of pixels, calculates the background intensities, and makes histograms of polarization, acceptor and donor intensities, and their background values.
- (f). Click Oneimage to see which molecules are found.

## **2. For a time-series of images:**

- (a) Follow steps 1(a) to 1(d) as mentioned earlier.
- (b) Click Find button. It finds the molecules, calculates the intensity of each molecule over some pixels, calculates the background intensities, and makes plots for the sum of donor and acceptor intensities vs. time, mean intensity vs. time, donor intensity vs. time, polarization vs. time, and mean polarization vs. time.
- (c) To see which molecules are found, click the First button.
- (d) If you want to get the histograms for acceptor and donor intensity as well as their background values for one particular image, just select that image (with the > or < button) and hit ONEK button.
- (e) You can further filter the number of molecules found by hitting Kinetics button. It takes all the values calculated by the Find routine, and deletes some of them by applying filters as mentioned above.
- (f) Click First button to see which of the molecules initially found by the Find routine are deleted by Kinetics (the red diamond shaped ones are deleted).



**2. SMS\_VIS.m:** This is a single molecule tracking algorithm developed to track surface diffusion of nanocars. This program accounts for blinking and bleaching of single molecules.

**3. Spectra and image analysis program:** This program is used to read and further process the data generated by a CCD camera.

## APPENDIX B

### CALIBRATION OF BULK FLUORESCENCE SPECTRA ACQUIRED BY A COMMERCIAL FLUOREMETER

In this work, the spectral response of a commercial fluorimeter (Perkin Elmer, LS50B) was calibrated over the range of 300- 800 nm using standard dyes. The detailed procedure can be found elsewhere.<sup>149</sup> In brief, corrected spectra of fluorescent dyes are compared with their spectra obtained from the fluorimeter and correction factors were calculated based on the deviation from the correct spectra. The standard dyes used in this study are (1) Tryptophan, (2) Coumarin 153, (3) Tetraphenylbutadiene (TBP), and (4) 4-dicyanomethylene)-2-methyl-6-(4-dimethylaminostyryl)-4H-pyran (DCM). These dyes were bought from Sigma-Aldrich and used as received. Water, cyclohexane, and methanol were used as solvents for Tryptophan, TBP, and DCM (as well as Coumarin 153) respectively. Fluorescence spectra of these dyes were acquired by exciting at their respective absorption maxima  $\lambda_{\max}$ .

Probe	Solvent	Excitation Wavelength (nm)	Emission Range (nm)
Tryptophan	Water	265	310-428
TBP	Cyclohexane	340	390-570
Coumarin 153	Methanol	400	486-678
DCM	Methanol	460	556-736

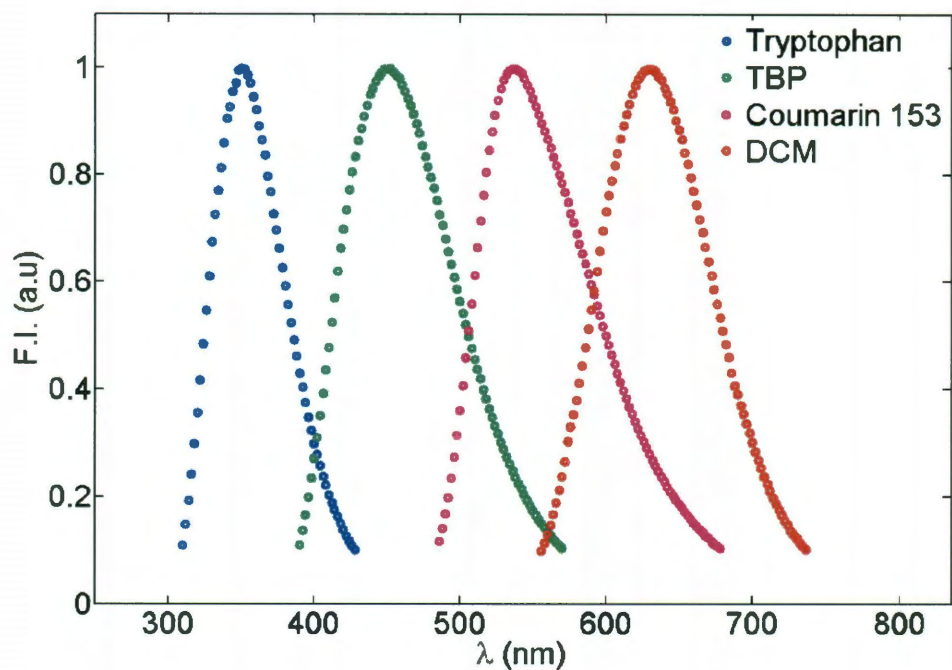


**Figure B.1:** Actual fluorescence spectra of standard fluorophores directly adopted from reference.<sup>149</sup> Excitation wavelengths ( $\lambda_{ex}$ ) were 265 nm (tryptophan), 340 nm (TBP), 400 nm (Coumarin 153), and 460 nm (DCM).

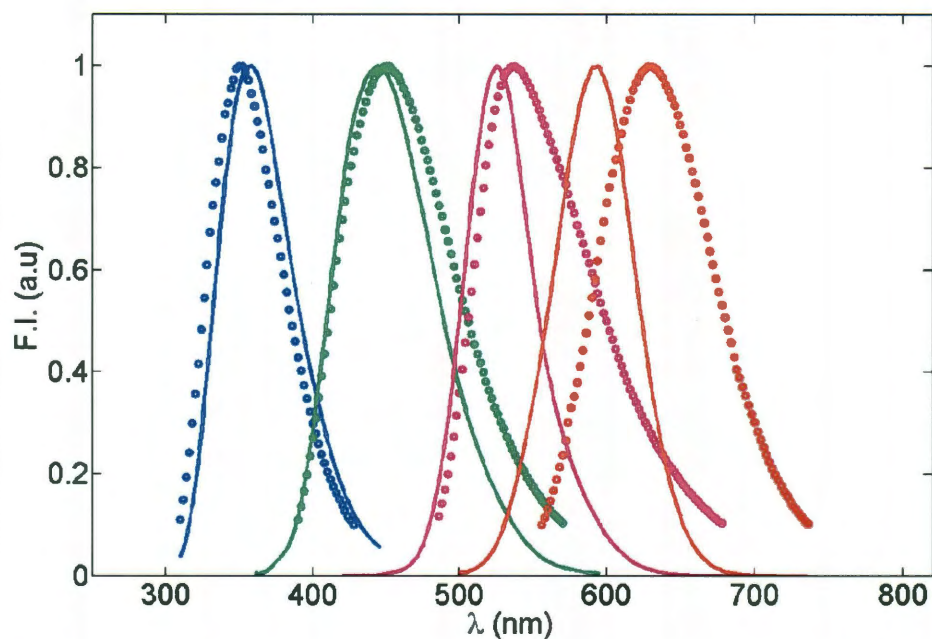


**Figure B.2:** Actual (circles) and measured (line) fluorescence spectra of tryptophan (blue,  $\lambda_{ex} = 265$  nm), TBP (green,  $\lambda_{ex} = 340$  nm), Coumarin 153 (magenta,  $\lambda_{ex} = 400$  nm), and DCM (red,  $\lambda_{ex} = 460$  nm). The measured spectra of these standard fluorophores are clearly different from their actual spectra emphasizing the need for detector calibration.

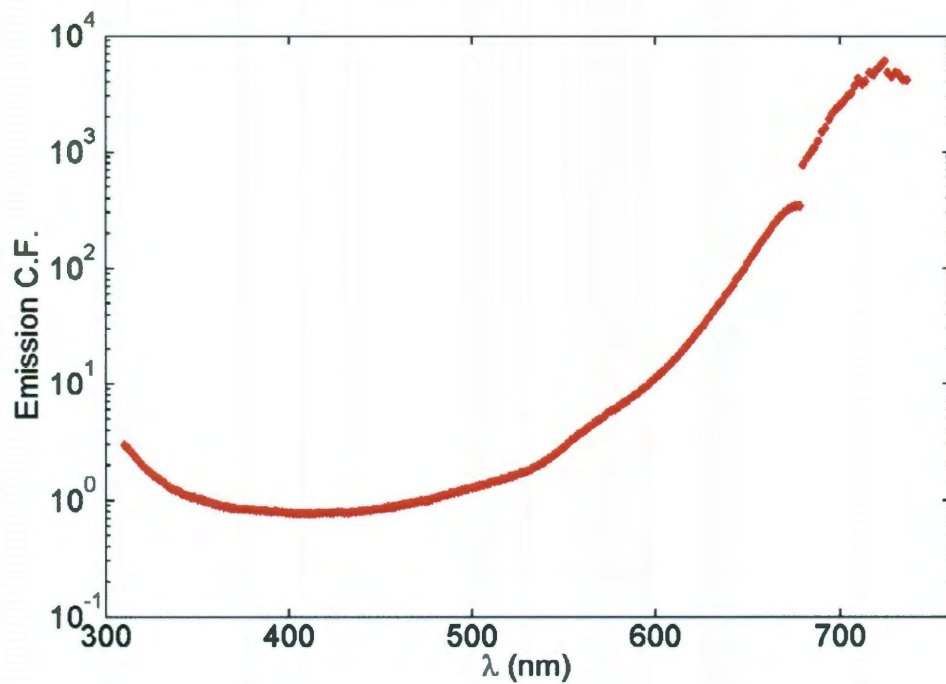


**Figure B.3:** Spectra-generated emission correction factors using the procedure described in ref.<sup>149</sup>

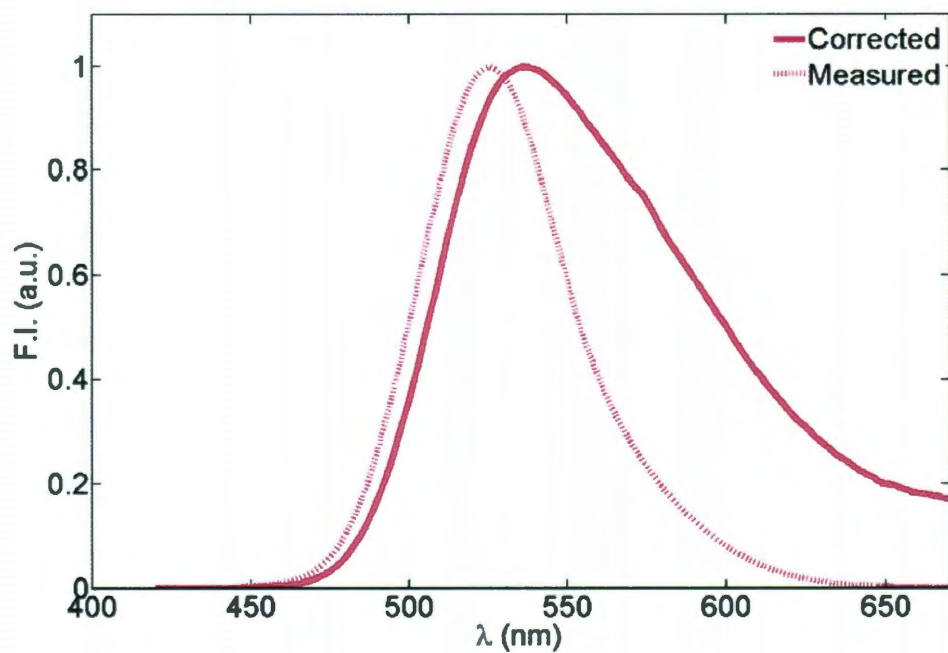


**Figure B.4:** Measured spectra of Coumarin 153 (dotted line) and after applying the correction factors (solid line).

## BIBLIOGRAPHY

- (1) Kreibig, U.; Vollmer, M. *Springer: Berlin* **1995**.
- (2) Jin, R.; Cao, Y.; Mirkin, C. A.; Kelly, K. L.; Schatz, G. C.; Zheng, J. G. *Science* **2001**, *294*, 1901-1903.
- (3) Lal, S.; Link, S.; Halas, N. J. *Nat. Photonics* **2007**, *1*, 641-648.
- (4) Sun, Y.; Xia, Y. *Science* **2002**, *298*, 2176-2179.
- (5) Fan, J. A.; Wu, C. H.; Bao, K.; Bao, J. M.; Bardhan, R.; Halas, N. J.; Manoharan, V. N.; Nordlander, P.; Shvets, G.; Capasso, F. *Science* **2010**, *328*, 1135-1138.
- (6) Hentschel, M.; Saliba, M.; Vogelgesang, R.; Giessen, H.; Alivisatos, A. P.; Liu, N. *Nano Lett.* **2010**, *10*, 2721-2726.
- (7) Maier, S. A.; Kik, P. G.; Atwater, H. A.; Meltzer, S.; Harel, E.; Koel, B. E.; Requicha, A. A. G. *Nat. Mater.* **2003**, *2*, 229-232.
- (8) Kinkhabwala, A.; Yu, Z. F.; Fan, S. H.; Avlasevich, Y.; Mullen, K.; Moerner, W. E. *Nat. Photonics* **2009**, *3*, 654-657.
- (9) Kundu, J.; Le, F.; Nordlander, P.; Halas, N. J. *Chem. Phys. Lett.* **2008**, *452*, 115-119.
- (10) Anker, J. N.; Hall, W. P.; Lyandres, O.; Shah, N. C.; Zhao, J.; Van Duyne, R. P. *Nat. Mater.* **2008**, *7*, 442-453.
- (11) Engheta, N. *Science* **2007**, *317*, 1698-1702.
- (12) Ozbay, E. *Science* **2006**, *311*, 189-193.
- (13) Lezec, H. J.; Dionne, J. A.; Atwater, H. A. *Science* **2007**, *316*, 430-432.
- (14) Valentine, J.; Zhang, S.; Zentgraf, T.; Ulin-Avila, E.; Genov, D. A.; Bartal, G.; Zhang, X. *Nature* **2008**, *455*, 376-U32.

- (15) Henzie, J.; Lee, J.; Lee, M. H.; Hasan, W.; Odom, T. W. *Annu. Rev. Phys. Chem.* **2009**, *60*, 147-165.
- (16) Gunnarsson, L.; Rindzevicius, T.; Prikulis, J.; Kasemo, B.; Kall, M.; Zou, S. L.; Schatz, G. C. *J. Phys. Chem. B* **2005**, *109*, 1079-1087.
- (17) Henzie, J.; Lee, M. H.; Odom, T. W. *Nat. Nanotechnol.* **2007**, *2*, 549-554.
- (18) Jones, M. R.; Osberg, K. D.; Macfarlane, R. J.; Langille, M. R.; Mirkin, C. A. *Chem. Rev.*, *111*, 3736-3827.
- (19) Khanal, B. P.; Zubarev, E. R. *Angew. Chem.-Int. Edit.* **2007**, *46*, 2195-2198.
- (20) Chang, W. S.; Slaughter, L. S.; Khanal, B. P.; Manna, P.; Zubarev, E. R.; Link, S. *Nano Lett.* **2009**, *9*, 1152-1157.
- (21) Ming, T.; Kou, X. S.; Chen, H. J.; Wang, T.; Tam, H. L.; Cheah, K. W.; Chen, J. Y.; Wang, J. F. *Angew. Chem.-Int. Edit.* **2008**, *47*, 9685-9690.
- (22) Mirkin, C. A.; Letsinger, R. L.; Mucic, R. C.; Storhoff, J. J. *Nature* **1996**, *382*, 607-609.
- (23) Boal, A. K.; Ilhan, F.; DeRouchey, J. E.; Thurn-Albrecht, T.; Russell, T. P.; Rotello, V. M. *Nature* **2000**, *404*, 746-748.
- (24) Blum, A. S.; Soto, C. M.; Wilson, C. D.; Cole, J. D.; Kim, M.; Gnade, B.; Chatterji, A.; Ochoa, W. F.; Lin, T. W.; Johnson, J. E.; Ratna, B. R. *Nano Lett.* **2004**, *4*, 867-870.
- (25) Dierking, I.; Scalia, G.; Morales, P.; LeClere, D. *Adv. Mater.* **2004**, *16*, 865-869.
- (26) Chang, W. S.; Link, S.; Yethiraj, A.; Barbara, P. F. *J. Phys. Chem. B* **2008**, *112*, 448-453.

- (27) Wu, K.-J.; Chu, K.-C.; Chao, C.-Y.; Chen, Y.-F.; Lai, C.-W.; Kang, C.-C.; Chen, C.-Y.; Chou, P.-T. *Nano Lett.* **2007**, *7*, 1908-1913.
- (28) Koenig, G. M.; Meli, M.-V.; Park, J.-S.; de Pablo, J. J.; Abbott, N. L. *Chem. Mater.* **2007**, *19*, 1053-1061.
- (29) Dickson, W.; Wurtz, G. A.; Evans, P. R.; Pollard, R. J.; Zayats, A. V. *Nano Lett.* **2008**, *8*, 281-286.
- (30) Berthelot, J.; Bouhelier, A.; Huang, C.; Margueritat, J. r. m.; Colas-des-Francis, G. r.; Finot, E.; Weeber, J.-C.; Dereux, A.; Kostcheev, S.; Ahrach, H. I. E.; Baudrion, A.-L.; Plain, J. r. m.; Bachelot, R.; Royer, P.; Wiederrecht, G. P. *Nano Lett.* **2009**, *9*, 3914-3921.
- (31) Chu, K. C.; Chao, C. Y.; Chen, Y. F.; Wu, Y. C.; Chen, C. C. *Appl. Phys. Lett.* **2006**, *89*, 103107/1-103107/3.
- (32) Kossyrev, P. A.; Yin, A.; Cloutier, S. G.; Cardimona, D. A.; Huang, D.; Alsing, P. M.; Xu, J. M. *Nano Lett.* **2005**, *5*, 1978-1981.
- (33) Müller, J.; Sönnichsen, C.; von Poschinger, H.; von Plessen, G.; Klar, T. A.; Feldmann, J. *Appl. Phys. Lett.* **2002**, *81*, 171-173.
- (34) Kay, E. R.; Leigh, D. A.; Zerbetto, F. *Angew. Chem.-Int. Edit.* **2007**, *46*, 72-191.
- (35) Endow, S. A. *BioEssays* **2003**, *25*, 1212-1219.
- (36) Schliwa, M.; Woehlke, G. *Nature* **2003**, *422*, 759-765.
- (37) Badjic, J. D.; Balzani, V.; Credi, A.; Silvi, S.; Stoddart, J. F. *Science* **2004**, *303*, 1845-1849.
- (38) Badjic, J. D.; Ronconi, C. M.; Stoddart, J. F.; Balzani, V.; Silvi, S.; Credi, A. *J. Am. Chem. Soc.* **2006**, *128*, 1489-1499.

- (39) Brouwer, A. M.; Frochot, C.; Gatti, F. G.; Leigh, D. A.; Mottier, L.; Paolucci, F.; Roffia, S.; Wurpel, G. W. H. *Science* **2001**, *291*, 2124-2128.
- (40) Perez, E. M.; Dryden, D. T. F.; Leigh, D. A.; Teobaldi, G.; Zerbetto, F. *J. Am. Chem. Soc.* **2004**, *126*, 12210-12211.
- (41) Baber, A. E.; Tierney, H. L.; Sykes, E. C. H. *ACS Nano* **2008**, *2*, 2385-2391.
- (42) van Delden, R. A.; ter Wiel, M. K. J.; Pollard, M. M.; Vicario, J.; Koumura, N.; Feringa, B. L. *Nature* **2005**, *437*, 1337-1340.
- (43) London, G.; Carroll, G. T.; Fernandez Landaluce, T.; Pollard, M. M.; Rudolf, P.; Feringa, B. L. *Chem Commun (Camb)* **2009**, 1712-4.
- (44) Bedard, T. C.; Moore, J. S. *J. Am. Chem. Soc.* **1995**, *117*, 10662-10671.
- (45) Muraoka, T.; Kinbara, K.; Aida, T. *Nature* **2006**, *440*, 512-515.
- (46) Shirai, Y.; Osgood, A. J.; Zhao, Y.; Yao, Y.; Saudan, L.; Yang, H.; Chiu, Y.-H.; Alemany, L. B.; Sasaki, T.; Morin, J.-F.; Guerrero, J. M.; Kelly, K. F.; Tour, J. M. *J. Am. Chem. Soc.* **2006**, *128*, 4854-4864.
- (47) Shirai, Y.; Morin, J.-F.; Sasaki, T.; Guerrero, J. M.; Tour, J. M. *Chem. Soc. Rev.* **2006**, *35*, 1043-1055.
- (48) Shirai, Y.; Osgood, A. J.; Zhao, Y.; Kelly, K. F.; Tour, J. M. *Nano Lett.* **2005**, *5*, 2330-2334.
- (49) Vives, G.; Guerrero, J. M.; Godoy, J.; Khatua, S.; Wang, Y. P.; Kiappes, J. L.; Link, S.; Tour, J. M. *J. Org. Chem.* **2010**, *75*, 6631-6643.
- (50) Shirai, Y.; Osgood, A. J.; Zhao, Y. M.; Kelly, K. F.; Tour, J. M. *Nano Lett.* **2005**, *5*, 2330-2334.



- (51) Sonnichsen, C.; Reinhard, B. M.; Liphardt, J.; Alivisatos, A. P. *Nat. Biotechnol.* **2005**, *23*, 741-745.
- (52) Celebrano, M.; Kukura, P.; Renn, A.; Sandoghdar, V. *Nat. Photonics* **2010**, *5*, 95-98.
- (53) Gaiduk, A.; Yorulmaz, M.; Ruijgrok, P. V.; Orrit, M. *Science* **2010**, *330*, 353-356.
- (54) Yildiz, A.; Tomishige, M.; Vale, R. D.; Selvin, P. R. *Science* **2004**, *303*, 676-679.
- (55) Kulzer, F.; Xia, T.; Orrit, M. *Angew. Chem.-Int. Edit.* **2010**, *49*, 854-866.
- (56) Roy, R.; Hohng, S.; Ha, T. *Nat. Methods* **2008**, *5*, 507-516.
- (57) Khatua, S.; Guerrero, J. M.; Claytor, K.; Vives, G.; Kolomeisky, A. B.; Tour, J. M.; Link, S. *ACS Nano* **2009**, *3*, 351-356.
- (58) Zondervan, R.; Kulzer, F.; Kol'chenko, M. A.; Orrit, M. *J. Phys. Chem. A* **2004**, *108*, 1657-1665.
- (59) Thompson, R. E.; Larson, D. R.; Webb, W. W. *Biophys. J.* **2002**, *82*, 2775-2783.
- (60) Khatua, S.; Manna, P.; Chang, W.-S.; Tcherniak, A.; Friedlander, E.; Zubarev, E. R.; Link, S. *J. Phys. Chem. C* **2009**, *114*, 7251-7257.
- (61) Khatua, S.; Chang, W.-S.; Swanglap, P.; Olson, J.; Link, S. *Nano Lett.* **2011**, *11*, 3797-3802.
- (62) Khatua, S.; Godoy, J.; Tour, J. M.; Link, S. *The Journal of Physical Chemistry Letters* **2010**, *1*, 3288-3291.
- (63) Ghosh, S. K.; Nath, S.; Kundu, S.; Esumi, K.; Pal, T. *Journal of Physical Chemistry B* **2004**, *108*, 13963-13971.
- (64) Templeton, A. C.; Pietron, J. J.; Murray, R. W.; Mulvaney, P. *J. Phys. Chem. B* **2000**, *104*, 564-570.

- (65) Underwood, S.; Mulvaney, P. *Langmuir* **1994**, *10*, 3427-3430.
- (66) Wang, Y. *Appl. Phys. Lett.* **1995**, *67*, 2759-61.
- (67) Wang, Y.; Russell, S. D.; Shimabukuro, R. L. *J. Appl. Phys.* **2005**, *97*, 023708/1-023708/5.
- (68) Evans, P. R.; Wurtz, G. A.; Hendren, W. R.; Atkinson, R.; Dickson, W.; Zayats, A. V.; Pollard, R. J. *Appl. Phys. Lett.* **2007**, *91*, 043101/1-043101/3.
- (69) Evans, S. D.; Allinson, H.; Boden, N.; Flynn, T. M.; Henderson, J. R. *J. Phys. Chem. B* **1997**, *101*, 2143-2148.
- (70) Koenig, G. M.; Gettelfinger, B. T.; de Pablo, J. J.; Abbott, N. L. *Nano Lett.* **2008**, *8*, 2362-2368.
- (71) Haraguchi, F.; Inoue, K.; Toshima, N.; Kobayashi, S.; Takatoh, K. *Japanese Journal of Applied Physics Part 2* **2007**, *46*, L796-L797.
- (72) Reznikov, Y.; Buchnev, O.; Tereshchenko, O.; Reshetnyak, V.; Glushchenko, A.; West, J. *Appl. Phys. Lett.* **2003**, *82*, 1917-1919.
- (73) Duran, H.; Gazdecki, B.; Yamashita, A.; Kyu, T. *Liq. Cryst.* **2005**, *32*, 815-821.
- (74) Lynch, M. D.; Patrick, D. L. *Nano Lett.* **2002**, *2*, 1197-1201.
- (75) Link, S.; Hu, D.; Chang, W. S.; Scholes, G. D.; Barbara, P. F. *Nano Lett.* **2005**, *5*, 1757-1760.
- (76) Barbara, P. F.; Chang, W. S.; Link, S.; Scholes, G. D.; Yethiraj, A. *Annu. Rev. Phys. Chem.* **2007**, *58*, 565-584.
- (77) Tcherniak, A.; Solis, D.; Khatua, S.; Tangonan, A. A.; Lee, T. R.; Link, S. *J. Am. Chem. Soc.* **2008**, *130*, 12262-12263.

- (78) Holt, L. A.; Bushby, R. J.; Evans, S. D.; Burgess, A.; Seeley, G. *J. Appl. Phys.* **2008**, *103*, 063712/1-063712/7.
- (79) Kumar, S.; Lakshminarayanan, V. *Chem. Commun. (Cambridge, U. K.)* **2004**, 1600-1601.
- (80) Qi, H.; Kinkead, B.; Marx, V.; Zhang, H.; Hegmann, T. *ChemPhysChem* **2009**, *10*, 1211-1218.
- (81) Kumar, S.; Pal, S. K.; Kumar, P. S.; Lakshminarayanan, V. *Soft Matter* **2007**, *3*, 896-900.
- (82) Marx, V. M.; Girgis, H.; Heiney, P. A.; Hegmann, T. *J. Mater. Chem.* **2008**, *18*, 2983-2994.
- (83) Frein, S.; Boudon, J.; Vonlanthen, M.; Scharf, T.; Barbera, J.; Suss-Fink, G.; Burgi, T.; Deschenaux, R. *Helv. Chim. Acta* **2008**, *91*, 2321-2337.
- (84) In, I.; Jun, Y.-W.; Kim, Y. J.; Kim, S. Y. *Chem. Commun. (Cambridge, U. K.)* **2005**, 800-801.
- (85) Zeng, X.; Liu, F.; Fowler, A. G.; Ungar, G.; Cseh, L.; Mehl, G. H.; Macdonald, E. J. *Adv. Mater. (Weinheim, Ger.)* **2009**, *21*, 1746-1750.
- (86) Fritz, K. P.; Scholes, G. D. *The Journal of Physical Chemistry B* **2003**, *107*, 10141-10147.
- (87) Brust, M.; Fink, J.; Bethell, D.; Schiffrin, D. J.; Kiely, C. *J. Chem. Soc., Chem. Commun.* **1995**, 1655-1656.
- (88) Lin, X. M.; Wang, G. M.; Sorensen, C. M.; Klabunde, K. J. *J. Phys. Chem. B* **1999**, *103*, 5488-5492.

- (89) Zubarev, E. R.; Xu, J.; Sayyad, A.; Gibson, J. D. *J. Am. Chem. Soc.* **2006**, *128*, 4958-4959.
- (90) Gibson, J. D.; Khanal, B. P.; Zubarev, E. R. *J. Am. Chem. Soc.* **2007**, *129*, 11653-11661.
- (91) Link, S.; Wang, Z. L.; El-Sayed, M. A. *The Journal of Physical Chemistry B* **1999**, *103*, 3529-3533.
- (92) Storhoff, J. J.; Mirkin, C. A. *Chem. Rev.* **1999**, *99*, 1849-1862.
- (93) Moskovits, M.; Vlckova, B. *J. Phys. Chem. B* **2005**, *109*, 14755-14758.
- (94) Kreibig, U.; Genzel, L. *Surf. Sci.* **1985**, *156*, 678-700.
- (95) Link, S.; El-Sayed, M. A. *The Journal of Physical Chemistry B* **1999**, *103*, 4212-4217.
- (96) Alvarez, M. M.; Khoury, J. T.; Schaaff, T. G.; Shafigullin, M. N.; Vezmar, I.; Whetten, R. L. *J. Phys. Chem. B* **1997**, *101*, 3706-3712.
- (97) Li, J.; Gauza, S.; Wu, S.-T. *J. Appl. Phys.* **2004**, *96*, 19-24.
- (98) Johnson, P. B.; Christy, R. W. *Physical Review B* **1972**, *6*, 4370-4379.
- (99) Berciaud, S.; Cognet, L.; Tamarat, P.; Lounis, B. *Nano Lett.* **2005**, *5*, 515-518.
- (100) Novo, C.; Gomez, D.; Perez-Juste, J.; Zhang, Z.; Petrova, H.; Reismann, M.; Mulvaney, P.; Hartland, G. V. *Phys. Chem. Chem. Phys.* **2006**, *8*, 3540-3546.
- (101) Boichuk, V.; Kucheev, S.; Parka, J.; Reshetnyak, V.; Reznikov, Y.; Shiyanovskaya, I.; Singer, K. D.; Slussarenko, S. *J. Appl. Phys.* **2001**, *90*, 5963-5967.
- (102) Nie, S.; Emory, S. R. *Science* **1997**, *275*, 1102-1106.
- (103) Atwater, H. A.; Polman, A. *Nat. Mater.* **2010**, *9*, 205-213.

- (104) Kulkarni, A. P.; Noone, K. M.; Munechika, K.; Guyer, S. R.; Ginger, D. S. *Nano Lett.* **2010**, *10*, 1501-1505.
- (105) Stockhausen, V.; Martin, P.; Ghilane, J.; Leroux, Y.; Randriamahazaka, H.; Grand, J.; Felidj, N.; Lacroix, J. C. *J. Am. Chem. Soc.* **2010**, *132*, 10224-10226.
- (106) Leroux, Y.; Lacroix, J. C.; Fave, C.; Stockhausen, V.; Felidj, N.; Grand, J.; Hohenau, A.; Krenn, J. R. *Nano Lett.* **2009**, *9*, 2144-2148.
- (107) Zheng, Y. B.; Yang, Y. W.; Jensen, L.; Fang, L.; Juluri, B. K.; Flood, A. H.; Weiss, P. S.; Stoddart, J. F.; Huang, T. J. *Nano Lett.* **2009**, *9*, 819-825.
- (108) Zheng, Y. B.; Kiraly, B.; Cheunkar, S.; Huang, T. J.; Weiss, P. S. *Nano Lett.* **2011**, *11*, 2061-2065.
- (109) Muller, J.; Sonnichsen, C.; von Poschinger, H.; von Plessen, G.; Klar, T. A.; Feldmann, J. *Appl. Phys. Lett.* **2002**, *81*, 171-173.
- (110) Tam, F.; Moran, C.; Halas, N. *J. Phys. Chem. B* **2004**, *108*, 17290-17294.
- (111) Lee, K.-S.; El-Sayed, M. A. *J. Phys. Chem. B* **2006**, *110*, 19220-19225.
- (112) Park, S. J.; Link, S.; Miller, W. L.; Gesquiere, A.; Barbara, P. F. *Chem. Phys.* **2007**, *341*, 169-174.
- (113) Yamauchi, M.; Marquez, A.; Davis, J. A.; Franich, D. J. *Opt. Commun.* **2000**, *181*, 1-6.
- (114) Stohr, J.; Samant, M. G.; Cossy-Favre, A.; Diaz, J.; Momoi, Y.; Odahara, S.; Nagata, T. *Macromolecules* **1998**, *31*, 1942-1946.
- (115) Sonnichsen, C.; Franzl, T.; Wilk, T.; von Plessen, G.; Feldmann, J.; Wilson, O.; Mulvaney, P. *Phys. Rev. Lett.* **2002**, *88*, 077402.

- (116) Andrienko, D.; Barbet, F.; Bormann, D.; Kurioz, Y.; Kwon, S. B.; Reznikov, Y.; Warenghem, M. *Liq. Cryst.* **2000**, *27*, 365-370.
- (117) Eelkema, R.; Pollard, M. M.; Vicario, J.; Katsonis, N.; Ramon, B. S.; Bastiaansen, C. W. M.; Broer, D. J.; Feringa, B. L. *Nature* **2006**, *440*, 163-163.
- (118) Liu, Q. K.; Cui, Y. X.; Gardner, D.; Li, X.; He, S. L.; Smalyukh, I. *Nano Lett.* **2010**, *10*, 1347-1353.
- (119) Berreman, D. W. *Appl. Phys. Lett.* **1974**, *25*, 12-15.
- (120) Fletcher, S. P.; Dumur, F.; Pollard, M. M.; Feringa, B. L. *Science* **2005**, *310*, 80-82.
- (121) Leigh, D. A.; Wong, J. K. Y.; Dehez, F.; Zerbetto, F. *Nature* **2003**, *424*, 174-179.
- (122) Kelly, T. R.; De Silva, H.; Silva, R. A. *Nature* **1999**, *401*, 150-152.
- (123) Bissell, R. A.; Cordova, E.; Kaifer, A. E.; Stoddart, J. F. *Nature* **1994**, *369*, 133-137.
- (124) Brouwer, A. M.; Frochot, C.; Gatti, F. G.; Leigh, D. A.; Mottier, L.; Paolucci, F.; Roffia, S.; Wurpel, G. W. H. *Science (Washington, DC, U. S.) FIELD Full Journal Title: Science (Washington, DC, United States)* **2001**, *291*, 2124-2128.
- (125) Serreli, V.; Lee, C.-F.; Kay, E. R.; Leigh, D. A. *Nature (London, U. K.)* **2007**, *445*, 523-527.
- (126) Liu, Y.; Flood, A. H.; Bonvallett, P. A.; Vignon, S. A.; Northrop, B. H.; Tseng, H. R.; Jeppesen, J. O.; Huang, T. J.; Brough, B.; Baller, M.; Magonov, S.; Solares, S. D.; Goddard, W. A.; Ho, C. M.; Stoddart, J. F. *J. Am. Chem. Soc.* **2005**, *127*, 9745-9759.
- (127) Morin, J.-F.; Sasaki, T.; Shirai, Y.; Guerrero, J. M.; Tour, J. M. *J. Org. Chem.* **2007**, *72*, 9481-9490.

- (128) Gimzewski, J. K.; Joachim, C. *Science* **1999**, *283*, 1683-1688.
- (129) Thompson, R. E.; Daniel R. Larson; Webb, W. W. *Biophys. J.* **2002**, *82*, 2775–2783.
- (130) Qu, X.; Wu, D.; Mets, L.; Scherer, N. F. *Proc. Natl. Acad. Sci. U. S. A.* **2004**, *101*, 11298-11303.
- (131) Forkey, J. N.; Quinlan, M. E.; Goldman, Y. E. *Prog. Biophys. Mol. Biol.* **2000**, *74*, 1-35.
- (132) Ha, T.; Laurence, T. A.; Chemla, D. S.; Weiss, S. *J. Phys. Chem. B* **1999**, *103*, 6839-6850.
- (133) Schmidt, T.; Schutz, G. J.; Baumgartner, W.; Gruber, H. J.; Schindler, H. *Proc. Natl. Acad. Sci. U. S. A.* **1996**, *93*, 2926-2929.
- (134) Altman, E. I.; Colton, R. J. *Surf. Sci.* **1992**, *279*, 49-67.
- (135) Akimov, A. V.; Nemukhin, A. V.; Moskovsky, A. A.; Kolomeisky, A. B.; Tour, J. *M. J. Chem. Theory Comput.* **2008**, *4*, 652-656.
- (136) Schunack, M.; Linderoth, T. R.; Rosei, F.; Laegsgaard, E.; Stensgaard, I.; Besenbacher, F. *Phys. Rev. Lett.* **2002**, *88*, 156102/1-156102/4.
- (137) Rosei, F.; Schunack, M.; Naitoh, Y.; Jiang, P.; Gourdon, A.; Laegsgaard, E.; Stensgaard, I.; Joachim, C.; Besenbacher, F. *Prog. Surf. Sci.* **2003**, *71*, 95-146.
- (138) Atkins, P.; depaula, J. *Physical Chemistry*; 7th ed.; Freeman and Company: New York, 2002; Vol. Chapter 28.
- (139) Andrews, P. C.; Hardie, M. J.; Raston, C. L. *Coord. Chem. Rev.* **1999**, *189* 169–198.
- (140) Vives, G.; Tour, J. M. *Acc. Chem. Res.* **2009**, *42*, 473-487.

- (141) Godoy, J.; Vives, G.; Tour, J. M. *Org. Lett.* **2010**, *12*, 1464-1467.
- (142) Fox, M. A.; Cameron, A. M.; Low, P. J.; Paterson, M. A. J.; Batsanov, A. S.; Goeta, A. E.; Rankin, D. W. H.; Robertson, H. E.; Schirlin, J. T. *Dalton Trans.* **2006**, 3544-3560.
- (143) Taylor, J. N.; Darugar, Q.; Kourentzi, K.; Willson, R. C.; Landes, C. F. *Biochem. Biophys. Res. Commun.* **2008**, *373*, 213-218.
- (144) Claytor, K.; Khatua, S.; Guerrero, J. M.; Tcherniak, A.; Tour, J. M.; Link, S. J. *Chem. Phys.* **2009**, *130*, 1647101-9
- (145) Fanfrlik, J.; Lepsik, M.; Horinek, D.; Havlas, Z.; Hobza, P. *ChemPhysChem* **2006**, *7*, 1100-1105.
- (146) Patwari, G. N. *J. Phys. Chem. A* **2005**, *109*, 2035-2038.
- (147) Andrews, P. C.; Hardie, M. J.; Raston, C. L. *Coord. Chem. Rev.* **1999**, *189*, 169-198.
- (148) Godfrey, P. D.; Grigsby, W. J.; Nichols, P. J.; Raston, C. L. *J. Am. Chem. Soc.* **1997**, *119*, 9283-9284.
- (149) Gardecki, J. A.; Maroncelli, M. *Appl. Spectrosc.* **1998**, *52*, 1179-1189.